Optimising Artificial Reef Design through Large-Scale Experiments

Part of CREST: Coral Reef Restoration for Coastal Resilience

MSc Thesis

Vincent Takens

Delft University of Technology

TU Delft

Optimising Artificial Reef Design through Large-Scale Experiments

Part of CREST: Coral Reef Restoration for Coastal Resilience

by

Vincent Takens

Student Name	Student Number
V. Takens	4940288

Thesis commitee:	Dr. M.F.S. Tissier,	TU Delft, chair
	Dr. Ir. S.G. Pearson,	TU Delft
	Prof. Dr. Ir. A.J.H.M. Reniers,	TU Delft
	Ir. S. Haage,	Boskalis

Cover: Installation of the artificial reef restoration into the Deltares Wave Flume

TU Delft

Acknowledgements

This thesis marks the end of my academic journey and as a student of TU Delft. I write these acknowledgements on the day of the United States presidential elections, and while I am not from there, nor have ever been there, it makes me reflect on the current state of scientific research. The importance of scientific research is undervalued more and more by political leaders and societies worldwide, yet, especially in the face of climate change, is more important than ever. I am grateful to have been part of a community that values and promotes the importance of science. With that, I would like to take this opportunity to thank everyone who contributed to this thesis and supported me throughout my studies.

First of all, I would like to thank Marion Tissier, the chair of my committee, for all her helpful advice, guidance, and encouragement throughout this process. Her enthusiasm and positivity helped me find direction and structure in my work. I would also like to thank my other committee members: Ad Reniers for his critical insights and of course his help during the installation of all the elements; Stuart Pearson, whose enthusiasm and perspective added depth to my work; and Samantha Haage, for her helpfulness on the practical side of my work.

I am also very thankful to Coastruction, and in particular Nadia, for allowing me to collaborate with them in designing and constructing the elements with their 3D printer. This opportunity gave me valuable insights into work outside academia, which is very focused on improving the world around us. It was a truly rewarding experience and one I definitely did not expect when I began my studies.

My thanks also goes out to to the Water Lab team at TU Delft for their valuable support in planning and preparing the laboratory experiments, always thinking along and thinking in possibilities rather than problems. Their help with the logistics of installing the elements and instrumentation made the process significantly smoother. Additionally, I would like to thank the team at the Delta Flume at Deltares for their collaboration and dedication to making the experiments successful. The many days spent at the Delta Flume working on the experiments were a highlight of this project. My gratitude also goes to everyone at Plymouth University who contributed to this project, especially Floortje Roelvink, whose input was invaluable to the success of the laboratory experiments.

Finally, I would like to thank my friends in Delft and my family back in Groningen for supporting me, with whom I shared many happy moments during these months of writing my thesis and throughout my entire academic journey. I look forward to what comes next for me in the future.

Vincent Takens
Delft, December 2024

Abstract

Low-lying coral islands are vulnerable to sea-level rise and climate change. These islands are protected by coral reefs, which are currently in decline as they are threatened through a combination of climate change and anthropogenic stressors. Reef restoration practises, in the form of artificial reefs, pose a solution to this issue. However, the effectiveness of these reefs in mitigating coastal flooding, as well as the effect these complex structures have on the wave field, remains unclear.

This research examines the impact of an artificial reef located on the reef flat, designed for both ecological benefit and coastal protection, on spectral wave transformation over fringing reefs. It combines numerical modelling with SWASH and large-scale experiments conducted in the Deltares Delta Flume. The flume, measuring 300 m in length and 5 m in width, was used to reconstruct a fringing reef island with a geometric scaling factor of 3. These experiments were carried out as part of the CREST project, led by TU Delft in collaboration with Plymouth University, Deltares, Boskalis, and Coastruction. It extends the ARISE initiative led by Plymouth University, which examines natural adaptations of atoll islands to rising sea levels.

The thesis has three objectives: (1) designing an artificial reef for laboratory experiments, (2) investigating and optimising its placement and density for maximal coastal protection through numerical modelling in SWASH, and (3) comparing numerical results with the laboratory outcomes. The artificial reefs consist of elements of 0.25 m in height stretching over a 10 m length and are modelled in SWASH as a porous medium. Default, uncalibrated dimensional parameters overestimated the wave height reduction of the artificial reef by around 200%, and therefore need to be calibrated with the laboratory data. The model showed that positioning the artificial reef mid-reef or near the shore is most effective, especially in reducing sea/swell waves at the shoreline, while reefs placed at the crest show minimal wave height reduction.

The laboratory results showed a reduction in wave height at the shoreline of 11% at lower water levels and 5% at higher levels. Both sea/swell and infragravity wave components showed similar reductions, even though frequency dependent dissipation was expected, with shorter wave components (sea/swell) dissipating more energy compared to the longer waves (infragravity). The similar reduction rate is likely due to the large orbital velocities and orbital excursion lengths observed on the flat. The numerical model underestimated shoaling in the surfzone (RMSE 0.4 m, $\sim$30% of total wave height) and infragravity wave height on the reef flat (RMSE 0.15 m, $\sim$50%), with sea/swell waves being accurately predicted on the reef flat. Additionally, the inability of the wave generator to generate bound subharmonics with frequencies below 0.02 Hz likely contributed to an increase in infragravity wave energy on the reef flat by approximately 50%.

The results of this thesis show a limited impact of an optimised artificial reef on the reef flat, with effectiveness expected to decrease further as sea levels rise. However, the smaller scale of the reef elements prioritises ecological benefits, and when combined with larger structures or integrated into shoreline protection strategies, these reefs can still offer valuable benefits for biodiversity and wave mitigation. Additionally, further investigation is needed to understand the influence of the limitation of the wave generator on these findings. Nevertheless, the laboratory experiments provide a valuable new dataset on the hydrodynamics of complex canopies, capturing both effects on the wave field and on the in-canopy flow structure. The dataset can be used to calibrate several numerical models and methods of schematising artificial reefs, and broaden our understanding of reef hydrodynamics.

Contents

List of Figures

List of Tables

List of Symbols

α_w^R	Representative attenuation parameter	g	Acceleration due to gravity
$\alpha_{w,j}$	Frequency dependent attenuation parameter	H_S	Significant wave height
α	Coefficient associated to laminar friction less	H_{m0}	Significant (spectral) wave height
β	Coefficient associated to turbulent friction less	H_{SS}	Significant Sea/Swell wave height
η	Water surface elevation	H_{IG}	Significant Infragravity wave height
$\overline{\eta}$	Mean surface elevation (setup)	KC	Keulegan Carpenter number
γ	Breaker parameter	K_t	Transmission coefficient
μ	Frictional coefficient	L	Characteristic wave length
ν	Kinematic viscosity	$L_{m-1,0}$	Wave length associated with $T_{m-1,0}$
ρ_e	Element density	m_0	Spectral moment of order 0
ρ	Porosity	m_1	Spectral moment of order 1
ω	Angular frequency	m_{-1}	Spectral moment of order -1
a	Empirical coefficient	n	Porosity (same as ρ)
b	Empirical coefficient	n_L	Geometric scaling factor
c	Empirical coefficient	$nfft$	Block length
A_∞^{rms}	Root-mean-square orbital excursion length	Q	Discharge
B	Restoration width	R_m	Reynolds number of model
C_f	Friction coefficient	R_p	Reynolds number of prototype
C_D	Drag coefficient	R_c	Freeboard
C_r	Courant number	$RMSE$	Root-Mean-Square-Error
C_m	Inertia coefficient	R^2	Coefficient of determination
D	Element diameter	S_x	Cross-shore element spacing
D_n	Nominal element diameter	S_y	Cross-flume element spacing
F_s	Sampling frequency	T_p	Peak period
F_{peak}	Peak frequency	T_{m01}	Mean wave period
f	Frequency	$T_{m-1,0}$	Mean energy period
$f_{N,n}$	Nth resonance frequency	T_{perc}	Percentage reduction in wave height
$f_{e,j}$	Energy dissipation coefficient	$U_{\infty,w}^{rms}$	RMS free-stream orbital velocity
GF	Groupiness factor	W	Element weight

1

Introduction

Coral islands are highly vulnerable to the effects of sea-level rise and climate change. Because of their low elevation, these islands are prone to wave-induced flooding, endangering their infrastructure and fresh-water supply. These islands are protected by coral reefs, which are not only home to 25 percent of all known marine species, but also protect the island by dissipating wave energy through wave-breaking and bottom friction (Kennedy & Woodroffe, 2002). Despite their importance, coral reefs are currently in decline as they are threatened through a combination of climate change and anthropogenic stressors, such as rising sea temperatures and ocean acidification (Obura et al., 2022). Reef restoration practises in the form of artificial reefs pose a solution to this issue. However, due to cost and operational constraints, reef restorations are of limited spatial extent (Bayraktarov et al., 2019). Additionally, the artificial reefs are often designed to enhance the biodiversity of the system and do not take into account the effect these reefs can have on energy dissipation. Consequently, the effect these restorations have on wave attenuation and coastal flooding is not well understood.

Since performing field experiments to assess the impact of both coral and artificial reefs is challenging and coral reef covers cannot be altered to systematically investigate wave attenuation, researchers often resort to numerical modelling. A study by Roelvink et al. (2021), employing a phase-averaged physics-based numerical model, revealed that on a fringing reef, optimizing reef restorations can effectively reduce wave runup, mitigating coastal flooding. The model is however heavily schematised with the coral reef being represented as an impermeable bottom layer with an increased roughness coefficient. This oversimplification does not take into account the complex interaction of wave-driven flow with the canopy structure of coral reefs.

It is hypothesized that this oversight may lead to different responses in terms of wave dissipation and reflection, subsequently altering the total amount of wave energy reaching the coast, the frequency distribution of this energy (Lowe et al., 2007), and the water level response (Van Rooijen et al., 2016), which are all critical parameters in wave-driven flooding. Lowe (2005a, 2005b, 2007) performed both laboratory experiments and field tests in which he discovered that wave dissipation through a coral reef is frequency dependent, with higher period waves being attenuated more significantly.

Norris et al. (2023) conducted phase-resolving, high-resolution numerical modelling, validating the modification of frequency distribution and total wave energy observed in Lowe's work. However, even though with a much larger resolution, similar to Roelvink's study, the model represented the coral reef as a two-dimensional impermeable bottom layer, failing to accurately describe the three-dimensional flow around the coral canopy and potentially introducing inaccuracies in the results.

Laboratory experiments are a potential solution to address the limitations associated with the heavy parameterisation of coral reef canopies in numerical models. Small-scale laboratory tests performed by Van Wiechen (2020) investigated the impact of complex coral reef structures on wave dissipation. The results showed that higher wave periods and increased coral density contributed to increased dissipation rates. However, the complex flow through the three-dimensional coral canopy structure might not be accurately simulated in small-scale laboratory experiments due to inaccuracies arising

from scale effects. The actual effect of this scaling is not known. Therefore, to overcome this limitation, experiments need to be conducted on a significantly larger scale within a controlled laboratory setup.

1.1. Research Objective & Research Questions

The primary objective of this research is to investigate the impact of artificial reefs, consisting of structures representing a coral canopy, located on the reef flat, on wave transformation and wave-driven flooding of low-lying fringing reef islands. This investigation combines numerical modelling with large-scale laboratory experimentation. The research, known as the CREST project, led by TU Delft, is a collaborative effort between TU Delft, Plymouth University, Deltares, Boskalis, and Coastruction. It extends the ARISE initiative led by Plymouth University, which examines natural adaptations of atoll islands to rising sea levels.

The core of this thesis on the CREST experiments focuses on optimising the setup for the laboratory experiments, as well as a data comparison between the numerical data and the laboratory results. This thesis consists of three distinct parts. The first is the design of the artificial reef restoration to be used in the laboratory, while the second focuses on how this restoration can be positioned to maximise its effectiveness in terms of coastal protection, alongside investigating how the positioning of such an artificial reef influences the energy distribution and wave transformation over a fringing reef. The final part analyses both the laboratory results and makes a comparison with the numerical model. For the numerical modelling the software SWASH is used, while the laboratory experiments are performed in the Deltares Wave Flume, which allows for a scaled-down representation of a coral reef island with a geometric scaling factor of only 3.

Research Questions

The research questions are oriented around the research objective and each question focuses on one of the three distinct parts of the research.

Question 1: Artificial Reef Design

How can an artificial reef restoration be designed and schematized for the use in a large-scale laboratory experiment?

- What are the key parameters characterizing the artificial reef elements that need to be preserved in the lab?
- How can the reef restoration be represented in the numerical model SWASH?

This research question focuses on the design of the artificial reef, consisting of the entire reef and the individual elements making up the reef. Additionally, this artificial reef needs to be schematized numerically in the SWASH model.

Question 2: Experiment Optimisation

How does the positioning and spacing of the artificial reef influence the energy distribution and wave transformation over the reef flat?

- How does the effect on the total wave field and the sea/swell and infragravity waves vary for restorations positioned at different locations on the reef flat?
- How does the density of the artificial reef affect the wave energy reaching the shoreline?

According to Lowe et al. (2007) and Roelvink et al. (2021) both the density and positioning of the artificial reef influence the energy dissipation, which is expected to be different for distinct frequency components of the wave field. This research question is used to not only determine the optimal location and densities for the artificial reef to be used in the lab, but also, through SWASH, to investigate how the positioning and density influence the transformation of the wave energy for these components.

Question 3: Data Analysis & Comparison

How effective is the artificial reef restoration designed for the CREST experiments at reducing wave height, and how does it compare to predictions from the SWASH model?

- How do varying water levels and wave conditions influence the performance of the artificial reef in reducing wave height??
- What are the differences in wave energy propagation and reduction over the reef flat between the laboratory data and the numerical predictions of the SWASH model?

This research question focuses both on the data of the laboratory experiments as well as on how accurately SWASH is able to predict these results. Analysing the dissipation for varying water levels and wave conditions allows for a more thorough and complete image of the reefs' effectiveness. Additionally, the results can be used to inform on the design and implementation of future artificial reefs and their expected effectiveness in wave height reduction.

1.2. Thesis Outline

To answer the research question, the thesis is split into 10 chapter. The first chapter, Chapter 1 introduces the research objectives and questions. Chapter 2 provides all relevant background information on which the research methodology is based.

The general experimental program is covered in Chapter 3, which introduces both the CREST experiments and the overarching ARISE project. The following chapter, Chapter 4, focusses on the design of the artificial reef structures and the numerical modelling approach, addressing Research Question 1.

Chapter 5 explains the data processing and analysis techniques, describing the parameters used to evaluate the effectiveness of the artificial reefs. Following this, Chapter 6 is dedicated to the optimisation of the experimental setup (Research Question 2), examining both the influence of the location of the artificial reef and density.

The following chapter, Chapter 7 focuses on the laboratory data, where an analysis on the laboratory data is performed and a comparison with the SWASH output is conducted. Chapter 8 is dedicated to discussing the results, evaluating limitations, and comparing findings with existing literature. The final chapter, Chapter 9 provides answers to the research questions and concludes with recommendations for future research.

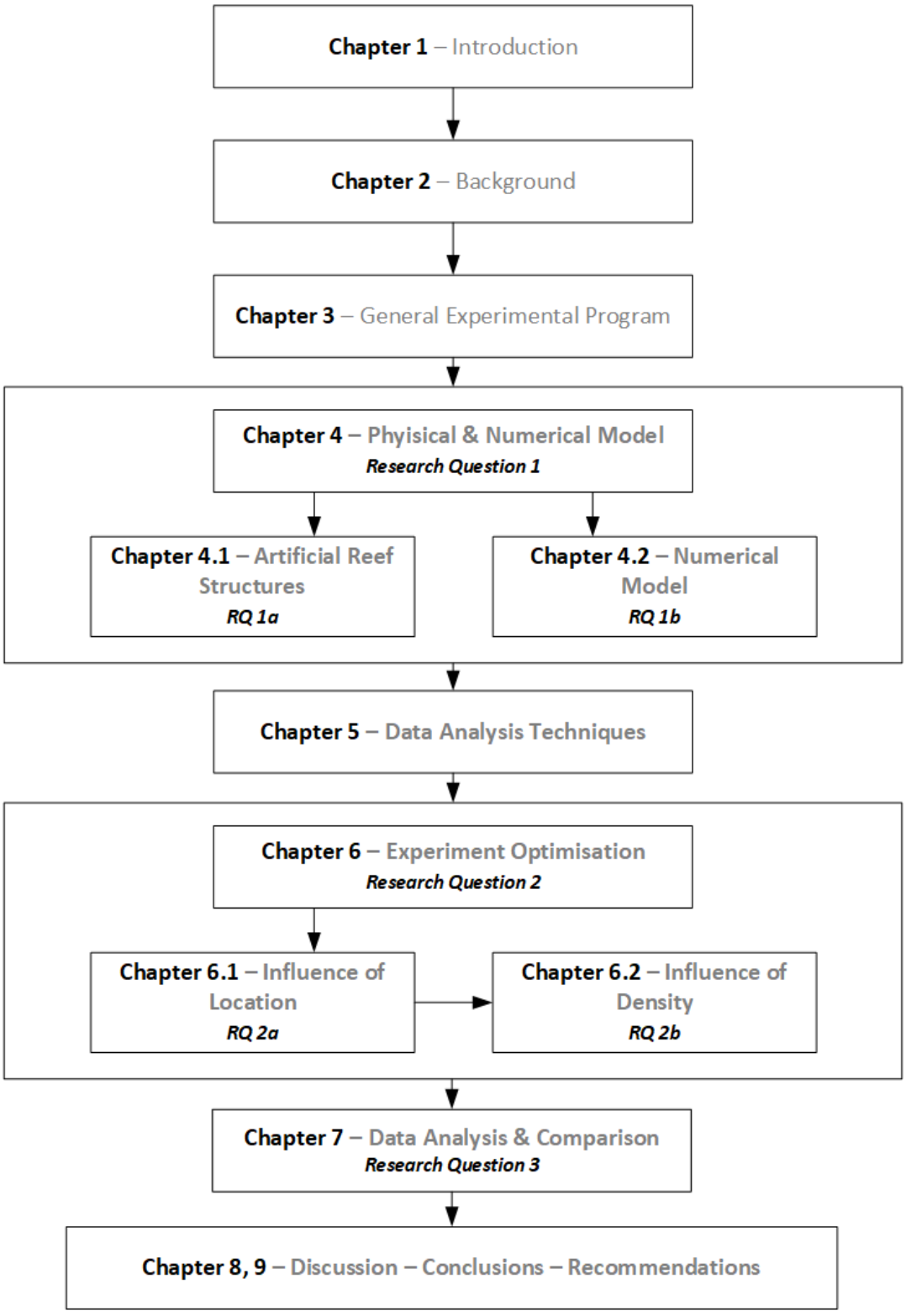

Figure 1.1: Thesis outline

2

Background

The following chapter provides the necessary information on which the research methodology is based. Section 2.1 describes coral reefs and coral islands, along with their associated characteristics, such as reef ecology and the unique concepts of frictional dissipation through canopy flow. The subsequent section, Section 2.2 examines artificial reefs designed to either protect these low-lying fringing reef islands or counter the severe deterioration of global coral reefs. Section 2.3 covers the hydrodynamics of fringing reef systems, including the hydrodynamic forcing, wave transformation, and canopy flow dynamics. Finally, Section 2.4 describes various techniques for modelling coral and artificial reefs, highlighting their limitations.

2.1. Coral Reef Formations

Coral reef formations is a general term that describes both the coral reefs itself as well as their associated coral islands. Coral reefs are limestone structures made up of the calcium carbonate skeletons of small organisms called polyps. When a polyp dies, it leaves behind a skeleton onto which the next generation of polyps can settle. These organisms depend on warm water and sunlight to grow. Therefore, coral reefs are mainly found in the lower latitudes of the Indo-Pacific region (Figure 2.1). Because these islands are formed by living organisms, they are especially vulnerable to climate change compared to more traditional rocky or sandy shorelines.

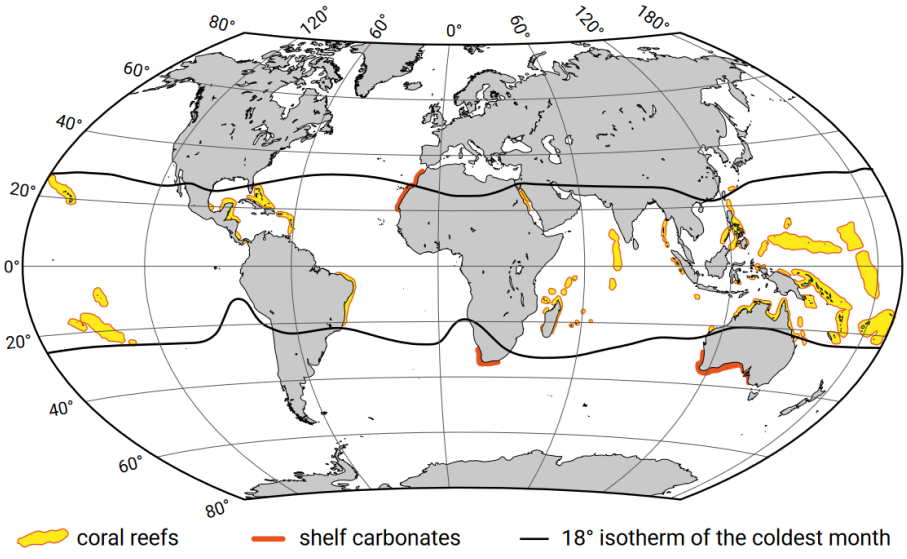

Figure 2.1: Extensive coral reefs can be found in the lower latitudes in the Indo-Pacific region, where they form coral islands and other coral reef formations (Bosboom and Stive, 2021)

Coral reefs can be categorized into three main formations: fringing reefs, barrier reefs, and atolls. Fringing reefs are directly attached to the coastline, while barrier reefs are separated from the coast by a lagoon. Atolls develop from fringing reefs that surround an island, such as a volcanic island. When the land sinks or the sea level rises, the island can become entirely submerged, resulting in a lagoon surrounded by a ring of atolls (see Figure 2.2). On these atolls, small islands can form, typically with elevations less than 3 meters above sea level, which makes them extremely vulnerable to flooding. A well-known example of these atoll formations is the Maldives.

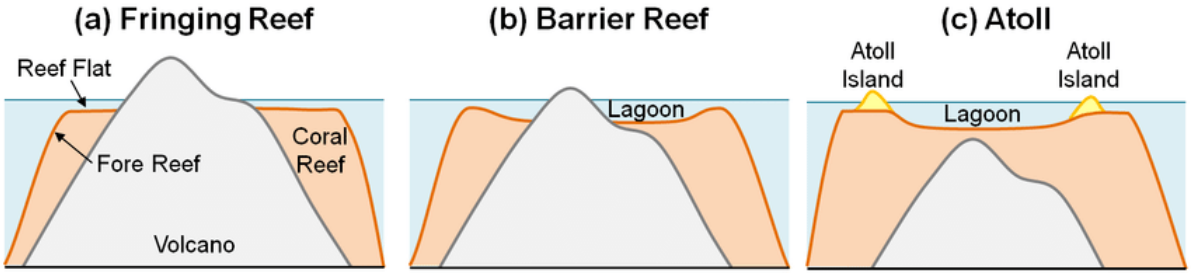

Figure 2.2: Different types of coral reef formations: (a) Fringing reefs, (b) Barrier reefs, and (c) Atolls. (Pearson, 2016)

2.1.1. Reef Morphology

This thesis focuses on atoll islands and fringing reefs due to their similar morphology and hydrodynamic characteristics. Therefore, from now on, coral reef formations will be referred to as ”fringing reefs”, because atoll islands, while distinct, originate from fringing reefs and have similar characteristics. Since barrier reefs are less susceptible to floods, they are not included in this study. Wave setup is caused by radiation stress gradients resulting from wave breaking on the reef edge. The reef flats of both atolls and fringing reefs are bordered by the shoreline, which intensifies this wave setup and increases flood risk. Barrier reefs, however, are separated from the shoreline by a lagoon, which mitigates wave setup and reduces the risk of flooding compared to fringing reefs and atolls.

The morphology of coral reefs is different from that of sandy coastlines. Coral reefs have a steep fore reef that rises abruptly from the ocean floor, creating a sharp transition in bathymetry. In contrast, sandy coastlines generally have a gently sloping beach. Besides the fore reef, coral reefs include a shallow, flat reef area which can be exposed during low tide. The reef flat of fringing reefs is significantly rougher than sandy shorelines and can vary widely, ranging from 10s to 100 s of meters in width (Brodie and Cohn, 2021), with the breakpoint of waves at the offshore edge of the reef flat, called the reef crest.

When compared to sandy shorelines, the distinct morphology of coral reefs results in different hydrodynamic characteristics. Although the the narrow shelves of coral reefs greatly reduces the effects of storm surges, they frequently encounter large significant wave heights, which can exceed 4 meters in height (Bosboom, 2021; Van Dongeren, 2020). Furthermore, while wave breaking dominates the dissipation of waves at sandy shorelines, friction from the hydraulic roughness of the reef plays a large role in the dissipation of wave energy at fringing reefs.

2.1.2. Reef Ecology

Coral reefs are among the most diverse and important ecosystems on the planet. They consist not only of corals, but include many marine species such as fish, algae, sharks, and others that depend on the reefs for food and shelter. Coral reefs provide a habitat for about 25% of all marine species, even though they cover less than 1% of the ocean floor (NOAA, 2023). However, coral reefs are susceptible to environmental changes, especially those driven by climate change and human activities. Stressors such as rising temperatures, ocean acidification, pollution, overfishing, and coastal development threaten coral reefs. Climate change has increased the frequency and intensity of heat stress, while anthropogenic factors like pollution and overfishing threaten the coral reefs. These stressors affect not only the corals themselves but also the many species that rely on the reef for survival.

The most significant threat to coral reefs is rising water temperatures. Due to their sensitivity to temperature, corals can bleach when the water temperature rises by as little as 2 °C. When the connection

between coral and the algae that reside inside their structure is broken, corals bleach. These algae are vital to the health of corals because they supply up to 90% of the energy needed for photosynthesis (NOAA, 2023). Coral may bleach for other reasons, like extremely low tides, pollution, or too much sunlight. While corals can sometimes recover from bleaching events if conditions return to normal quickly, repeated or prolonged bleaching often results in permanent coral death. (WWF, 2023). Globally, the health of coral reefs has severely deteriorated, around 75% of the world's tropical coral reefs have experienced heat stress severe enough to trigger bleaching. For 30% of the world's reefs, that heat-stress was enough to kill the coral.

2.1.3. Frictional Dissipation & Canopy Flow

Coral reefs are not only essential for a healthy ecosystem, they also play an important role in the dissipation of wave energy. Research shows that the roughness of coral formations significantly reduces wave energy and that healthier reefs generally dissipate more energy (Carlot et al., 2023; Monismith et al., 2015; Harris, 2018). Healthy reefs are characterised as reefs with a high roughness and a large structural complexity. A healthy reef has extensive coral cover and a complex, diverse coral structure (Obura, 2022). This combination not only increases the hydraulic roughness of the reef but also increases its structural complexity.

For example, the research of Carlot et al. (2023) showed that if coral roughness is halved, extreme wave run-up events that occur once in a century can become 50 times more frequent. Also, the research of Harris (2018) showed that preserving the structural complexity of coral reefs, therefore increasing their roughness, is the most important factor in protecting low-lying tropical islands from flooding.

A significant study on the effect of coral canopies on wave dissipation is by Lowe (2007, 2005b, 2005a). Lowe conducted both laboratory experiments and field tests, in which he showed that coral reef canopies significantly attenuate wave energy. This attenuation is attributed not only to the structural complexity and increased roughness of the corals but also to the canopy flow dynamics. The magnitude of this energy dissipation depends on the work done by the flow, with wave components that can more readily flow through the canopy are attenuated significantly more than those that cannot. The flow of shorter-wave components is significantly less attenuated than that of larger components and therefore dissipate significantly more energy. These canopy flow dynamics are highly dependent on the density and dimensions of the coral canopy. The concept of canopy flow dynamics is a crucial aspect of this thesis, and therefore a more in-depth discussion of these dynamics is provided in Section 2.3.3.

Further research by Monismith et al. (2015) supports the importance of canopy flow dynamics on energy dissipation. They found that corals with greater structural complexity, or higher relief, create more turbulence in the water column under shorter wave periods and therefore dissipate more energy. Additionally, increasing coral roughness by 13% can result in a 45% increase in wave energy dissipation per meter of coral reef (Norris et al., 2023). Pomeroy et al. (2023) also investigated the impact of complex reef structures on flow attenuation and found that the flow attenuation caused by a coral canopy can be attributed to three parameters regardless of coral species; the coral frontal area per unit reef area, the height of the coral and the water depth. The first two parameters are characterised by the health of the coral canopy.

2.2. Artificial Reefs

Coral reefs play a crucial role in both ecology and as natural coastal protection, therefore their severely declining health has brought forth numerous restoration projects. These restoration efforts serve different purposes, with some prioritising biodiversity while others aim to improve coastal protection. The goal of the restoration largely determines the method and scale of the intervention (Bayraktarov et al., 2019). Generally, reef restorations cover limited areas (on the scale of tens of meters) and are of limited height (0.25 to 1.25 meters) due to the high costs involved. Furthermore, the depth at which restorations can be conducted is restricted by operational challenges, particularly the limitations for divers.

For biodiversity-focused restoration projects, coral colonies are often directly transplanted from nurseries to the fore reef (Figure 2.3a). These types of efforts are rarely conducted on the reef flat, as corals

in this area are exposed to higher wave forces and may become exposed during low tide. Additionally, the reef flat typically lacks suitable substrates for coral attachment, which must be added before transplantation can occur, further increasing costs. As a result, coral density on the reef flat tends to be lower, which reduces the structural complexity and hydraulic roughness of coral canopies compared to those on the fore reef (Chappell, 1980). However, it is the canopies on the reef flat that play the most significant role in dissipating wave energy.

Therefore, coastal protection measures aimed at improving flood safety are often focused on the reef flat. These projects often overlook the potential ecological benefits, such as creating habitats for marine species. Traditional methods, like constructing (submerged) breakwaters (Figure 2.3b), are highly effective at protecting the coast but offer little ecological value and can be damaging to the natural environment. To address this, alternative solutions known as artificial reefs have been developed. Artificial reefs are man-made structures designed to provide habitat for marine life, aligning better with the natural ecosystem. Examples are The MOdular SEalife System (MOSES) made by ReefSystems (2024) (Figure 2.3c) and the Reef Ball designed by the Reef Ball Foundation (Figure 2.3d). Although these artificial reefs are less effective as coastal protection measures compared to traditional structures, they offer a more environmentally friendly option. In locations like the Maldives, where tourism is a major source of income but the islands are highly vulnerable to flooding, artificial reefs present a potential solution. However, because of their novelty, there remains uncertainty regarding how effectively these structures can reduce wave energy, especially for artificial reefs that mimic a natural canopy as accurately as possible. It has been shown by research of Roelvink et al. (2021) that optimising the location of a reef restoration, resembling a natural canopy, can increase flood risk reduction.

(a) Reef nursery for restoration purposes in Florida, USA (NOAA, 2019)

(b) Breakwater at Ellaidhoo, Maldives (Scubaboard, 2022).

(c) MOdular SEalife System (MOSES) (ReefSystems, 2024).

(d) Reef Balls at Sellingan Island, Malaysia (Chen et al., 2018)

Figure 2.3: Different restoration/coastal defence approaches: (a) Coral nurseries for ecological purposes, (b) emerged breakwater for coastal defence, (c) MOSES artificial reefs for both ecology and coastal protection (d) Reef Balls for both ecology and coastal protection.

2.3. Reef Hydrodynamics

Because of the unique morphology of fringing reefs as well as their geological positioning, wave hydrodynamics on these reefs is distinct from any other coastline. The wave energy reaching the shoreline is a function of both the hydrodynamic forcing as well as the transformation of waves over the reef flat.

2.3.1. Hydrodynamic forcing

As shown in Figure 2.1 fringing reefs can be found across almost all longitudes on the globe. Therefore, the hydrodynamic forcing, mainly the water levels and wave conditions, vary strongly per geographical location.

Water Levels

The water levels on fringing reefs play on important role in the hydrodynamic forcing. Because of the low elevation of the reef flats, changes in water level have a large impact on the transmission of waves and therefore on the risk of flooding. These water levels are governed by factors such as tides, wave-induced setup, and changes in sea level, such as sea level rise.

Tidal ranges vary significantly over fringing reefs found around the globe, with the largest ranges exceeding 8 m in magnitude (Lowe et al., 2015). This means the reef flat can be uncovered during low tide, while during high tide the water depth can be several meters high. In general the tidal ranges are substantially smaller. For example Woodworth (2005) found a tidal range of around 1 m for the Maldives, While Becker et al. (2014) found tidal ranges in the pacific to vary between 1 and 1.6 m, with mean water levels of around 0.8 m. Kennedy & Woodroffe (2002) found that water levels over fringing reefs rarely exceed 2 m in height.

Another important factor that determines the water level on a fringing reef, and therefore island flooding, is the wave-induced setup. This setup depends on the intensity or magnitude of wave breaking and the associated radiation stress gradients. The intensity of wave breaking is influenced by both water depth and wave height: greater water depth generally reduces the magnitude of wave breaking and, subsequently, the setup, while higher wave heights increase radiation stress gradients, leading to greater setup (Becker et al., 2014; Cheriton et al.,2016; Vetter et al., 2010). However, even if setup is lower at higher water levels, more energy can still reach the shoreline. As a result, the runup at the shoreline may increase during high tide if there is significant energy present on the reef flat.

Changes in mean sea level can also impact water levels on the reef. Sea level is expected to rise up to 1 m by the end of the century (IPCC, 2023). While it is still unknown how exactly the morphology of coral islands is expected to change with SLR, given their elevation of only several meters above mean sea level, flood risk is guaranteed to increase. SLR not only reduces the effective height of the island above the sea, it also influences the water depth on the reef flat, which influences many hydrodynamic processes. It must also be noted that coral reefs are living organisms, highly depending on light intensity and therefore the water depth. An increase in water depth could lead to less favourable conditions for the corals, which could even further harm their health and therefore their ability to dissipate wave energy effectively. While sea level rise poses a big threat to low-lying fringing reef islands through multiple factors, it falls outside of the scope of this thesis.

Wave Climate

Fringing reefs and atoll islands are primarily located next to an ocean basin, which means that the wave fields at these reefs are dominated by distant swell waves generated from large storms. While fringing reefs share the characteristic of being located next to an ocean basin, different geographical location means fringing reefs are subject to different wave climates. The main interest of this thesis is focused on fringing reefs located in the Indian ocean, more specifically the Maldives, as well as those located in the Pacific ocean region. While fringing reefs with similar morphology and water levels exist in both regions, the wave climates are distinctly different.

The Maldives are positioned in the doldrums (Amores, 2021), which means they experience infrequent and mild storm surges, with cyclones rarely occurring. The extreme wave conditions in the Maldives

are a result of distant swell waves, with limited significant wave height of roughly 1.5 to 3.0 m, but significantly long wave periods between 13 and 16 s. While these swell waves are of limited magnitude, these waves can still pose significant threats to low-lying islands. Fringing reefs in the Pacific are, contrary to those in the Maldives, subject to cyclones and experience more extreme significant wave heights of around 4 m, with periods in the range of 10 s.

Waves can be classified by their frequency into several groups. Since this thesis is focused on the effect of an artificial reef on wave transformation of different wave components a distinction is made between two different wave groups: the sea/swell waves and the infragravity waves (Table 5.1). Sea-swell waves are the combination of locally generated sea waves (1 - 10s) and swell waves generated from distant storms (10 - 33 s). The lower frequency bands are infragravity waves, including all waved with a period larger than 33 s. These infragravity waves are generated on the reef flat itself and depend highly on the reef bathymetry and wave conditions. Since these waves form a core part of this thesis, they are discussed in more detail in Section 2.3.2.

Frequency band		f [hz]	T [s]
H_{SS}	Sea/Swell	0.03 - 1	1 - 33
H_{IG}	Infragravity	<0.03	>33

Table 2.1: For this thesis the wave field is separated into two frequency bands: the sea/swell waves H_{SS} and the infragravity waves H_{IG}.

2.3.2. Wave Transformation over a Fringing Reef

Wave transformation processes on coral reefs significantly differ from those on a typical sandy coast, which is mainly due to the different morphology. The narrow shelves and steep coasts cause wave-driven processes to be of more importance. Offshore sea-swell waves approaching the reef shoal quickly on the steep fore reef to then heavily break on the reef crest dissipating a large amount of energy and resulting in setup over the reef. The waves continue to lose energy over the flat through friction caused by the coral canopy. Through non-linear processes energy is transferred from the sea-swell band to the infragravity waves, which continues to happen up until the shoreline (Van Dongeren, 2020). The waves, especially the low frequency components, reflect on the reef crest as well as on the shoreline. The morphology and characteristics of a fringing reef is very efficient at dissipating energy, with shallower, rougher and wider reefs more efficient at dissipating this energy (Pomeroy et al., 2012).

Offshore, the wave spectrum is dominated by a single peak in the sea/swell domain, towards the shoreline this peak shifts to the infragravity wave spectrum. Cheriton et al. (2016) found that energy distribution over the flat is frequency dependent, with the wave energy gradually shifting over the flat from high frequencies at the crest to low frequencies at the shoreline. Pomeroy et al. (2015), Lowe et al. (2005a) and Van Dongeren et al. (2013) found the same, high frequency waves are dissipated at the reef crest, while low frequencies dominate over the reef flat. While infragravity waves also shoal at the crest, they do not break as violently and instead gain energy over the flat. Figure 2.4 shows an overview of the main hydrodynamic processes over a fringing reef.

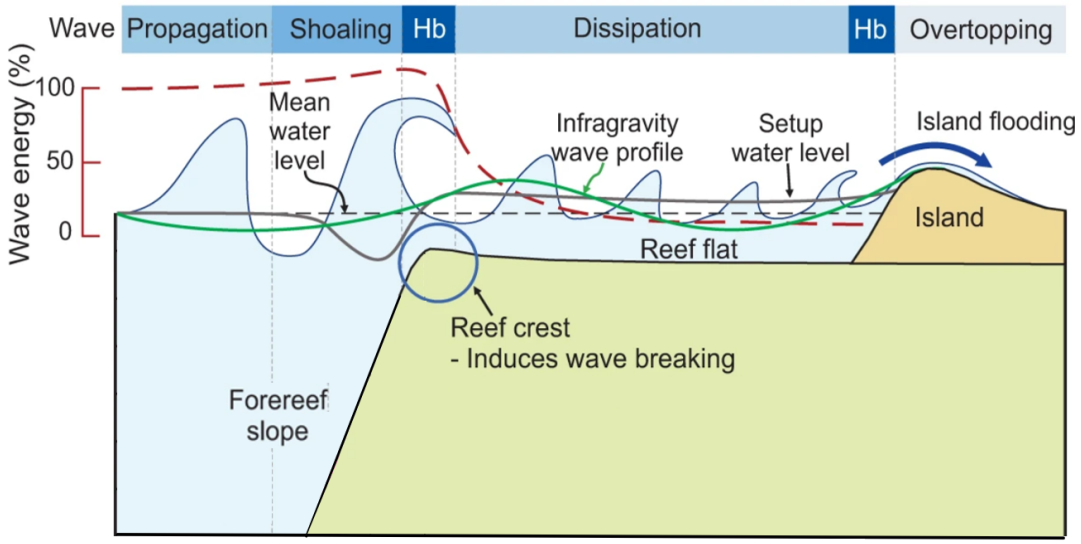

Figure 2.4: Summary of wave process interactions with a fringing reef. Waves shoal as they approach the reef and break on the reef crest (Hb), which leads to a water level setup at the shoreline. The waves continue to lose energy over the reef flat through bottom friction. The water level setup and infragravity waves can lead to island flooding (altered from Kench et al. (2002).

Breakpoint Forcing

As mentioned, low frequency (infragravity) wave components are an important phenomenon on fringing reefs. On sandy shorelines low frequency waves are often generated as bound long waves, or surf beat. Due to wave height variation of sea/swell waves travelling in groups, the radiation stresses vary as well, being highest under the highest waves. This results in a time-varying set-down in the shoaling zone, with the largest depression under the highest waves. The effect of this is a long wave motion on the wave group scale. These waves are therefore 'bound' to the short waves. However, because of the strong wave breaking and the narrow shoaling zone, Pomeroy et al. (2012) found that bound long waves barely contribute to infragravity wave energy on the reef. Instead the infragravity waves are formed through breakpoint forcing (Symonds et al. 1982).

Symonds et al. (1982) first described infragravity wave formation through breakpoint forcing. Unlike bound long waves, which are tied directly to wave height variations within groups of incident waves, breakpoint forcing occurs as the breakpoint shifts both in space and time. This shifting breakpoint creates two long waves, one moving toward shore and one moving seaward. The shoreward-directed wave forms a standing wave which is largely unaffected by changes in incident wave height. Larger incident waves break farther offshore in deeper waters, and smaller waves break closer to shore. This leads to differences in radiation stress gradients and therefore to a different setup at the shoreline, which varies in time at the wave group scale. Because of the steep slope of the fore reef, and therefore the small width of this surf zone, the dynamic setup caused by breakpoint forcing can be significant (Figure: 2.5)

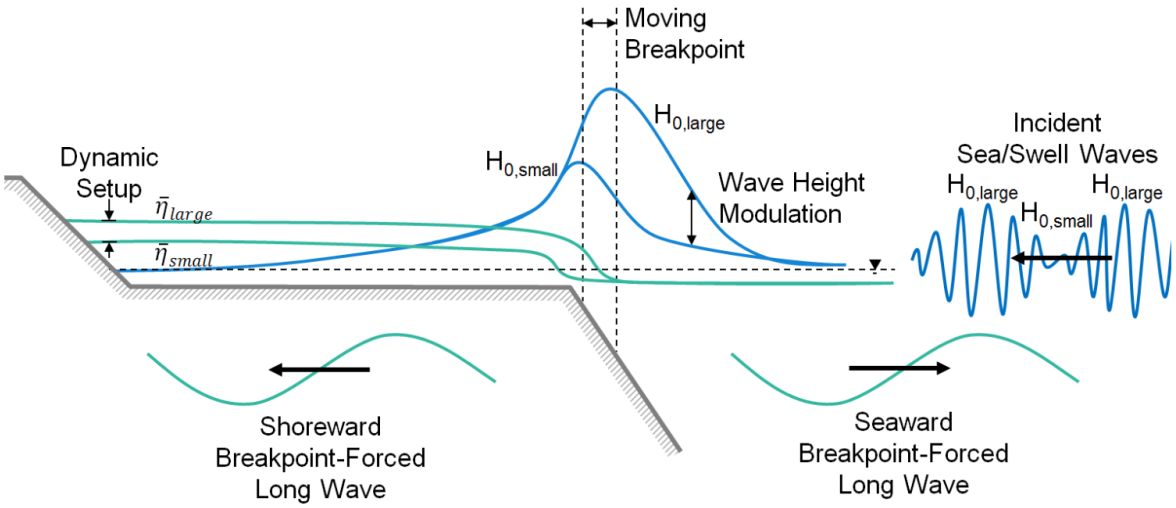

Figure 2.5: The morphology of fringing reefs leads to long-wave generation through breakpoint forcing. Larger incident sea/swell waves break further offshore and create a larger setup than smaller incident waves, which break closer onshore. This moving breakpoint leads to a dynamic setup at the shoreline (Pearson et al., 2016).

2.3.3. Canopy Flow Dynamics

The friction dominated energy dissipation on the reef flat is often attributed to canopy flow dynamics. The magnitude of the dissipation depends on the ability of the flow to move through the canopy, with wave components that can more readily flow through the canopy, dissipated significantly more. This theory was first proposed by Lowe (2005a;2005a;2007) and his work forms the basis for most subsequent research on canopy flows. Lowe investigated the applicability of science-based theories on in-canopy flow dynamics through experiments, employing both small-scale laboratory experiments and field measurements with arrays of vertically mounted circular cylinders representing the coral canopy. He found that shorter wave components can more readily flow through a canopy and therefore dissipate more energy than longer wave components. This hypothesis is further supported by research of Norris er al. (2023) who conducted phase-resolving, high resolution numerical modelling. Their study validated the theory that greater energy dissipation occurs under shorter-wave components.

According to Lowe (2007) the spectral wave dissipation is frequency dependent and depends on the attenuation of the in-canopy flow. Lowe relates the frequency-dependent energy dissipation $f_{e,j}$ to the canopy geometry as well as to an attenuation parameter α_w (Equation 2.1).

$$f_{e,j} = C_f + C_d \lambda_f \alpha_w^R \alpha_{w,j}^2 \tag{2.1}$$

In Equation 2.1 C_f and C_d are the friction and drag coefficient respectively. λ_f is based on the geometry of the canopy. The equation contains two attenuation parameters: α_w^R and $\alpha_{w,j}$. α_w^R is a representative attenuation parameter and $\alpha_{w,j}$ is a frequency dependent attenuation parameter. The attenuation parameters take a value between 0 and 1, with a higher value meaning a lower attenuation of the flow and therefore a higher dissipation of energy. These parameters are calculated as follows:

$$\alpha_w^R = \frac{\hat{U}_w^{rms}}{U_{\infty,w}^{rms}}, \qquad \alpha_{w,j} = \left(\frac{\hat{S}_{U,i}}{S_{U,i}}\right)^{1/2} \tag{2.2}$$

α_w^R depends on the ratio of the root-mean-squared in-canopy velocity $\hat{U}_w^{rms}$ and root-mean-squared free-stream velocity, or the velocity far above the canopy $U_{\infty,w}^{rms}$. $\alpha_{w,j}$ is frequency dependent and depends on the wave velocity spectrum both in-canopy $\hat{S}_{U,i}$ and above canopy $S_{U,i}$.

While it is possible to compute these values, Lowe derived a method to estimate the values of these parameters based on the the root-mean-squared orbital excursion length of the free-stream potential

flow A_{∞}^{rms} as well as the spacing of the in-canopy elements. He defined the orbital excursion length as $U_{\infty,w}^{rms}/\omega$ where $U_{\infty,w}^{rms}$ represents the root-mean-squared velocity of the free-stream potential flow, and ω is the representative angular frequency based on the spectral period T_{m01}

To predict the attenuation parameter, Lowe identifies three distinct flow regimes: inertia-dominated flow, general flow, and unidirectional flow. These regimes are based on the relationship between the attenuation parameter, the excursion length A_{∞}^{rms}, and the element spacing S (see Figure (2.6).

- *Inertia-dominated flow*: In this flow regime A_{∞}^{rms} / S < 1, which means that the orbital excursion length is smaller than the element spacing S, therefore the inertia force dominates.
- *General flow*: In this regime no forces can be neglected and therefore the attenuation parameter is dependent on both the canopy density as well as the excursion length.
- *Unidirectional flow*: here the flow is non-oscillating and dominated by shear forces. This means that the attenuation parameter is independent of the excursion length.

Figure 2.6 illustrates these flow regimes, showing that oscillatory (non-unidirectional) flow has a higher attenuation parameter, thereby dissipating more energy.

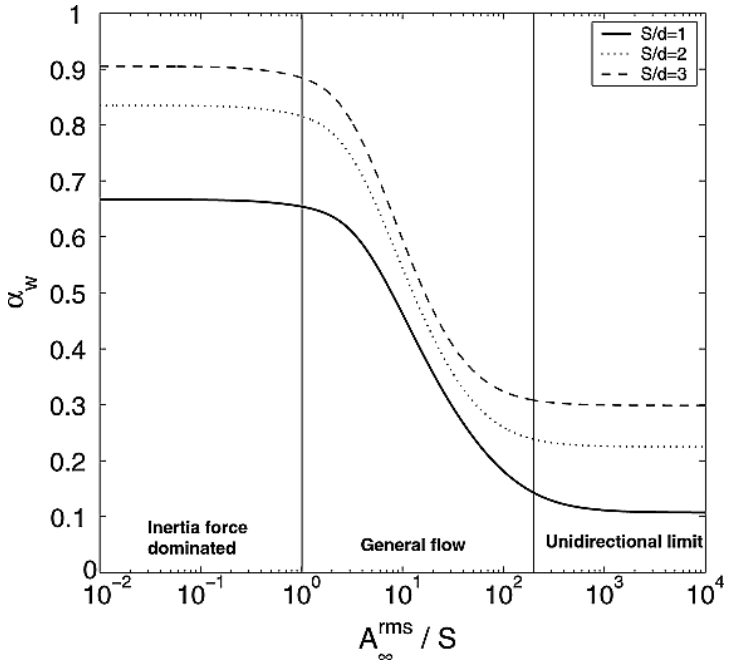

Figure 2.6: Flow regimes according to Lowe (2007), showing the three regimes. The attenuation parameter α_w^R is dependent on spacing S/d as well as the orbital excursion length A_{∞}^{rms}.

For the frequency dependent attenuation parameter, Lowe relates the magnitude of this value to the orbital velocities and the specific wave period component. Figure 2.7 shows that for higher periods, so lower frequency components, the attenuation parameter decreases. It also shows that for higher orbital velocities the attenuation parameter decreases rapidly.

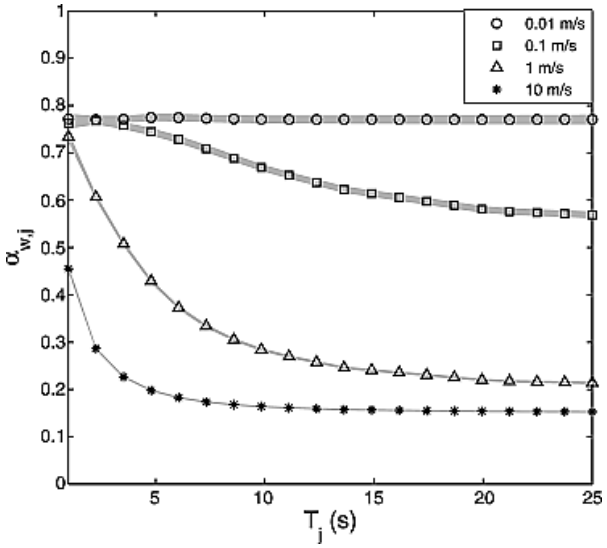

Figure 2.7: The frequency dependent attenuation parameter $\alpha_{w,j}$ depends on the period T of the wave component and the orbital velocities (Lowe et al., 2007).

In-Canopy Flow Structure

To understand and predict the effect of in-canopy flow on wave attenuation, it is crucial to accurately characterise the flow structure within the canopy, describing the spatial variation in in-canopy flow velocities. Due to the complex geometry of a canopy, there is significant spatial variability in flow velocities.

Research by Gijón et al. (2021) investigated wave transmission through dense cylinder arrays, describing in-canopy flow as a function of cylinder spacing and location within the canopy (Figure 2.8). They identified two distinct flow regions: an accelerated flow zone and a sheltered zone. Flow accelerates between the cylinders, while a wake forms directly behind each cylinder, resulting in reduced flow velocities. The extent of these acceleration and deceleration effects is influenced by the spacing between cylinders in both the cross-shore and alongshore directions. Consequently, when conducting laboratory experiments, it is essential to measure the vertical flow structure at these specific locations within the canopy to effectively characterise the complete in-canopy flow structure.

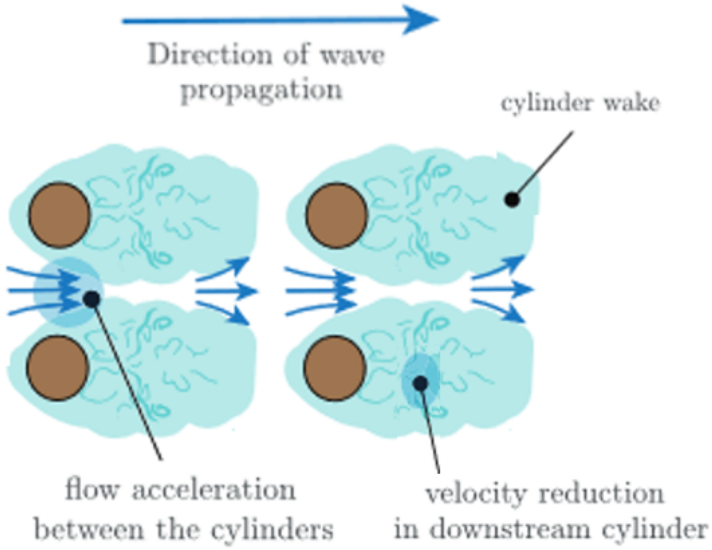

Figure 2.8: The flow in between the elements is accelerated, with a wake forming downstream of the elements in which the flow velocities are reduced (altered from Gijón et al., 2021).

2.4. Modelling Techniques

Various modelling techniques are used to model fringing reefs and artificial reefs, with a common approach being the combination of field research and numerical modelling. In this section several approaches to modelling are discussed. For each modelling approach, the limitations are examined and discussed. It also discusses several techniques of schematising artificial reefs in a numerical model.

Canopy flow dynamics

Both Lowe et al. (2005a;2005b;2007) and Van Wiechen (2020) combined laboratory experiments and numerical modelling to investigate canopy flow dynamics. Lowe's work forms the basis for most subsequent research on canopy flows of which it's results have previously been discussed. They investigated in-canopy flow dynamics through experiments, employing measurements with arrays of vertically mounted circular cylinders representing the coral canopy. While the results agreed with the hypothesised theory, using cylinders is an oversimplification of a real-world coral canopy. A problem with the model of Lowe is that it requires heavy parametrisation of the coral canopy, which was relatively straightforward for arrays of cylinders, but does not translate directly to real-world coral canopies. On the other hand, Van Wiechen (2020) used more complex shapes than cylinders, but scale-effect may limit the validity of those results.

Most other studies combined numerical modelling with field observations, but both the objective and complexity of the models employed vary. Monismith et al. (2015) expanded upon the work of Lowe and investigated the roughness of a reef at an atoll island. The findings showed a large friction factor which was attributed to the complex canopy structure of the reef, believed to be in a healthy state. The observed friction factor was larger than could be expected from Lowe's theory. This is because attributing a complex structure to a variable like the friction factor, especially when this factor is computed from simplified configurations such as a cylinder array, induces errors.

Norris et al. (2023) and Pomeroy et al. (2023) investigated the impact of complex reef structures on flow attenuation. Norris focused on turbulence, while Pomeroy examined flow attenuation for various coral species. Both studies build on the previous work of Lowe and employed high-resolution computational fluid dynamics (CFD) simulations, validated with field observations or small-scale laboratory experiments.

Norris' CFD model treated the bed as impermeable, and although roughness is modelled with a function to describe turbulent boundary layers, treating the bed as impermeable does not allow for flows through the coral canopies. While Pomeroy's model was able to simulate the 3D flow around coral canopies, it assumed a constant drag coefficient, neglecting variations due to the health of the canopies. Also, Pomeroy's research focused only on steady flow attenuation and did not account for unsteady oscillatory flow induced by waves. In contrast, Norris investigated spectral wave dissipation but did not show its translation to the shoreline. This limitation restricts the applicability of both studies to assess flood risk reduction.

Flood risk assessment

On the other hand, the studies of Carlot et al. (2023) and Roelvink et al. (2021) investigated runup and consequently flooding on coral reef coasts. Carlot et al. used a Boussinesq-type model which utilised a bed friction coefficient f_w, dependent on the hydrodynamic conditions and the Nikuradse roughness obtained from field observations. Model runs were assessed using the 2% exceedance wave run-up height as a proxy, in which a distinction was made between healthy and unhealthy coral reefs by means of their structural complexity. However, the research did not specify attenuation of the specific wave components and the impact of simplifying the complex canopy structure. This limitation comes from the Boussinesq model's inability to explicitly describe the vertical flow velocity field, making the modelling of interaction with roughness elements challenging.

Roelvink et al. (2021) used the non-hydrostatic version of XBeach to solve wave evolution of both short and infragravity waves to investigate the effect of reef restorations on different reef profiles. In the model, the reef was represented as an impermeable layer with a friction coefficient f_w of 0.15 for 90–100% coral cover and 0.01 for no coral cover. The results showed that the location of reef restorations can be optimized to reduce coastal flooding. However, the results lack validation, as no laboratory or field experiments were conducted.

3

General Experimental Program

This thesis is part of the CREST project and focuses both on optimising the setup for the laboratory experiments by designing the artificial reef elements and determining the location at which these elements should be placed, as well as investigating in more depth what such a restoration project does to the wave field.

By performing large-scale experiments, not only can we gain insights into the interaction between reef structures and waves, we can also identify the limitations of numerical modelling techniques. However, despite the advantages of large-scale experimentation, acquiring data in a laboratory setting comes with limitations. Measurement devices, which not only have inaccuracies, can only be deployed at a limited number of locations. Additionally, laboratory experiments require a schematisation of an actual reef system and a simplification of a reef canopy. Nevertheless, the controlled conditions of a laboratory setup simplify acquiring data compared to a field research, and the large-scale setup significantly minimises errors resulting from scaling effects.

This chapter presents the research methodology for the general experimental program of the ARISE and CREST projects. It begins with an overview of the research context. Then, the laboratory experiment setup is described, covering aspects such as bathymetry, water levels, and hydrodynamic conditions. Finally, the chapter details the instrumentation used during experimentation.

3.1. Research Context: ARISE & CREST

The CREST project is an extension of the ARISE project, which is led by Plymouth University and is focused on investigating the natural adaptation of atoll islands to sea-level rise. The ARISE project consists of both field experiments in the Maldives as well as large-scale laboratory experiments in the Delta Flume at Deltares. The laboratory experiments extend over a period of roughly two months in which both hydrodynamic and morphodynamic tests are performed on a coral island. ARISE is in charge of the design of the coral island as well as of the planning of the experiments.

CREST extends on the ARISE project and investigates the impact of reef restorations, located on the reef flat, on wave transformation and wave-driven flooding of coral islands. CREST, led by TU Delft, is a collaboration between TU Delft, Boskalis, Coastruction, Deltares and Plymouth University and involves roughly ten days of hydrodynamic testing of the total of two months available for the ARISE project. The hydrodynamic conditions used during testing are determined in collaboration with the involved parties and are mainly governed by the ARISE experiments.

3.2. Laboratory Experiment

The laboratory experiment is designed by Plymouth University, who is in charge of the ARISE project and is performed in the Delta Flume, a unique test facility located at Deltares in Delft, The Netherlands. This wave flume is one of the largest in the world, measuring 300 m in length, 9.5 m in height, and 5

m in width. The design of the coral island and its reef structure resembles that of Fiyoaree Island in the Maldives, scaled down by a geometric factor of 3. In contrast, prior experiments addressing reef hydrodynamics have only been able to scale to an extend around 10 times further from reality.

The laboratory setup resembles that of a fringing reef, characterized by a flat and relatively narrow width of 45 m. The fore reef is steep, with a slope of 1:5 and a height of 5 m. The coral island has a limited extent of 60 m, with a front height of 1.0 m above the reef flat. The spatial extend of the potential reef restoration is limited to roughly 10 m, which is in accordance with restoration projects performed in the field that are spatially restricted due to cost and operational constraints (Figure 3.1).

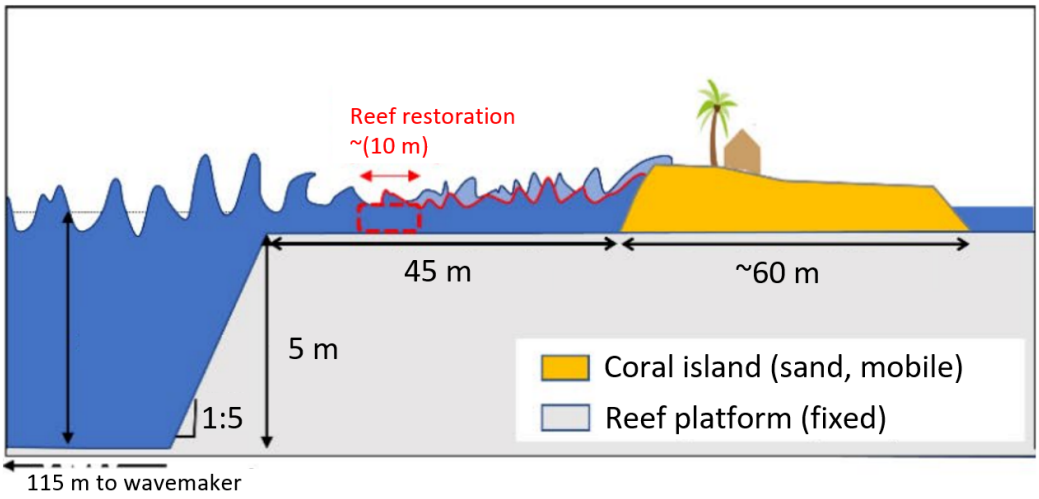

Figure 3.1: Setup of the large-scale lab experiments planned in this project with the restoration area indicated by the dashed red frame. The potential effect of reef restoration is illustrated by the two shades of blue used to represent the waves approaching the island (light blue: waves on the unrestored reef, dark blue: restored reef leading to a reduced wave runup at the beach).

The dimensions of the reef designed for the laboratory experiments are designed for the ARISE project and are modelled after typical fringing reefs found in the Indian and Pacific Oceans, specifically representing the island of Fiyoaree. This island, situated in the southern part of the Maldives, within the Indian Ocean, is the location of the field study site for the ARISE project. The fringing reef features an island with a width of 60 m and an elevation of 1 m, which, when scaled up by a geometric scaling factor of 3, corresponds to a prototype width of 180 m and an elevation of 3 m. The reef also includes a narrow reef platform measuring 45 m in the laboratory model, equivalent to 135 m at prototype scale. This relatively narrow configuration was selected because narrower reefs are more vulnerable to flooding.

The water level in the experiments range between 0.17 and 0.67 m, reflecting conditions similar as found on fringing reefs in the Indian and Pacific Oceans, where water depths reach up to 2 m at real-life scale. Table 3.1 provides the scaled-down dimensions of the fringing reef island as used in the wave flume, with a geometric scaling factor of 3 applied to prototype dimensions.

Variable	Unit	Delta Flume	Prototype
Island width	[m]	60	180
Platform width	[m]	45	135
Island elevation	[m]	1	3
Water depth across platform	[m]	0.17 - 0.67	0.5 - 2.0

Table 3.1: Reef dimensions for both the prototype case (real-life) and the values used in the Delta Flume, which are scaled with a geometric scaling factor of 3. The fringing reef is designed for the ARISE project, by Plymouth University.

Hydrodynamic Conditions

The CREST experiments are performed over a period of 10 days, during which three distinct configurations of roughness elements are tested under various water levels, wave heights, and wave periods. These configurations consist of the base case, without any roughness elements and two cases involving different densities of roughness elements positioned at the same location on the reef flat. The wave conditions and water levels are based on those used for the experimental runs of the ARISE project. A total of five wave conditions are tested for each configuration, combined with two water levels. These wave conditions are representative of environments in the Indian and Pacific Oceans.

The Maldives, located in the Indian Ocean, experience infrequent and mild storm surges, with cyclones rarely occurring. The extreme water levels at Fiyoaree are a result of distant swell waves, with relative limited significant wave heights and relatively large periods Nonetheless, fringing reefs with similar characteristics exist in the Pacific Ocean, therefore extreme wave events induced by cyclones are also taken into consideration. These conditions are governed by larger wave heights and shorter periods. The experiments account for both mild and extreme wave conditions found in these oceans.

While ARISE tests four water levels ranging from 0.17 m to 0.67 m of water depth on the reef flat, time constraints forces limiting the use of only two water levels for the CREST experiments. The height of the artificial reef elements was chosen at 0.25 m, of which the design is discussed in Section 4.1. Therefore, chosen is to use only water level 0.33 m and 0.67 m, ensuring the elements are fully submerged during testing.

Table 3.2 shows the hydrodynamic conditions and the water levels used for testing, along with their naming convention as used for the ARISE project. The wave conditions cover both mild conditions as found in the Indian and Pacific Oceans (C3 and C1, respectively) to more extreme conditions (C9 and C11, respectively). The duration of each run is 55 minutes, allowing for startup and ensuring a sufficient number of waves in the time series for an accurate analysis.

Wave Conditions				
Name	**Delta Flume**		**Prototype**	
	H_S **[m]**	T_p **[s]**	H_S **[m]**	T_p **[s]**
C1	0.5	5.77	1.5	10
C3	0.5	9.24	1.5	16
C7	1.0	5.77	3.0	10
C9	1.0	7.51	3.0	13
C11	1.3	5.77	4.0	10

Water Levels		
Name	**Height [m] (Delta Flume)**	**Height [m] (Prototype)**
WL33	0.33	1.0
WL67	0.67	2.0

Table 3.2: Offshore wave conditions and water levels used during experimentation expressed in terms of offshore significant wave height H_S and peak period T_p. Conditions **C1**, **C7**, and **C11** represent Pacific Ocean scenarios, while **C3** and **C9** correspond to Maldives (Indian Ocean) conditions.

The wave time-series is imposed at the wave generator using a JONSWAP spectrum with a shape factor (γ) of 3.3. Since the JONSWAP spectrum does not account for the bound harmonics created by non-linear wave interactions, second-order stirring of the wave paddle is used to generate these harmonics. However, due to the technical limitations of the wave maker, only bound subharmonic waves with frequencies larger than 0.02 Hz can be generated. Additionally, active reflection compensation is employed to reduce wave reflections.

Scaling

Various scaling laws exist for hydrodynamic testing, with the most commonly used for laboratory experiments are Froude scaling and Reynolds scaling. Froude scaling laws aim to scale each parameter such that the Froude number remains constant, while Reynolds scaling laws do the same for the Reynolds number. Froude scaling is preferred for experiments in which gravitational forces are dominant, which is the case for free surface flows, such as waves. Reynolds scaling is applied for cases where viscous forces are the dominant forces, which is often the case for small-scale turbulence and boundary layer type experiments. Since the laboratory experiments are performed on a large scale, Froude scaling is applied for the ARISE and CREST experiments.

As mentioned, a geometric scaling factor of 3 is applied for the laboratory setup. The scaling factor n_n for other properties n such that the Froude number remains constant is as follows:

$$Fr_p = Fr_m \qquad \rightarrow \qquad \frac{u_p}{\sqrt{g_p * L_p}} = \frac{u_m}{\sqrt{g_m * L_m}} \tag{3.1}$$

$$n_L = \frac{L_p}{L_m} = 3, \qquad n_v = \sqrt{n_L} = \sqrt{3}, \qquad n_T = \sqrt{n_L} = \sqrt{3} \tag{3.2}$$

This means that the length scales are scaled with a factor of 3, while corresponding velocity and time scales, i.e. flow velocities and wave periods, are scaled with a factor $\sqrt{3}$.

Instrumentation

The ARISE project employs various instruments for data acquisition. Here only those instruments used for the CREST experiments are presented. Figure 3.2 and 3.3 provide a visual overview of the experimental setup, indicating the placement of various instruments. This setup includes offshore wave gauges, 15 pressure sensors (DRO), and 10 flow meters (EMS) distributed from offshore to more densely concentrated areas over the reef flat. By co-locating flow meters and pressure sensors, the wave time-series can be decomposed into incoming and outgoing wave components, as detailed further in Chapter 5. Table A.1 in Appendix A details the precise locations of the 15 pressure sensors (DRO) and 10 flow meters (EMS), along with their corresponding naming conventions, as depicted in the laboratory setup shown in Figure A.1.

The instruments measure at a frequency of 120 Hz, and a runup berm is incorporated into the laboratory setup. This berm prevents overtopping and therefore significant reshaping of the coral island during hydrodynamic testing, which is essential to maintain the conditions for the ARISE project after the CREST experiments are performed. Additionally, significant reshaping of the beach during experimental runs can change the reflection patterns and therefore influence the results negatively. An indication of the positioning of the artificial reef on the reef flat is also shown in Figure 3.2, extending 10 meters in length. Within the canopy of the artificial reef canopy, six Acoustic Doppler Velocimeters (Vectrinos) are positioned to capture the in-canopy flow structure, positioned such that it represents the overall flow characteristics within the canopy. Further details on the precise positioning of these Vectrinos are provided in Chapter 6.

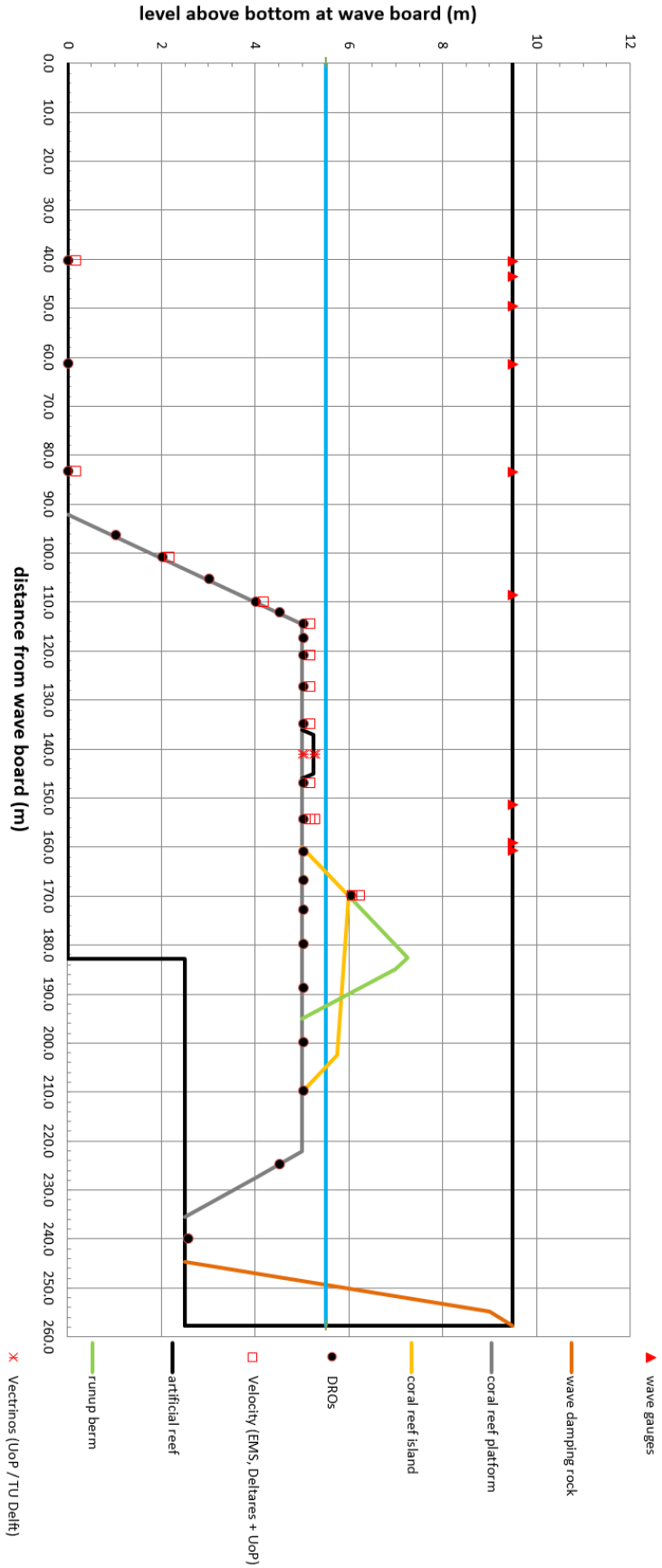

Figure 3.2: Side view of the experimental setup in the Delta Flume, including all the locations for the wave gauges, pressure sensors (DRO) and velocity meters (EMS). A set of pressure sensors and velocity meters is positioned directly in front and behind the artificial reef, such that the exact effect of the reef on the wave field can be examined.

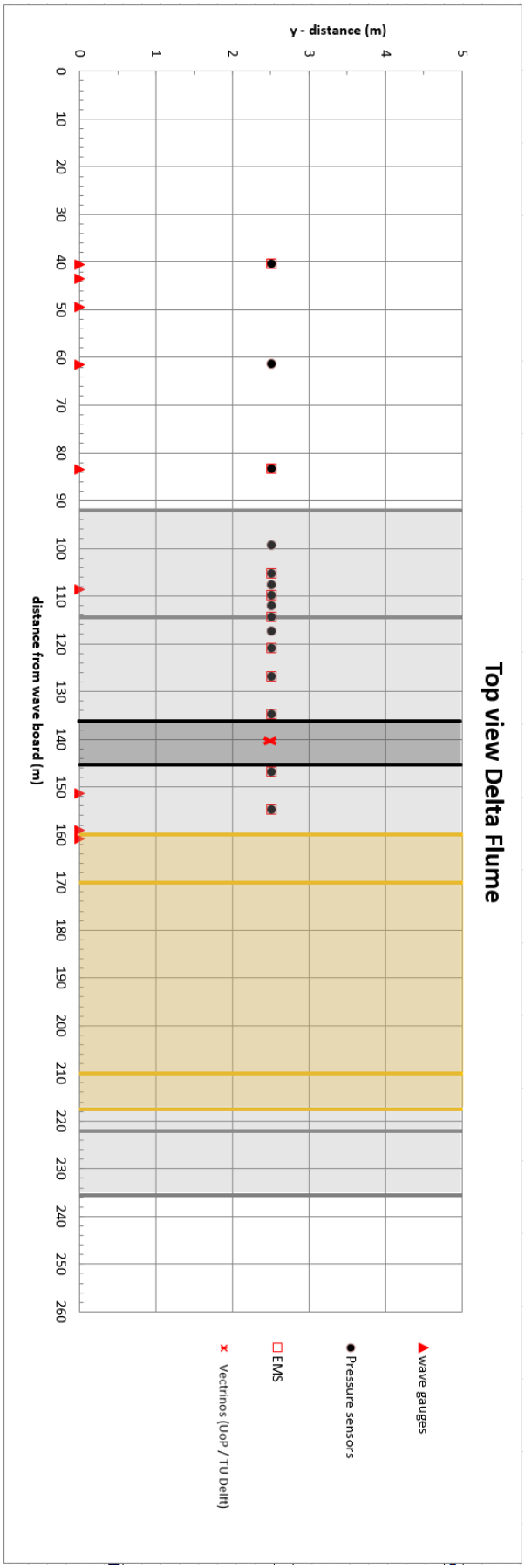

Figure 3.3: Top view of the experimental setup. All pressure sensors and velocity meters are positioned in the middle of the flume to minimise boundary effects induced by the walls of the flume.

4

Physical & Numerical Model

For the laboratory experiments, an artificial reef has to be designed. Additionally, numerical simulations need to be performed and analysed to optimise the positioning and density of the artificial reef structures as well as to investigate the effect of these reefs on the wave field. This chapter starts with a section detailing the design of the artificial reef structures. The design focuses both on the design of the individual elements as well as potential configurations to be used in the laboratory.

Next, the numerical model SWASH is introduced, which includes a description of the schematisation of the artificial reef. Additionally, this section describes the numerical setup and the simulations used to analyse the impact of the reefs on the wave dynamics.

Also, an initial assessment of the modelling approach is performed to investigate its limitations. The chapter concludes by addressing the first research question, which covers both the design as well as the numerical schematisation of the artificial reef.

4.1. Artificial Reef Structures

For the laboratory experiments, an artificial reef, consisting of individual 3D reef elements is constructed. These elements aim to represent a real-world coral canopy as accurately as possible, while also be designed such that it can effectively mitigate wave energy as well as allowing for reliable assessments of the results. The 3D reef models are printed by Coastruction, a company specialised in designing and producing naturally shaped artificial reefs. Coastruction uses a powder bed technology that allows for the printing of complex shapes with a resolution of 2.5 mm. The printed material is a sand-cement mixture with water as a liquid binder. Their printer can produce elements up to one cubic meter and their printed reefs have shown to be able to form an efficient substrate for marine live.

The design of an artificial reef is governed by the specific requirement. Therefore, to create a representative 3D model, the requirements have to be precisely defined. The objective for the design is to create a naturally-shaped artificial reef which enhances the biodiversity on the reef flat as well as increase the efficacy of reef restorations as coastal protection measures. Therefore, the requirements are divided into two parts; one part focuses on the requirements for increasing the biodiversity, such as providing habitats for both coral and fish species, while the other part focuses on the requirements for the engineering purpose of the design, such as ensuring reliable measurements of the canopy flow dynamics during experimentation as well as ensuring sufficient dissipation of the wave energy.

The design is also governed by several physical and time constraints. For example, the roughness elements need to be manually placed on the reef flat for testing, imposing a weight restriction of a maximum of 40 kg to be handled by two persons. Also, the spatial extend is limited to 10 m, which is in accordance with artificial reefs and restoration performed in the field, due to the high cost. In collaboration with Coastruction, a representative 3D model of a coral canopy is constructed based on these requirements.

4.1.1. Requirements

The requirements for the artificial reef are approached from both an ecological as well as an engineering perspective, of which for the purpose of this research the engineering requirements are most important. The requirements not only dictate the shape and size of an individual element, but also that of the entire artificial reef system, so the spatial extend, grid configuration and density. The final design balances these requirements as much as possible in the context of this laboratory experiment.

Engineering requirements

- *Dissipation:*
  According to research of Pomeroy et al. (2023) the dissipation of a reef can be attributed to the frontal area per unit reef area as well as the height of the reef. Also, more complex canopies, so canopies with large variation in shapes over short length scales, have a larger friction coefficient and therefore dissipate more energy (Monismith et al., 2015). The dissipation of the artificial reef can therefore be maximised by either increasing the size and complexity of a single element or by increasing the density and orientation in which they are placed.
- *Stability:*
  Another important requirement is the stability of the elements. A section will be dedicated to determining the stability of the individual elements according to the Morison Equation described in Chapter 6. Larger elements with a lower porosity are expected to be more stable than those that are not. In the design this parameter is not as stringent as the others, it is however crucial that the stability criteria is tested to ensure stable elements during the performing of the experiments. If the elements are deemed unstable, subsequent measures have to be taken to ensure their stability during testing.
- *Canopy flow:*
  An important research gap regarding complex structures is that of canopy flow dynamics and its effect on wave transformation. Lowe et al. (2007) categorised the flow of a canopy into three regimes, which are based on the (frequency dependent) rms orbital excursion length of the waves as well as on the spacing of the individual elements. The two regions of interest for this research are the inertia flow regime and the general flow regime. These regimes are governed by oscillatory flow and have relatively large attenuation parameters. The spacing of the elements has to be chosen such that the flow regimes fall in either the inertia or general flow regimes for the entire range of hydrodynamic conditions and water levels tested.
- *Measurable:*
  A limitation of laboratory experiments is that instrumentation can only measure at a limited number of points. While a natural reef canopy is characterized by irregular spacing, positioning, and shapes, relating a single measurement to a specific reef feature is near impossible. While this information is still valuable as it resembles a natural system more accurately, laboratory experiments allow for precise control of the wave conditions and the configuration of the artificial reef. Given the controlled environment and the limited measurement locations, arranging the roughness elements in a structured grid is essential. This structured approach allows us to relate the observed velocity field to both the specific design of the roughness elements as well as the location within the canopy.

Biodiversity requirements

- *Exposure:*
  The artificial reef should provide a habitat for various forms of marine live, including corals. Corals are highly dependent on temperature and light intensity, and like most marine organisms, need to remain constantly submerged to survive. The range of water levels investigated for the ARISE project are between 0.17 m to 0.67 m. Based on this requirement, the artificial reef should have a maximum height of 0.17 m to ensure it remains fully submerged at all times.
- *Marine species habitat:*
  An artificial reef enhances biodiversity if it creates a habitat for various marine species, enabling the development of a diverse ecosystem. A key species for a healthy reef ecosystem is coral. Corals need light for growth and a solid substrate for their polyps to attach (Chappell, 1980;

Spieler et al., 2001). The polyps also require nutrition, which is facilitated by adequate water flow through the artificial reef (Piniak, 2002). While sufficient flow is generally not a concern due to the typically high flow velocities over shallow reef flats, the reef must be designed to ensure adequate light for coral growth. This can be achieved by incorporating horizontal ledges where coral polyps can attach to.

Other important reef species include fish and algae (Obura et al., 2022). Algae are expected to thrive under similar conditions to corals, as coral reefs in poor health are often dominated by benthic algae (Birrell et al., 2008). Fish, on the other hand, require shelter. Therefore, the shape and spacing of the artificial reef should provide refuge for various fish sizes. This can be accomplished by integrating tunnels of different sizes to serve as shelters for various species of fish.

4.1.2. Element Design

The design of a single roughness element is based on a balance between the requirements described above, with engineering considerations taking a priority if a trade-off between biodiversity and functionality must be made. The design begins with outlining the specifications for a single element and then proceeds to the overall configuration of the artificial reef, including the grid layout and element spacing. Figure 4.1 shows the final design of an element, with its general dimensions detailed in Table 4.1.

The element has horizontal ledges and tunnels of varying shapes and sizes to support marine life. Its dimensions are relatively large, with a height of 0.25 meters and width and length of 0.40 meters. Although the height of 0.25 meters means that the top part of the element remains above the waterline, which could limit marine growth in that area, reducing the height further would significantly lower the effectiveness of the element in dissipating wave energy. Therefore, a height of 0.25 meters is chosen. Table 4.1 also provides the nominal diameter of the element D_n, which is 0.30 meters. This diameter is based on a cylinder with equivalent volume and height.

Figure 4.1: Final design of an individual roughness element measures 0.25 m in height and 0.40 m in width. The element features horizontal ledges and tunnels of varying shapes and sizes to support marine life.

Height [m]	Length [m]	Width [m]	Volume [m^3]	Weight [kg]	Diameter D [m]	Nominal diameter D_n [m]
0.25	0.40	0.40	0.0175	~30 kg	0.40	0.30

Table 4.1: Element dimensions. The nominal diameter is calculated by calculating the diameter for a cylinder with similar height and volume.

4.1.3. Configurations Artificial Reef

Several configurations of roughness elements are tested on their efficacy as coastal protection and their influence on wave transformation. According to Lowe (2007) the spacing of individual elements and therefore the density of the artificial reef has a large influence on the attenuation of waves. In total four different configurations with different densities are tested numerically, of which two are chosen to be employed in the laboratory experiments. An exact description of how these restorations are numerically modelled is given in Section 4.2. The numerical model requires as input the porosity of the artificial reef, which is defined as one minus the volume covered by the roughness elements over the entire restoration area. To determine a value for this porosity for the specific configurations, the positioning of the elements has to be defined.

The four different configurations are all employed in a symmetrical staggered grid. An advantage of a symmetrical grid is that it is homogeneous, which allows for the inter-comparison between not only distinct configurations, but also between different locations within the configuration. Both an unstaggered and staggered grid could have been employed. A staggered grid was chosen because it maximises the frontal area of the artificial reef with respect to the flow, which according to Pomeroy et al. (2023) increases its efficiency at dissipating waves. Also, Lowe (2005a;2005b;2007) employed a staggered grid in his experiments as it enhances canopy flow compared to unstaggered grids.

The difference between the four configurations is their spacing, both in the cross-flume (S_x) and along-flume (S_y) direction (Figure: 4.2). These configurations all have a relatively high density and cover a greater width compared to typical field restoration projects, such as Reef Balls^{TM}, which are often placed in rows consisting of only a few elements (Reef Beach, 2024). A higher density and large width however, are necessary to increase the ability of the reefs to dissipate wave energy.

Table 4.2 presents the density options D1 to D4, along with their respective number of elements, x-spacing, y-spacing, and porosity. Porosity is defined as the ratio of the volume occupied by the elements to the total volume of the restoration. This is calculated by multiplying the number of elements by the volume of a single element and then dividing by the total volume of the restoration.

Additionally, the table includes the ratio S_x/D_n, where S_x represents the x-spacing, and D_n the nominal diameter. The ratios investigated here are between 1 and 2, which is comparable to the ratios used by Lowe et al. (2007). Increasing the density further, resulting in ratios far below 1, is unwanted, as the spacing becomes so small that the orbital excursion length A_∞^{rms} with respect to the spacing becomes too large, resulting in the energy dissipation no longer being frequency dependent.

Configuration	Number of elements [-]	x-spacing S_x [m]	y-spacing S_y [m]	porosity ρ [-]	S/D_n [-]
D1	66	0.54	0.54	0.90	1.9
D2	91	0.42	0.42	0.87	1.5
D3	120	0.34	0.34	0.83	1.1
D4	153	0.27	0.27	0.78	0.9

Table 4.2: Characteristics of the four configurations tested in SWASH including their porosity. Of these four configurations, two will be used in the laboratory experiments.

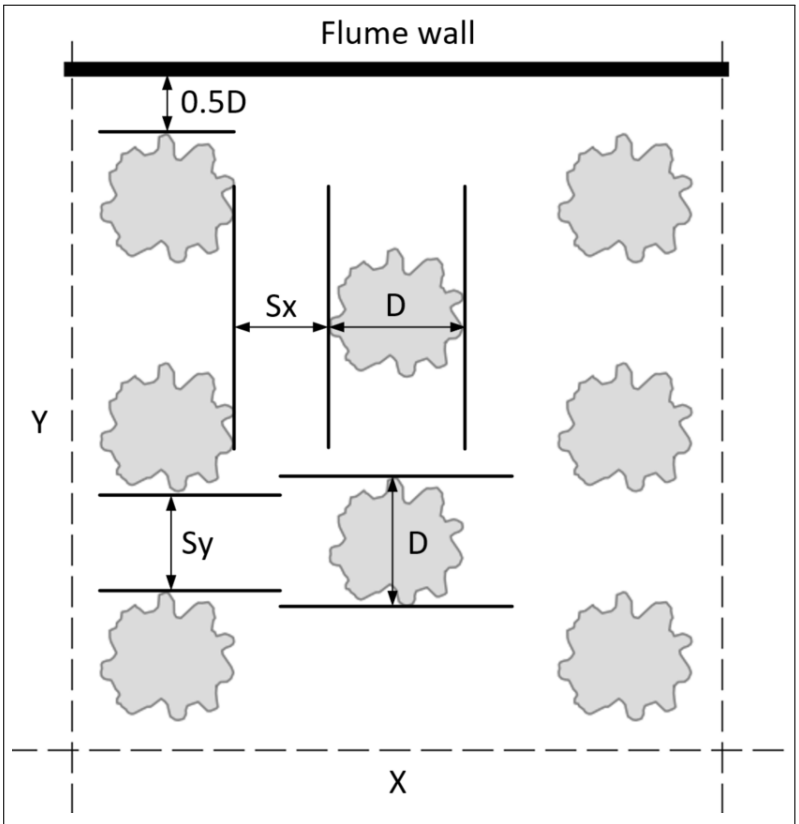

Figure 4.2: The distinct configurations are placed in a staggered grid with x - spacing (S_X) and y - spacing (S_y). The diameter D is identical in both x and y direction. The elements are located 0.5D from the walls of the flume.

Figure 4.3 illustrates the full restoration for configuration D2 involving 91 elements. The setup spans approximately 10 m, with the elements positioned at a distance of 0.5D from the wall.

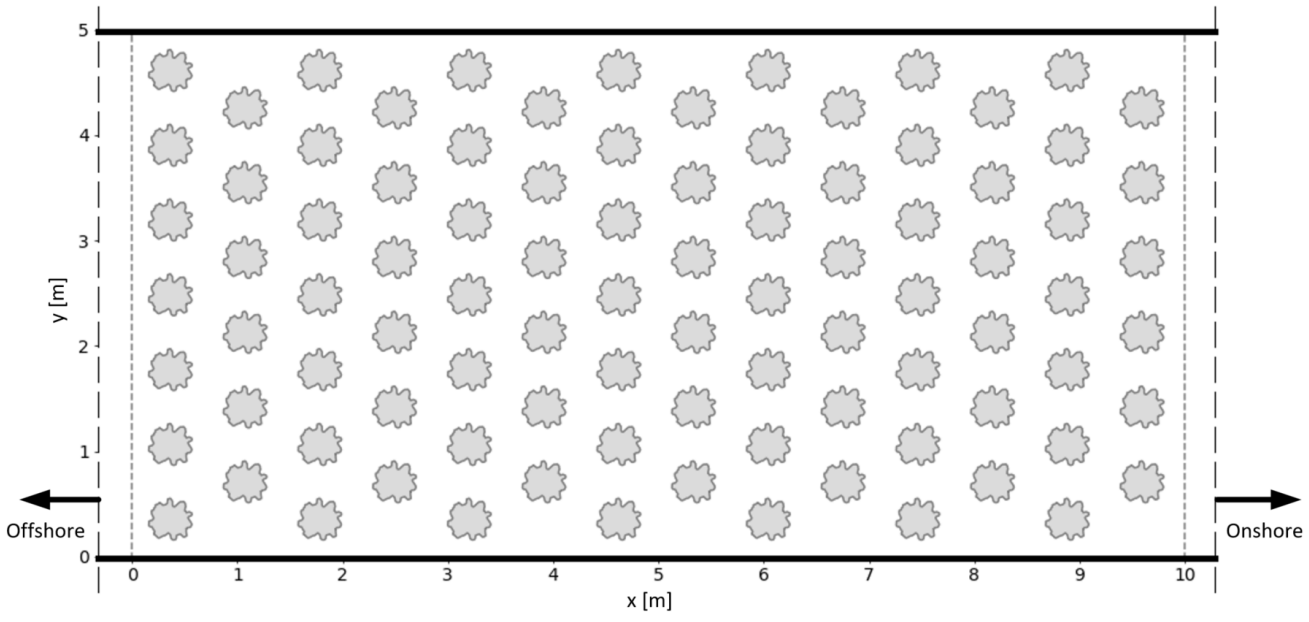

Figure 4.3: Top view of the reef restoration case D2 (91 elements).

4.2. Numerical Model

Numerical modelling is employed to investigate how for this laboratory setup, the effect of both the positioning on the reef flat as well as the density of the artificial reef itself affects the wave field. The numerical modelling tool SWASH is used, which has proven to be an efficient tool for modelling wave transformation over a fringing reef (Zijlema, 2012). SWASH is able to model submerged porous structures and has proven to be effective at estimating the wave transmission for permeable rubble mound submerged breakwaters (Rathnayaka, 2023). However, it has not been applied to artificial reefs, which in general have a much larger porosity. Therefore, the results need to be compared to the laboratory data to validate the applicability of SWASH to more porous structures, such as artificial reefs.

This chapter describes the modelling approach, including a general description of the numerical model SWASH as well as the numerical setup, including the numerical schematisation of the artificial reef. The chapter ends with the performed model runs. Three different locations are tested as well as four different densities for all the wave conditions described in Chapter 3.

4.2.1. SWASH

The modelling tool SWASH is selected, which is a non-hydrostatic wave-flow model capable of simulating wave propagation and transformation in the surfzone and swash zone. As a phase-resolving model, SWASH allows for the investigation of individual components in the wave spectrum, a necessity for this research. This distinguishes it from spectral wave models like SWAN, which lack the capability to model runup. SWASH implements a local mass and momentum equation and uses a Poisson Solver for the non-hydrostatic pressure. By modelling the energy dissipation of the wavebreaker-generated turbulence, the Prandtl mixing length hypothesis is applied. This allows for realistic breaking as well as propagation of breaking waves (Zijlema, 2011)

While Boussinesq type models, such as used by Carlot et al. (2023), are capable of modelling runup, they do not explicitly describe the vertical flow velocity field, making the modelling of interaction with roughness elements challenging. Also, despite the option of using a fully 3D CFD model, as demonstrated by Norris et al. (2023) and Pomeroy et al. (2023), the significant computational time required discouraged its use in this study.

SWASH allows for the modelling of artificial reefs as an impermeable bottom layer with increased elevation and roughness, as vegetation, or as a porous medium. However, like any numerical model, SWASH has its limitations. For instance, it may not perfectly capture 3D canopy flow, which is expected to be of significant importance in wave dynamics over a coral reef. Also, SWASH has not yet been validated to be able to properly model submerged artificial reefs. Therefore, its limitations need to be investigated and the results of the laboratory experiments can be used to validate the numerical model.

Governing Equations and Boundary Conditions

SWASH is a multi-layer non-hydrostatic model based on the Euler equations describing an incompressible fluid with a free surface η and a constant density p_0. The Euler equations for a 2D-vertical domain where the water column is defined from the free-surface $z = \eta$ to the bottom $z = -d$, are given by:

$$\frac{\partial u}{\partial x} + \frac{\partial w}{\partial z} = 0 \tag{4.1}$$

$$\frac{\partial u}{\partial t} + \frac{\partial uu}{\partial x} + \frac{\partial uw}{\partial z} + \frac{\partial P}{\partial x} = 0 \tag{4.2}$$

$$\frac{\partial w}{\partial t} + \frac{\partial uw}{\partial x} + \frac{\partial ww}{\partial z} + \frac{\partial P}{\partial z} = -g \tag{4.3}$$

where u and w are, respectively, the horizontal and vertical velocities, g is the gravitational acceleration and P is the total pressure normalised with the reference density. The total pressure is defined as:

$$P = p - gz = q + g(\eta - z) \tag{4.4}$$

where p and q are the dynamic and non-hydrostatic pressures, respectively. The two kinematic boundary conditions, one at the free surface and one at the impermeable bottom, are expressed as:

$$w_s = \frac{\partial \eta}{\partial t} + u\frac{\partial \eta}{\partial x} \quad \text{at } z = \eta \tag{4.5}$$

$$w_b = -u\frac{\partial d}{\partial x} \quad \text{at } z = -d \tag{4.6}$$

Integrating the continuity equation (Eq. 4.1) over the entire water column, $h = d + \eta$, and applying the kinematic boundary conditions, the free surface equation can be obtained:

$$\frac{\partial \eta}{\partial t} + \frac{\partial}{\partial x}\int_{-d}^{\eta} u\, dz = 0 \tag{4.7}$$

Equations 4.1 to 4.3 are the general governing equations which are numerically solved in SWASH. However, the equations look slightly different when multiple layers are applied, which is the case for this research. The layer-integrated continuity equation and momentum equations for layer $k(z_{k^-} \leq z \leq z_{k^+})$ are as follows:

$$\frac{\partial h_k u_k}{\partial x} - u_k^{(+)}\frac{\partial z_k^{(-)}}{\partial x} + u_k^{(-)}\frac{\partial z_k^{(+)}}{\partial x} + w_k^{(+)} - w_k^{(-)} = 0 \tag{4.8}$$

$$\frac{\partial h_k u_k}{\partial t} + \frac{\partial u_k h_k u_k}{\partial x} + u_k^{(+)} w_{r,k}^{(+)} - u_k^{(-)} w_{r,k}^{(-)} + h_k g\frac{\partial \eta}{\partial x} + \frac{\partial h_k q_k}{\partial x} - q_k^{(+)}\frac{\partial z_k^{(+)}}{\partial x} + q_k^{(-)}\frac{\partial z_k^{(-)}}{\partial x} = 0 \tag{4.9}$$

$$\frac{\partial h_k w_k}{\partial t} + \frac{\partial u_k h_k w_k}{\partial x} + w_k^{(+)} w_{r,k}^{(+)} - w_k^{(-)} w_{r,k}^{(-)} + q_k^{(+)} - q_k^{(-)} = 0 \tag{4.10}$$

where w_r is the relative vertical velocity at the layer interface, defined as the difference between the vertical velocity along the streamline and the vertical velocity along the interface:

$$w_{r,k}^{(+)} = w_k^{(+)} - \frac{\partial z_k^{(+)}}{\partial t} - u_k^{(+)}\frac{\partial z_k^{(+)}}{\partial x} \tag{4.11}$$

The $k - \epsilon$ turbulence model is incorporated within the SWASH model to compute the eddy viscosity, which modulates the turbulent diffusion of momentum. With this model, porosity can be accounted for by modifying the bottom friction, using the Van Gent (1995) formula, which adjusts the frictional forces based on the porosity of the medium. Additionally, the w-momentum equation is extended to incorporate frictional forces, and the model includes the effect of added mass, further improving the simulation of turbulent flow in a porous medium.

4.2.2. Numerical Setup

The numerical model is set up in accordance with the lab experiments in terms of bathymetry and wave conditions. The model is run in one-dimensional dynamic mode, and uses the $k - \epsilon$ model to represent turbulence, which means that it can more accurately describe turbulence and wave breaking, which is important in our case of shallow water depth.

Several parameters have to be defined for the numerical model, namely the computational domain, consisting of the bathymetry a length step size (Δx) and the number of vertical layers, of which the latter

two depend on the hydrodynamic conditions and the expected velocity gradients respectively. The time step Δt employed in the model depends on the CFL stability criteria and therefore the Courant number, which has to be defined.

In this section all parameters that have to be defined for the model are discussed, including the computational domain, the wave spectrum and boundary conditions, and a description of the numerical schematisation of the artificial reef.

Computational Domain and Time Step

The computational domain is structured as a regular grid, and follows the setup of the laboratory experiment (Figure 3.2), therefore it extends 180 meters in length. The island is modelled as a constantly sloping beach from 160 to 180 meters, reaching a height of 2 meters above the reef flat, which corresponds to the berm in the experimental setup. This berm is designed such that the runup, under the tested wave conditions, never overtops the crest of the island. Consequently, in the model, the runup also remains below 180 meters, making the beach effectively infinitely sloping. A Manning friction coefficient is chosen at 0.01 over the entire computational domain, corresponding to the value for a concrete floor (Chow, 1959).

For the vertical resolution, 10 layers are employed, following research by Smit and Zijlema (2013), who suggest that for strong vertical velocity gradients, expected with sharp changes in bathymetry or for artificial reefs, 10 to 20 vertical layers should be implemented. The lower bound is chosen to limit computational times.

Grid Cell Length Scale Δx

The grid cell length scale Δx is determined based on criteria from Zijlema (2011). Zijlema recommends, for non-linear waves, to define the length scale as one hundredth of the dominant wavelength. The dominant wavelength depends on the location within the domain as well as the offshore wave conditions. It is calculated based on linear wave theory using the following formula:

$$L = \frac{g \cdot T_p^2}{2\pi} \cdot \tanh\left(\frac{2\pi d}{L}\right)$$

Each condition will be tested using the same numerical setup, meaning that the most stringent condition, which results in the lowest dominant wavelength, dictates the choice of Δx. Consequently, the lowest peak period and the lowest water level in the domain result in the shortest dominant wavelength.

With a minimal offshore peak period T_p of 5.77 seconds and a minimal water depth d of 0.33 meters on the reef flat, the dominant wavelength L is approximately 10 meters. It is important to note that while 5.77 seconds is the forcing period of the spectrum, it does not match the period on the reef flat, where the period is expected to be larger due to the transfer of wave energy to lower frequencies. Nevertheless, using 5.77 seconds provides a lower bound for the dominant wavelength. With L approximately 10 meters and applying the criterion of Δx being 1/100 of the dominant wavelength, Δx is determined to be 0.1 m.

Time Step Δt

The time step Δt is based the CFL condition, which is a stability condition depending on the Courant number:

$$C_r = \frac{\Delta t(c+u)}{\Delta x} \leq 1$$

where the Courant number C_r is set to 0.4, as recommended by Zijlema (2011). To determine the time step Δt, both the wave celerity c and the velocity u must be quantified.

The offshore wave celerity c is expected to be largest due to the relatively deep water. Shallow water is assumed, maximising the wave celerity, and therefore the celerity is calculated using the formula $c = \sqrt{g * d}$, where g is the acceleration due to gravity (9.81 [m/s^2]) and d is the water depth. With the maximum water depth reaching 5.67 meters, the celerity c is approximately 8 m/s. Under the

assumption that the offshore velocity u is minimal, a time step Δt of 0.005 seconds is selected to ensure numerical stability.

Wave Spectrum and Boundary Conditions

The chosen wave spectrum is the JONSWAP spectrum with a peak enhancement parameter γ of 3.3, which is both the default value for this spectrum and the value used to generate the wave spectrum for the laboratory experiments. The JONSWAP spectrum was originally developed from data in the North Sea, and therefore the spectrum is relatively broad compared to the more swell dominated wave spectra as found in the Indian and Pacific Ocean. Despite this limitation, the JONSWAP spectrum has been effectively used for modelling wave transformation and propagation for a wave field in the Maldives (Amores et al., 2021).

In this setup, the JONSWAP spectrum is imposed as a weakly reflective boundary on the offshore side of the computational domain, specifically at the location of the wave generator. The spectrum has a 15-minute cycle time and is defined by the significant wave heights and peak periods that are to be tested. Additionally, second-order bound waves are introduced at the offshore boundary. These bound waves include both super-harmonics as well as weakly non-linear IG waves. The super-harmonics help to mitigate the generation of spurious modes, which is essential for accurately modelling highly non-linear waves. The IG waves need to be added at the offshore boundary since this location is located in intermediate water. Therefore, a natural wave spectrum includes these weakly non-linear IG waves, which are not present in the JONSWAP spectrum by default and as a result, need to be added.

The total duration of each model run is set to 55 minutes, of which the initial 10 minutes are removed to account for spin-up time. This leaves 45 minutes for the actual analysis. Considering the longest peak period of 9.24 seconds, each model run covers at least 200 waves of the dominant wavelength during the analysis period. This provides a sufficient number of waves to ensure accurate analysis of the wave statistics.

Breaker parameter

Wave breaking is a critical factor in coastal dynamics, and accurately modelling this process in SWASH is essential. SWASH often underestimates wave breaking when the vertical resolution is coarse. Therefore, to improve the accuracy, SWASH includes a BREAKING command which can be used to more accurately describe the breaking process.

Typically, with a high vertical resolution, additional parameters for wave breaking are not necessary (Smit et al., 2013). Research by Zijlema (2012) and Liu et al. (2021) has shown that for simulations with a low vertical resolution, specifically a two-layer setup, the unique characteristics of fringing reefs require adjusting the breaker parameter. Namely, the default value of 0.6, representing the wave steepness at which breaking occurs, needs to be increased to 1.6 to account for the steeper slopes associated with these environments. A higher breaker parameter indicates a steeper breaking criterion.

In this study, the breaker parameter is set to the default value of 0.6 because a high vertical resolution is used, and therefore, theoretically, there is no need to adjust the parameter (Smit et al., 2013). Nevertheless, while SWASH validates the use of this parameter for general cases with a high vertical resolution, there is limited research on its effectiveness for the steep fore reefs of fringing reef systems.

4.2.3. Numerical Schematisation Artificial Reef

At the start of this chapter, it was mentioned that the artificial reef is represented as a porous layer in SWASH. While this approach has been effective for estimating wave transmission through permeable rubble mound submerged breakwaters (Rathnayaka et al., 2023), it has not been applied, in SWASH, to artificial reefs, which typically have a much higher porosity. Therefore, the results need to be compared to laboratory data to validate SWASH's applicability to more porous structures, such as artificial reefs.

The porous medium requires three parameters: porosity, the height of the porous layer, and the height of an individual element. For this study, the porous medium extends over a 10 m area with a height of 0.25 m and an individual element height of 0.25 m. In SWASH, the mean flow through a porous medium is described by the volume-averaged Reynolds-averaged Navier-Stokes (VARANS) equations.

Laminar and turbulent frictional forces in the porous medium are modelled using the empirical formulas of Van Gent (1995), which is a resistance-type porosity model developed for rubble mound breakwaters, typically with a porosity around 0.5. The Van Gent equations calculate the hydraulic gradient I as a function of the flow velocity u and three dimensional coefficients a, b, and c (Equation 4.12).

$$I = a \cdot u + b \cdot u\,|u| + c\frac{du}{dt} \tag{4.12}$$

With the dimensional coefficients:

$$a = \alpha\frac{(1-n)^2}{n^3}\frac{\nu}{g * D_{n50}^2} \tag{4.13}$$

$$b = \beta(1 + \frac{7.5}{KC})\frac{1-n}{n^3}\frac{1}{g * D_{n50}} \tag{4.14}$$

$$c = \gamma_p\frac{1-n}{n} \tag{4.15}$$

In which n the porosity, ν the kinematic viscosity of water and D_{n50} the nominal diameter equal to 0.25 m and KC the Keulegan-Carpenter number. Coefficient c is an added-mass coefficient with γ_p a closure coefficient, which is set to be 0.34 as the default value. The coefficients α and β are coefficients associated to the laminar and turbulent friction loss, respectively. These coefficients dependent on several parameters, such as the Reynolds number, the shape of the elements, the permeability and, importantly, the flow characteristics. The coefficients require calibration with laboratory data, since a large range in values exist for these parameters in literature.

Various studies have derived values for these parameters based on numerical simulations and experimental tests on submerged porous breakwaters with a porosity of around 0.5. For example, Pilechi et al. (2018), Hsu et al. (2002), and Losada et al. (2008) found values for α of 200 and for β of 1.1. Other research on submerged breakwaters with a similar porosity of around 0.5 calibrated the parameters further and found values ranging from 200 to 2000 for α and values for β between 0.8 and 4 (Lara et al., 2006; Garcia et al., 2004; Burcharth, 1995; Srineash et al., 2020; Mellink et al., 2014).

Although most of these studies used models based on the VARANS equations, only Mellink et al. (2014) employed SWASH for their investigation and found values for α and β for which the numerical output corresponded well with the laboratory results. Despite examining similar breakwater structures, either emerged or submerged and of similar dimensions, these studies found significant differences for the values of α and β. The structure used in this thesis differs significantly from these breakwaters, particularly in the size and porosity of the individual porous elements, although the overall dimensions (height, length, and submergence) are comparable.

The Van Gent approach to modelling flow in a porous structure, although not with SWASH, has also been applied to fringing reefs. Research by Qu et al. (2024), Liu et al. (2020) and Yao et al., (2022) performed a combination of numerical modelling and laboratory tests to examine the wave transformation over a fringing reef covered by a roughness layer of several centimetres high consisting of vertically placed cylinders. Although the porosity and morphology of the reef is similar, their research consisted of significantly smaller elements covering the entire reef flat as well as the reef crest. They found values for α of 200 to 500 and β of 1.1 to 2 for which the numerical data aligned reasonably well with the experimental data.

For this study, values of $\alpha = 200$ and $\beta = 1.1$ were used, which are the default values mainly based on the experiments of Van Gent (1995). Ideally, these parameters should be calibrated for this specific case; however, this falls outside the scope of this thesis. Instead, we determine whether the experimental conditions of this thesis fall within the range of tests performed by Van Gent. If not, the applicability of the default values for these dimensional coefficients can be assessed in a broader context when compared to laboratory data. This comparison is made after the following section, in which the numerical simulations are described.

Additionally, while the flow velocity in the Van Gent equations is influenced by the frequency of the wave components, it does not directly correlate with the frequency-dependent dissipation described by Lowe. Therefore, it is crucial to examine the differences in spectral dissipation per wave component between the numerical model using the Van Gent equations and the laboratory experiments, which are expected to align more closely with Lowe's theory.

4.3. Numerical Simulations

Multiple locations for the artificial reef on the reef flat and various densities are tested to investigate their effects on the wave field and specific wave components, as well as to optimize the configurations for the subsequent laboratory tests. In the lab experiment, two configurations with different densities are assessed at a single location on the reef flat.

According to Roelvink et al. (2021), the location of a reef restoration on the reef flat significantly influences energy dissipation, with restorations situated in the middle and closer to the shoreline showing greater efficiency in energy dissipation compared to those near the crest. Additionally, energy transfer from high-frequency to low-frequency components over the reef flat results in varying wave spectra at different cross-shore locations. This variation suggests that energy dissipation will differ depending on the reef's location, and therefore three different locations for the artificial reef are tested.

Additionally, Lowe (2007) indicates that different densities and spacings of roughness elements affect energy dissipation rates. Given that canopy flow dynamics are expected to vary with density, four distinct densities are tested in the SWASH simulations, of which two are chosen for the laboratory tests. However, SWASH's approach in determining the energy dissipation of a porous medium is not expected to have a frequency dependent dissipation based on the density. Therefore, the SWASH simulations are used to estimate the expected magnitude of dissipation for each density and to identify the likely flow regimes. Based on this, two configurations with different densities are chosen for the laboratory test, where frequency dependence of the dissipation is then analysed using the laboratory results.

For each configuration the same water levels and wave conditions are repeated. A total of five wave conditions and two water levels are tested, which gives a total of 10 numerical simulations per configuration (Table 4.3).

Figure B.1 and B.2 in Appendix B present the SWASH input files for a simulation of wave condition C3 with WL33, corresponding to the base case and a case with a restoration, respectively. Each simulation took approximately 3 hours to complete on a desktop computer with the specifications provided in Table B.1.

Simulation	Water level		Wave condition		
	Name	Height [m]	Name	Hs [m]	Tp [s]
1	WL33	0.33	C1	0.5	5.77
2	WL33	0.33	C3	0.5	9.24
3	WL33	0.33	C7	1.0	5.77
4	WL33	0.33	C9	1.0	7.51
5	WL33	0.33	C11	1.3	5.77
6	WL67	0.67	C1	0.5	5.77
7	WL67	0.67	C3	0.5	9.24
8	WL67	0.67	C7	1.0	5.77
9	WL67	0.67	C9	1.0	7.51
10	WL67	0.67	C11	1.3	5.77

Table 4.3: For each configuration of the artificial reef, 10 simulations are performed with two different water levels and five different wave conditions.

A total of four different densities of artificial reefs are investigated, of which two will be employed in the laboratory experiment. To optimise computational and analysis time, only a single density will be examined for each of the three different locations. Initially, the optimal location among the three is selected based on these investigations. For the chosen location, all four densities are then analysed.

In Table 4.5, the four densities (D1 to D4) are presented along with their respective porosities. Density D2, highlighted in yellow in the table, is the specific density that will be tested across the three locations.

Density	Number of elements [-]	x-spacing S_x [m]	y-spacing S_y [m]	porosity ρ [-]
D1	66	0.53	0.53	0.903
D2	91	0.41	0.41	0.867
D3	120	0.33	0.33	0.827
D4	153	0.26	0.26	0.780

Table 4.4: The four densities to be numerically tested in SWASH. The table contains the spacing and number of elements for these configurations to be used in the lab as well as the corresponding porosity. In yellow the density, Density D2, is highlighted, which is the density used for analysing the optimal location.

Location

The three locations for the artificial reefs are chosen based on their positioning along the reef flat. Each artificial reef measures 10 meters in length and 0.25 meters in height, and they are placed at distinct zones: the outer reef flat, middle reef flat, and inner reef flat. Figures 4.4 and 4.5 illustrate the positioning of these configurations.

- **Outer Restoration (R1)**: Positioned between 120 and 130 m from the offshore boundary, this restoration is approximately 5 m from the reef crest.
- **Middle Restoration (R2)**: Located at the center on the flat, between 132.5 and 142.5 m.
- **Inner Restoration (R3)**: Located between 145 and 155 meters, this reef extends to 5 m from the beach toe.

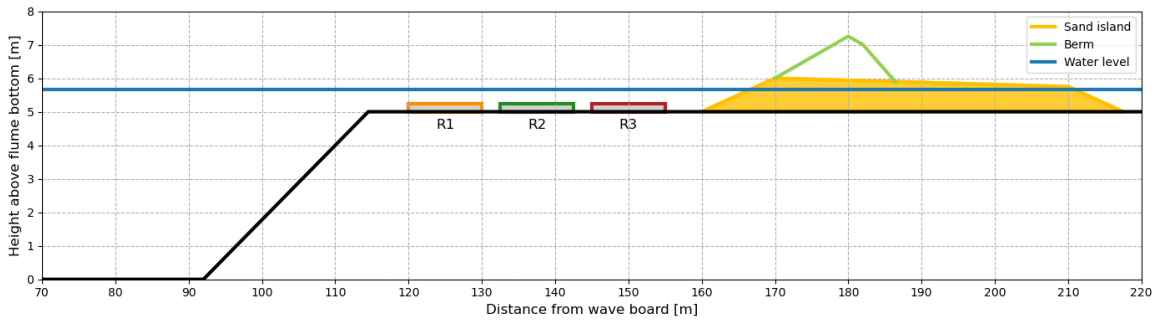

Figure 4.4: Laboratory setup, including the three locations of the artificial reefs to be tested. A berm can be seen on the island, which is also employed in the laboratory experiments

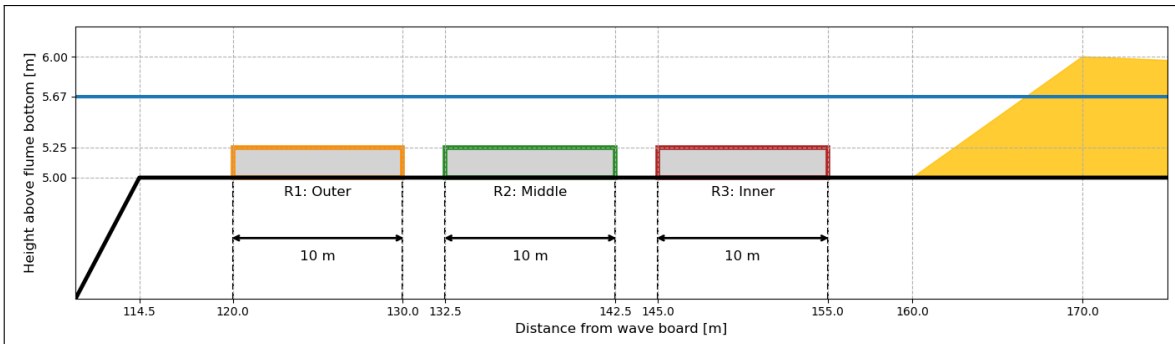

Figure 4.5: Laboratory setup, zoomed in on the restorations on the reef flat. All three restorations are 10 m in length and 0.25 m in height. The outer restoration extends from 120 to 130 m, the middle from 132.5 and 142.5 m, and the inner from 145 to 155 m.

4.4. Initial Assessment of Modelling Approach

An initial assessment is performed to investigate potential limitations in the modelling approach, regarding the numerical setup, simulations, and artificial reef design. These limitations may stem from factors such as scaling or SWASH's application of the Van Gent method in modelling porous media, potentially leading to inaccuracies in the results. Additionally, an investigation into whether the tested conditions fall within the general or inertia-dominated canopy flow regimes is performed. It is a necessity that these flow regimes are covered, since frequency-dependent energy dissipation is expected for these domains.

Scaling

For the artificial reef structures, a geometric scaling factor of 3 is applied, consistent with the scaling used for the laboratory experiments. Wave conditions are scaled using Froude scaling laws, which are more appropriate for larger-scale wave experiments than Reynolds scaling, which focuses on turbulence. However, for complex shapes like this, turbulence around the structure is significant. To ensure that both the real-life prototype and the scaled model are in the same turbulence regime, the Reynolds number for flow around the structure is calculated for both cases. The Reynolds number is given by:

$$R_m = \frac{u_m \cdot l_m}{\nu} \tag{4.16}$$

$$R_p = \frac{u_m/\sqrt{n_L} \cdot (l_m/n_L)}{\nu} \tag{4.17}$$

where R_m is the Reynolds number of the model, u_m is the model velocity (rms) in m/s, l_m is the smallest length scale of the printed reef elements in meters, ν is the viscosity of water, and R_p is the Reynolds number of the prototype (real-life). The values are scaled according to Froude scaling laws with the length scaling factor n_L, equal to 3.

The smallest length scale of a single element is measured to be around 0.015 meters or 1.5 cm, which is the smallest horizontal ledge size that could be printed. For the velocity, the average velocity over the length of the restorations was chosen. Of all the simulations, the minimum value of this velocity is around 0.5 m/s. Therefore, the prototype R_p and model R_m Reynolds numbers are as follows:

$$R_p = 40,000$$
$$R_m = 7,500$$

Flow is considered fully turbulent if the Reynolds number is above 4000. Given that both calculated Reynolds numbers exceed this threshold, both the prototype and the model are within the turbulence regime. Therefore, applying Froude scaling laws is justified, and it does not introduce discrepancies in the results related to turbulence.

Numerical Schematisation Artificial Reef

In SWASH, the attenuation of a porous structure is approached with the Van Gent equations. Van Gent derived the values of the dimensional parameters from tests on rubble mount breakwaters with a porosity of around 0.5. He determined the region in which his tests are performed as a function of both the Reynolds number R_e and the Keulegan Carpenter number KC (Equation 4.18).

$$R_n = \frac{u * D}{\nu}, \qquad KC = \frac{u * T}{D} \tag{4.18}$$

Where:

u	[m/s]	=	Flow velocity amplitude
D	[m]	=	Element diameter
ν	[m^2/s]	=	Kinematic viscosity
T	[s]	=	Characteristic wave period

The amplitude of the flow velocity u as well as the characteristic wave period are acquired from SWASH by averaging these values over the length of the restorations. The element diameter is chosen as the nominal diameter of 0.3 m, and a default kinematic viscosity of $10^{-6} m^2/s$ is used. The characteristic wave period is represented by the spectral period T_{m01}, a commonly used spectral characteristic.

Figure 4.6 illustrates the regions of the concerning test associated with the Van Gent experiments alongside those for the CREST experiments. It is clear that the CREST experiments fall outside of the range for the Van Gent experiments. The CREST experiments fall within the 'large rock' category, which aligns with the size of the individual elements used. Consequently, the default dimensional parameters α and β might not be able to accurately predict the wave attenuation of the artificial reef.

Moreover, wave attenuation is influenced by the arrangement of the artificial reef elements, which for these experiments are placed in a structured and staggered grid. This configuration cannot be directly represented in SWASH. However, it is known that grid structure can influence wave transformation processes (Gijón et al., 2021).

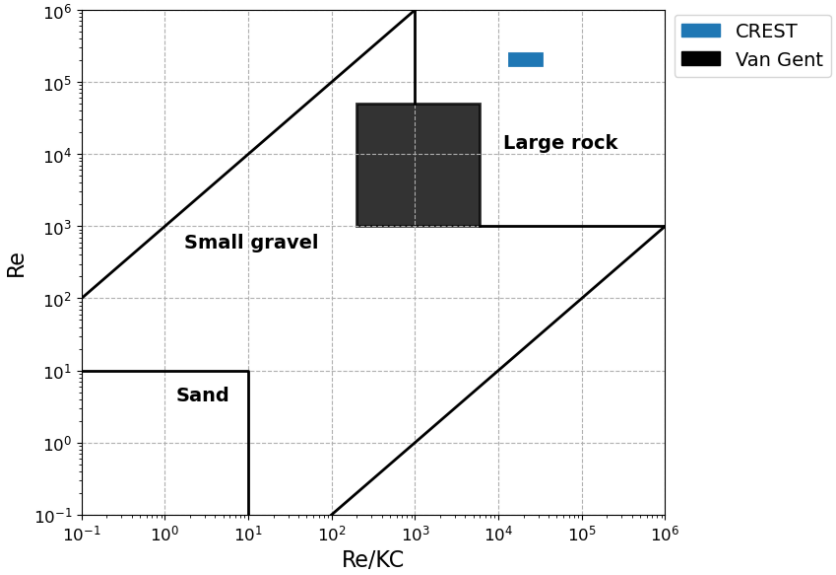

Figure 4.6: The Van Gent experiments are performed in the region denoted by the black square, while the CREST experiments cover the range of the blue square (altered from Van Gent, 1995). Re denotes the Reynolds number and KC the Keulegan-Carpenter number.

Canopy flow regimes

The densities tested in the experiments are chosen to resemble the ratios as used by Lowe et al. (2007) in their research. The selection of the two densities used in the experiments is primarily based on the magnitude of total energy dissipation and the added effect increasing the density has on this dissipation. However, it is important to verify the flow regimes these configurations represent, such that frequency dependence can be investigated for the laboratory data. Frequency dependence can be expected when the flow regimes fall in either the general or inertia dominated domain.

To classify the flow regimes for the tested conditions and various densities, the orbital excursion length is calculated using $A_{\infty}^{rms} = U_{\infty,w}^{rms}/\omega$. Since the free-stream velocity is required, the SWASH simulations without a restoration (S0) are used, as the depth-averaged velocity from these runs represents the free-stream velocity. The wave angular frequency is determined based on the spectral period T_{m01}. The free-stream velocity is calculated as $U_{\infty,w}^{rms} = 2 * \sqrt{2} * std(u')$, where u' represents the deviation of the velocity from the mean u_{mean}.

For each location, density and wave condition the ratio A_{∞}^{rms}/S is calculated to determine their flow regime. Values of A_{∞}^{rms}/S higher than 1 indicate the general flow regime, while values below 1 indicate the inertia flow regime.

Density Configuration	Outer	Middle	Inner
D1	0.7 - 1.8	0.4 - 1.7	0.4 - 1.3
D2	0.8 - 2.1	0.5 - 1.9	0.5 - 1.6
D3	1.0 - 2.4	0.6 - 2.2	0.6 - 1.8
D4	1.1 - 2.7	0.7 - 2.5	0.6 - 2.0

Table 4.5: Range of A_{∞}^{rms}/S for each configuration and restoration location.

The range of A_{∞}^{rms}/S is largest for configuration D4. For all configurations, the range of A_{∞}^{rms}/S is around 1, indicating to be in both the inertia flow regime as well as in the general flow regime, and therefore, frequency dependent energy dissipation can be expected for the laboratory results.

4.5. Conclusion: Artificial Reef Design

A discussion of the modelling approach is already given in the previous section. This chapter concludes the design part of the artificial reef, which is covered by research question 1, which is answered in this section.

How can an artificial reef restoration be designed and schematized for the use in a large-scale laboratory experiment?

This research question focuses on the design of the artificial reef, consisting of the entire reef as well as the individual elements making up the reef. Additionally, this artificial reef has been schematized numerically in the SWASH model. Therefore, the sub-questions are oriented around these two parts and are answered individually.

What are the key parameters characterizing the artificial reef that need to be preserved in the lab?

The design of the artificial reef is governed by the specific requirements for this laboratory experiments. For the individual elements, key parameters are the height, frontal area and features that create habitat for coral species and other marine life. The first two parameters have a large influence on the dissipation of wave energy, with higher elements with a larger frontal area expected to dissipate more energy. The last parameter can be achieved by adding horizontal ledges and shelter for fish. These features increase the complexity in shape of the elements and result in the elements more closely resembling a natural reef system as well as increasing its ecological value.

The key parameter describing the configuration of the individual elements forming the artificial reef is the element spacing in combination with a structured staggered grid. With the hydraulic conditions and the element spacing, an indication of the flow regime can be given. Having these regimes to be in either the inertia or general flow domain ensures potential frequency dependent energy dissipation.

How can the reef restoration be represented in the numerical model SWASH and what are its limitations?

The reef restoration is represented in SWASH by means of a porous layer, with as input the height of the element and the corresponding porosity based on the density of the reef. While SWASH has shown to be effective at simulation wave transmission over a fringing reef, it has not been tested for artificial reefs with these porosities. It has been established that the conditions for which the dimensional coefficients used by SWASH are calibrated, are different from the conditions used in these experiments. Therefore, an investigation is required into how accurately SWASH can predict the wave dissipation through an artificial reef while using these uncalibrated coefficients.

5

Data Analysis Techniques

Both the data from SWASH as well as from the laboratory experiments need to be processed and analysed. Here the data analysis techniques used for this are discussed. The data analysis is similar for both sets of data, however the laboratory data requires additional data processing.

Laboratory data from the pressure (DRO) and velocity (EMS) sensors are processed for analysis. Although both type of sensors have been pre-processed by Deltares, the pressure sensor data requires additional processing to convert the pressure (kN/m^2) to sea surface elevation (m). The steps for this conversion can be can be found in Section C.1 of Appendix C. Additionally, while the positioning of the vectrino sensors is discussed, the analysis of their data, and therefore the processing, falls outside of the scope of this thesis. The analysis of both the numerical results and laboratory data is based on the characteristics of the wave spectra.

5.1. Spectral Characteristics

To infer information from the wave spectrum an analysis needs to be performed on the spectral characteristics. Therefore, the variance density spectrum is computed from the surface elevation time-series. From the density spectrum several spectral characteristics can be computed.

For both datasets, the initial 10 minutes are excluded to account for spin-up time and the first 5 minutes of the experimental runs during which water is pumped into the flume to compensate for the decrease in water level caused by the build-up of wave-induced setup on the reef. This period is sufficient to remove any inaccuracies resulting from the initial conditions and to allow the wave field to fully develop. Afterwards, the variance density spectrum is calculated by means of the Welch method. The Welch method is a technique for estimating the power spectral density (PSD) of a signal using the Fast Fourier Transform (FFT). While the computational time is generally larger, The Welch method reduces the variance by averaging modified power spectra from overlapping segments of data. The computational steps for performing the Welch FFT are described in Section C.2 of Appendix C.

From the variance density spectrum various wave parameters can be computed, which are useful for describing wave characteristics. The parameters that can be extracted are the spectral moments m_n:

$$m_n = \int_0^\infty f^n E(f) df, \qquad n = ..., -1, 0, 1, ... \tag{5.1}$$

where m_n is the n^{th} moment of the variance density spectrum and E(f) the variance density spectrum itself. The range of the frequency domain of the variance density spectrum is based on the Nyquist frequency and equal to half of the sampling frequency, which means that, while the frequency resolution is equal for both the numerical dataset and the laboratory dataset. The frequency domain extends to 5 hz and 60 hz respectively for these datasets. For both datasets the frequency limit for integration to calculate the spectral moments is set to the highest frequency of the sea/swell wave band.

In Section 2.3 two frequency bands were specified: The sea/swell wave band, and the infragravity waves. These frequency bands were defined with their respective frequency range, however the experiments are scaled with a geometric scaling factor of 3, therefore these frequency ranges need to be scaled to represent the correct frequencies as used in the experiments. Due to Froude scaling laws, time scales are scaled with a factor of $\sqrt{3}$ and since frequencies have the unit 1/s, the frequencies are scaled, by multiplying the values by a factor $\sqrt{3}$ (Table 5.1).

Frequency band		f_p [Hz]	f_m [Hz]
H_{SS}	Sea/Swell	0.03 - 1	0.052 - 1.73
H_{IG}	Infragravity	<0.03	<0.052

Table 5.1: Wave classification by frequency for prototype case and model

The upper limit for integration used to calculate the spectral moments is set at 1.73 Hz for both the laboratory data and the numerical simulations. This value corresponds to approximately 10 times f_p,where f_p represents the largest offshore peak frequency of the tested wave conditions. Although waves with larger frequencies are present, they are both irrelevant to this study and contribute negligible energy compared to waves with frequencies below this threshold.

With the zero-order moment m_0, the significant wave height H_{m0} can be calculated according to Equation 5.2.

$$H_{m0} = 4\sqrt{m_0} \tag{5.2}$$

With the spectral density, several spectral wave periods can be computed. A well known period is the peak period T_p, which is the period corresponding to the frequency with the highest energy density. While the peak period is useful for uni-modal wave spectra, such as the offshore spectra, it fails to capture the complexity of a multi-modal spectrum such as a wave spectra found on a reef flat, where the energy shifts from higher frequency components to lower frequencies as the waves propagate over the flat. Therefore, two other wave periods are used for the spectral analysis, namely the mean wave period $T_{m0,1}$, which is the period corresponding to the frequency with the mean energy density, and the mean energy period $T_{m-1,0}$, which is a different averaging of wave energy, more focused on the lower frequency bands (Equation 5.3). The latter period is especially useful for stability calculations on the artificial reef structures. The spectral periods describe the entire density spectrum and are therefore more appropriate for complex multi-modal wave spectra as can be found on a reef flat, compared to the peak period T_p.

$$T_{m0,1} = \frac{m_0}{m_1} \qquad T_{m-1,0} = \frac{m_{-1}}{m_0} \tag{5.3}$$

5.2. Guza Split: Co-Located Decomposition

Since reflection is expected to be significant on both the fore reef and the beach as well as to some extent on the artificial reefs, the incoming and outgoing wave fields need to be separated. A common approach for this separation is the Guza split method developed by Guza et al. (1985). This decomposition method uses the co-located water level and velocity time series. Several variations of the Guza method exist with some using the depth averaged velocity, while others use a point measurement of the velocity. Due to time restrictions, splitting the wave signal is only performed for the SWASH output, which uses depth averaged velocity. The Guza split method provides a surface elevation time-series that is separated into an incoming and an outgoing component.

Guza derived a method to split incoming η^+ and outgoing η^- components by writing it as a function of the depth averaged velocity U(x,y,z) and total water level η(x,t), by assuming that the total water level is a superposition of the incoming component η^+ and outgoing component η^- (Equation 5.4).

$$\eta = \eta^+ + \eta^- \tag{5.4}$$

The discharge can be decomposed in the same manner, with Q = U * h, the instantaneous velocity times the instantaneous water depth. The discharge associated with the incoming and reflected components can be expressed as:

$$Q = Q^+ - Q^-; \qquad Q^+ = c^+\eta^+, \qquad Q^- = c^-\eta^- \tag{5.5}$$

These equations can be combined and rewritten in terms of the incoming and outgoing water surface elevation η^+ and η^- as a function of the wave celerity, instantaneous velocity and instantaneous water depth:

$$\eta^+ = \frac{Uh + c^-\eta}{c^+ + c}, \quad \text{and} \quad \eta^- = \frac{Uh - c^+\eta}{c^+ + c} \tag{5.6}$$

where the wave celerity c^+ and c^- are assumed equal. For shallow water simulations determining these celerities is straightforward as the celerity is a function of depth only: $c = \sqrt{g * h}$. However, the shallow water assumption can not be made in this case, therefore linear wave theory has to be used, with $c = \omega/k$. This approach was developed by Dekkers (2018). The wave number k is calculated with linear wave theory, specifically the dispersion relation:

$$\omega^2 = g * k * tanh(kh) \tag{5.7}$$

Using the dispersion relation to determine the wave velocities and therefore the incoming and outgoing water level components, requires the computation to be made in Fourier space. However, the discharge Q depends on the instantaneous, and therefore time-dependent, water level and velocity. Performing the computation in Fourier space results in ignoring energy at twice the frequency of interest. While the energy at those frequencies is not expected to be significant, neglecting these introduces inaccuracies in the decomposed surface elevation signal. Expected is that on the reef flat, shallow water assumption holds, to investigate the extent of the inaccuracy, the wave signal is decomposed by assuming shallow water as well, which is compared to the decomposition performed in Fourier space.

5.3. Parameter Quantification

Calculating the variance density spectrum as well as decomposing the incoming and outgoing surface-elevation signal allows for the investigation of the wave transmission over the reef flat as well as the effect the artificial reefs have on this energy spectrum. The analysis of the data is split into two parts, one part consists of investigating the numerical data to determine the optimal position and densities for the artificial reef to be used in the laboratory experiments. The other part is on comparing the laboratory data to the SWASH output.

5.3.1. Numerical Data

The analysis of the numerical data is for both optimising the configurations in the lab as well as investigating the effect of the location of the restoration on specific wave components. The optimisation of the lab experiments is based on the effectiveness of the artificial reefs in mitigating wave energy. Therefore, the parameter which is investigated is the reduction of total wave energy reaching the shoreline. For the wave energy the spectral wave height H_{m0} is used, while it is not equal to the wave energy, it is calculated directly from the energy density spectrum and therefore proportional. The reduction R is quantified as a percentage in reduction of the incoming wave height compared to the base case, i.e. the case without an artificial reef, which can be calculated for any location (loc) in the domain (Equation 5.8).

$$R_{perc,loc} = \frac{H_{loc,inc,base} - H_{loc,inc,res}}{H_{loc,inc,base}} * 100\% \tag{5.8}$$

The parameter $R_{perc,loc}$ describes a reduction with respect to the base case at a certain location (loc) in the domain and therefore does not state if energy has been dissipated. The term ”reduction” is used to describe the effectiveness of the artificial reef, which gives a magnitude of change with respect to the base case.

Wave Component Investigation

After defining the optimal location for the artificial reef, a more in-depth analysis is performed for specific wave components and the influence of the location of the artificial reef on these individual components. The reduction coefficient is again investigated for the distinct frequency bands as well as the transformation of the spectral wave height H_{m0} over the reef flat. These spectral parameters for the individual bands can be acquired by limiting the integration for calculating the spectral moments (Equation 5.1) to the specific frequency bands.

Density investigation

After defining the optimal location, which is the location which has the highest reduction in incoming wave energy at the beach toe, the density is investigated. As mentioned earlier, the approach of SWASH in determining energy dissipation in a porous medium does not align with the theory of Lowe et al. (2007) on frequency-dependent dissipation, and therefore, it is not expected to accurately capture this frequency dependence. Consequently, the SWASH simulations on density are used to examine the magnitude of wave height reduction for a certain density. An investigation is performed into how effective increasing the number of elements is in increasing the wave height reduction.

Additionally, the expected flow regimes, which are based on the ratio of A_{∞}^{rms} over the spacing S, are calculated. A_{∞}^{rms} is calculated with the rms free-stream velocity, defined here as the mean depth-averaged velocity measured directly in front and behind the artificial reef, and the wave angular frequency ω for which the mean spectral period T_{m01} is used. For all wave conditions and water levels tested the range of the ratio A_{∞}^{rms} / S is determined and with it the flow regimes. Two Configurations are chosen that have a sufficiently large difference in energy reduction as well as fall into the inertia or general flow regime for all conditions tested.

5.3.2. Data Comparison

After optimising the laboratory experiments and completing the test runs, the results are ready for comparison with the SWASH model output. However, the conditions of the laboratory experiments differ slightly from those in the numerical simulations. To account for these differences, calibration is required to ensure the conditions match precisely. For example, the water level is manually adjusted at the beginning of each laboratory test run, so actual water levels may vary slightly from those in the initial simulations. Additionally, the exact positioning of the artificial reef may differ from the simulated setup. As a result, the numerical simulations need to be rerun using the precise conditions observed in the laboratory experiments.

Correcting Hydrodynamic Conditions

During the first five minutes of the experimental runs, water is pumped into the flume to compensate for the decrease in water level caused by the build-up of wave-induced setup on the reef. Since pumping occurs while waves are already present, it is not possible to perfectly match the desired offshore water levels of 0.33 m or 0.67 m on the flat. To correct for this, the water level is extracted from the most offshore pressure sensor located at x = 83 m from the wave generator. The mean water level at this sensor is calculated over the run duration, excluding the first 10 minutes allocated for both the pumping and spin-up time.

Additionally, the exact location and extent of the artificial reefs has to be measured and included correctly in the numerical model. Also, because of limitation of the wave generator, the wave height conditions might not be exactly as those defined initially. The exact offshore peak period and significant wave height can be extracted from the incoming wave field of the most offshore wave gauge, which is located at 40 m from the wave generator. However, due to time constraints, the time-series of the laboratory data has not been split into an incoming and outgoing component. Therefore, the exact offshore wave conditions cannot be extracted and used for the numerical simulations.

Spectral Parameter Investigation

After replicating the exact laboratory conditions, the results can be compared. Again, an investigation into the spectral parameters is performed. However, instead of R_{perc} a reduction coefficient is used, which expresses the change in wave height H_{m0} over the domain as follows:

$$R_c = \frac{H_{res}}{H_{base}} \tag{5.9}$$

The reduction coefficient is calculated for all sensors over the domain as well as for the two wave components H_{SS} and H_{IG}. Together with an investigation into the energy density spectra at specific locations on the reef flat, discrepancies between the numerical model and the laboratory simulations can be investigated.

Additionally, the mean spectral period T_{m01} is investigated as well as the ratio of A_{∞}^{rms} / S. The mean spectral period is investigated for all water levels and wave conditions and gives an indication of the importance of the specific frequency components with respect to each other. The ratio A_{∞}^{rms} / S indicates the flow regimes, which are used to determine if, according to Lowe, energy dissipation is expected to be frequency dependent.

Assessing Model Fit

While a qualitative inspection is performed at first, also a quantitative analysis on the comparison between the numerical data and the laboratory data is performed. Several error metrics are used to assess the correlation, including the Root Mean Square Error (RMSE), the bias, and the R-Squared (R^2) metric. The RMSE is a metric for the difference between the model output ($\hat{y}_i$) and the lab data (y_i), giving more weight to larger errors because of the squaring (Equation 5.10). Bias is similar to the RMSE, however, it quantifies the average systematic error between the model output and the laboratory data, indicating whether the model consistently overestimates or underestimates the observed values (Equation 5.11). R^2 is a metric for determining the overall fit of the model by explaining the proportion of variance in the actual data that is captured by the model (Equation 5.12).

While the forcing conditions have a similar spectrum, the time series of the surface elevation will differ. Therefore, the data comparison is performed on either the wave height or energy density spectra of the datasets, both looking at the total wave height or energy density spectrum as well as per individual frequency band. For the RMSE and the bias, the wave height is investigated, while for the R-squared the energy density spectra are compared.

$$\mathrm{RMSE} = \sqrt{\frac{1}{n}\sum_{i=1}^{n}(\hat{y}_i - y_i)^2} \tag{5.10}$$

$$\mathrm{Bias} = \frac{1}{n}\sum_{i=1}^{n}(\hat{y}_i - y_i) \tag{5.11}$$

$$R^2 = 1 - \frac{\sum_{i=1}^{n}(y_i - \hat{y}_i)^2}{\sum_{i=1}^{n}(y_i - \bar{y})^2} \tag{5.12}$$

Expected is that the numerical model is closer to the laboratory results for the cases without a restoration. Therefore, the cases with and without artificial reefs are investigated individually.

6

Experiment Optimisation

This chapter describes the investigation and selection of the positioning and densities for the artificial reef to be used in the laboratory experiment. The optimal location is first assessed, with a detailed analysis of the differences per possible location. Following this, the impact of the density of the reef is examined, from which two specific densities are chosen for the laboratory experiments. A stability analysis is then conducted to determine if additional precautions are needed to ensure the stability of the elements during experimentation. The chapter concludes with the final laboratory setup, including the positioning of the Vectrinos.

6.1. Influence of Location

The optimal location for the artificial reef restoration is chosen based on the location that most effectively reduces incoming wave height at the shoreline. After this initial analysis, a more detailed analysis into the differences between the locations as well as the effects under varying hydrodynamic conditions is investigated.

Figure 6.1 shows the percentage reduction (T_{perc}) in incoming wave height at the beach toe (located 160 m from the offshore boundary). The figure shows both the average reductions for all conditions and water levels, along with reductions per specific component. Restoration 1, positioned on the outer reef flat, shows the lowest overall wave height reduction at only 8%, while Restoration 2 (middle location) and Restoration 3 (inner location) each show a reduction of 12%. Therefore, either location 2 or 3 is suitable for the laboratory experiments. Considering the placement of existing equipment in the flume, location 2 was the most practical choice for setting up the artificial reef.

6.1.1. Data Analysis

In addition to the total reduction in incoming wave height, Figure 6.1 shows the reductions across specific conditions, water levels, and wave components. Clear differences in wave height reduction between these factors can be observed. A more detailed analysis into these differences is therefore required. First, a general analysis of differences between hydrodynamic conditions, including wave conditions and water levels, is performed. Afterwards, the analysis focuses on the differences per location of the restoration and, finally, on the specific wave components.

General Characteristics

The tested wave conditions are presented again in Table 6.1. Generally, an increase in wave height, while the wave period remains constant, results in a reduction in effectiveness of the artificial reefs at all three locations (compare C1, C3 and C11). Similarly, an increase in wave period, while the wave height remains constant, reduces the reefs' effectiveness (compare C1 and C3, and C7 and C9). A third overarching characteristic is that higher water levels further reduce the effectiveness of the restorations.

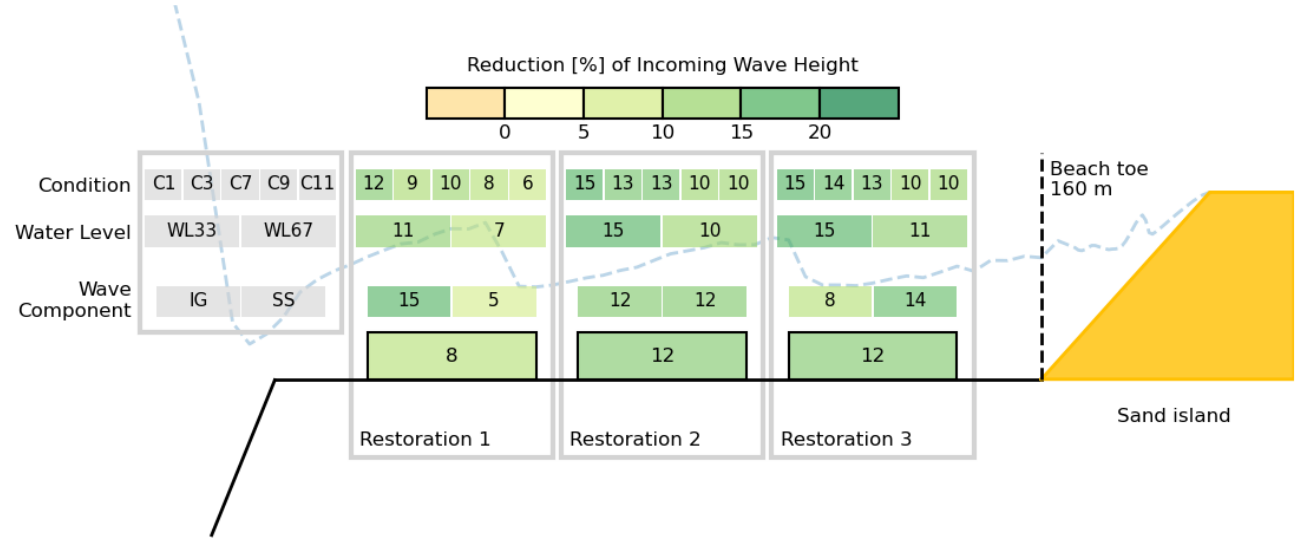

Figure 6.1: Reduction in percentage of incoming wave height at the beach toe (160 m from wave generator). The values indicate the reduction for the specific wave conditions, water levels and wave components with the black lined boxes at the bottom showing the average reduction in incoming wave height for the specific restoration. The dashed blue line shows a time snap of the water level over the flat, clearly showing two highly non-linear bores travelling over the flat.

Wave conditions		
Name	**Hs [m]**	**Tp [s]**
C1	0.5	5.77
C3	0.5	9.24
C7	1.0	5.77
C9	1.0	7.51
C11	1.3	5.77

Table 6.1: The five wave conditions used in the numerical simulations.

To understand and analyse these results, it is essential to examine how SWASH determines wave height reduction through the resistance of a porous medium. This resistance is based on the interaction between the flow velocities and the reef structure. On the reef flat, where the water depth is shallow, the pressure is hydrostatic, and the orbital velocities are uniform throughout the water column. In this scenario, the effectiveness of the reef in dissipating wave energy is primarily a function of the relative depth of the reef. As water levels rise, the relative depth over which the reefs dissipate energy decreases, even though absolute dissipation may increase. This explains the reduction in efficiency when the water level increases from 0.33 m to 0.67 m, as observed in Figure 6.1 for all three restorations: Restoration 1 to Restoration 3. Thus, the water level appears to influence the effectiveness of the artificial reefs, and can potentially also explain the differences observed for varying wave conditions.

Therefore, to investigate how specific wave conditions affect the water level on the reef flat, Figures 6.2 and 6.3 show the wave height transformation across the domain, alongside the water level relative to the flume bottom, for the base case as well as for WL33 and WL67. Only the base case is shown here to focus on offshore wave shoaling, breaking intensity, and setup over the reef. Comparing the water levels on the reef flat (second panel showing $\eta + d_0$), it can be seen that with increasing wave height (e.g., comparing C1, C7, and C11) and longer wave periods (e.g., comparing C1 with C3, and C7 with C9), the setup, and consequently the water level over the reef, increases. This increase reduces the effectiveness of the reefs, as shown in the reduction per wave condition shown in Figure 6.1.

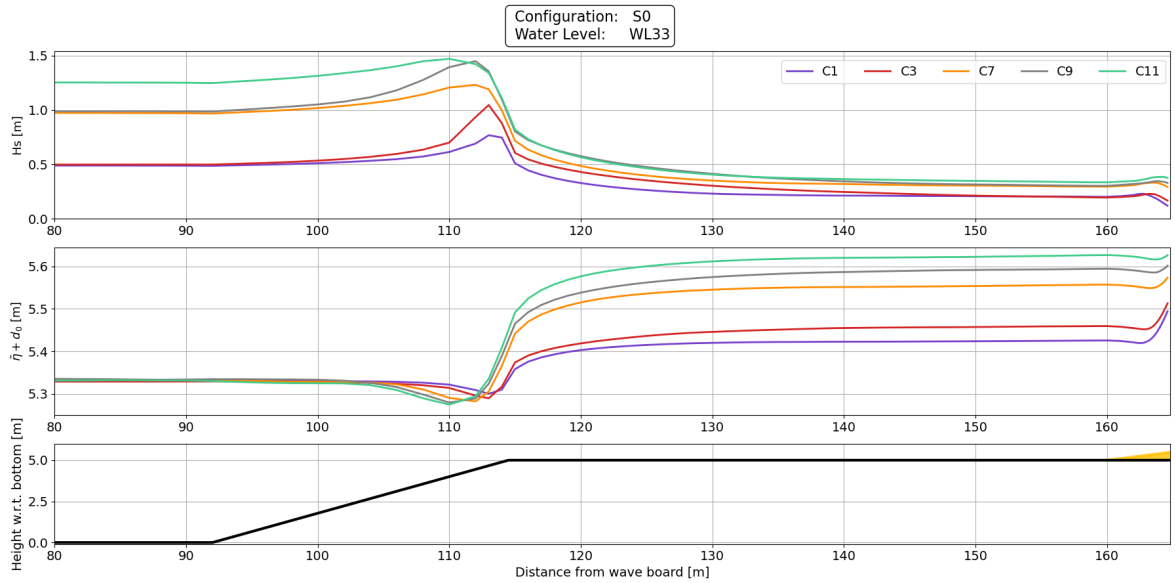

Figure 6.2: Wave height transformation and setup over the reef for the base case **(S0)** and **WL33**. More energetic wave conditions, or conditions with a larger period have larger setups over the reef.

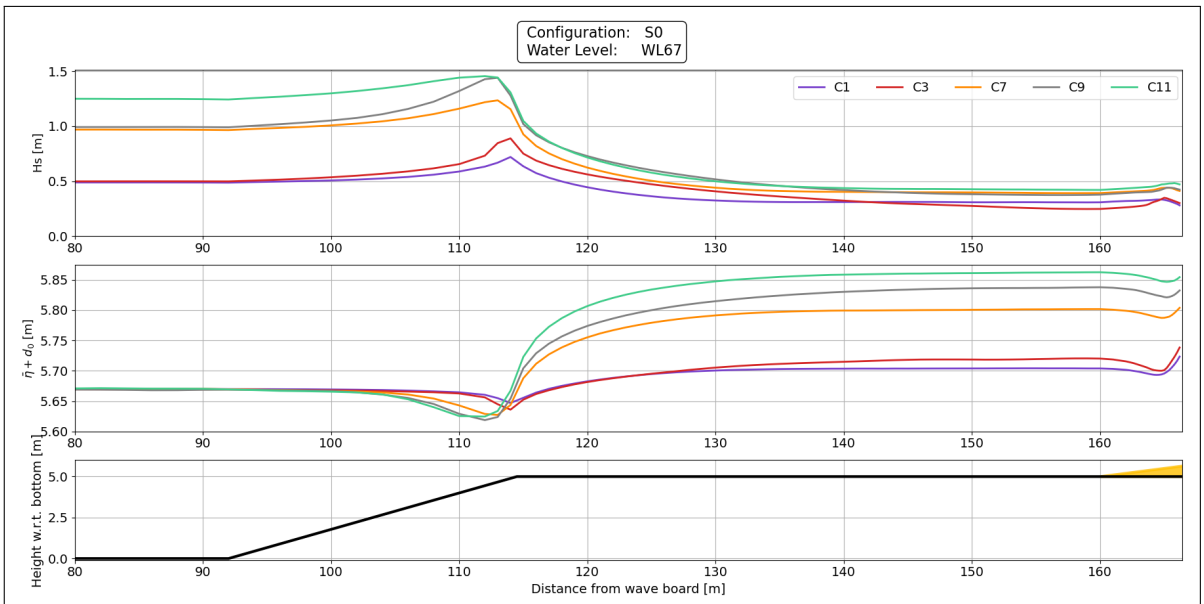

Figure 6.3: Wave height transformation and setup over the reef for the base case **(S0)** and **WL67**. For all wave conditions the water levels on the reef flat are larger than for WL33.

Figures 6.2 and 6.3 also help explain why water levels on the reef flat increase with greater wave heights and longer wave periods. This is analysed by investigating the shoaling zone (approximately x = 110 m, as shown in the first panels of the figures depicting H_S). When the offshore wave height increases (e.g., comparing C1, C7, and C11), the intensity of wave breaking at the reef crest (x = 115 m) increases. In other words, the reduction in wave height is greater, leading to stronger radiation stress gradients and therefore a larger setup over the reef flat.

Additionally, in the shoaling zone it can be observed that longer period waves shoal more than shorter period waves with similar offshore wave height (e.g., comparing C1 with C3, and C7 with C9 in the first panels showing H_S). In intermediate to deep waters, the group velocity of longer period waves is

higher due to their larger wavelengths. As these waves travel into shallower water, their group velocity decreases significantly, resulting in more pronounced shoaling for longer period waves. This enhanced shoaling increases breaking intensity and, consequently, the setup over the reef, reducing the efficiency of wave height reduction for longer period waves.

Another reason for the reduced effectiveness for the more energetic conditions (C9 and C11) could be an increase in setup due to enhanced wave breaking over the artificial reefs. However, analysis shows a maximum increase of setup of only 1 cm near the restorations. Therefore, setup variations due to the reefs are minimal and do not impact their effectiveness, so they have not been investigated further.

6.1.2. Differences per Location

While the general characteristics of wave height reduction are similar across the three locations, as shown in Figure 6.1 and discussed in the subsequent analysis, there are notable differences for the specific wave conditions, water levels, and wave components. Restorations 2 and 3 show comparable reductions under each condition and water level, whereas Restoration 1 shows significantly lower reduction rates. Additionally, the differences per wave component are clear: the offshore restoration reduces most infragravity wave height (15%), while Restoration 3 is most effective at reducing sea/swell wave height (14%). As a result, an analysis focusing on these specific wave components is conducted, along with an examination of how these components transform across the domain.

Transformation of SS and IG Wave Components

Before analysing the effect of the reef restorations on the SS and IG waves, the transformation of these waves for the base case (S0) is examined. This investigation provides a clearer understanding of the wave transformation process when the artificial reefs are introduced on the flat. Figure 6.4 illustrates the transformation of the base case S0 for both the incoming SS (solid line) and IG (dashed line) waves across the domain, with WL33 shown in the top panel and WL67 in the middle panel. For clarity, only three wave conditions are presented: C3 (H_S = 0.5 m, T_p = 9.24 s), C3 (H_S = 1.0 m, T_p = 5.77 s), and C11 (H_S = 1.3 m, T_p = 5.77 s).

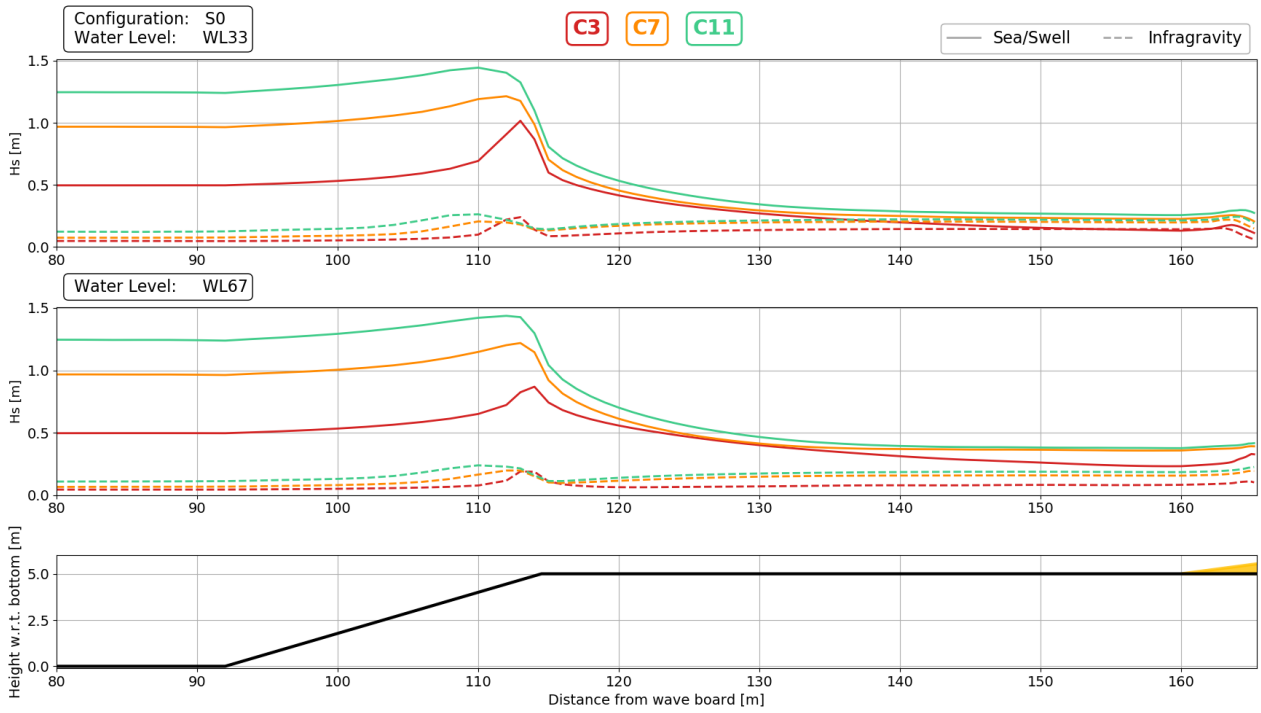

Figure 6.4: Wave height transformation of the incoming Sea/Swell (solid lines) and Infragravity (dashed lines) wave components over the domain for the base case S0. The figure shows the transformation for wave conditions C3, C7, and C11, with WL33 shown in the top panel and WL67 in the middle.

The analysis of Figure 6.4 focuses on three sections of the domain: the offshore region (from x = 80 to x = 100 m), the shoaling zone (from x = 100 to x = 115 m), and the reef flat (from x = 115 to x = 165 m). Offshore, for both water levels (WL33 in the top panel and WL67 in the middle panel), the incoming sea/swell (SS) waves (solid lines) are the dominant contributor to the wave height, with the infragravity (IG) waves (dashed lines) remaining close to zero for all conditions (C3, C7, and C11).

In the shoaling zone (x = 100 to x = 115 m), the more energetic condition (C11) shows less shoaling for both SS and IG waves compared to the less energetic condition (C3). Furthermore, the lower water level (WL33) shows more shoaling and breaking for the SS waves compared to WL67, while for both water levels and all three wave conditions, the IG waves show minimal shoaling and breaking.

On the reef flat, extending from x = 115 m to the shoreline, interesting observations can be made. For both water levels, the SS waves initially show a steep gradient in wave height reduction as they move onshore, which gradually flattens out around x = 140 m. The large reduction near the crest is attributed to wave breaking, while friction closer to the shore dominates the wave height reduction. In contrast, the IG waves show an increase in wave height as they move onshore, for all conditions and both water levels, with the rate of increase decreasing shoreward. This increase in wave height is attributed to both breakpoint forcing and energy transfer from the SS waves to the IG waves.

Differences per Wave Component

Here an analysis into the effect of the artificial reefs on the specific wave components is conducted, first for the sea/swell component. Figure 6.5 shows the reduction of incoming SS wave height at the beach toe for each restoration, wave condition, and water level. It is similar to Figure 6.1, but shows the incoming sea/swell waves instead of the incoming total wave height. Significant differences between the restoration can be observed; where the outer restoration (Restoration 1) reduces the SS wave height by only 5%, the middle and inner restoration (Restoration 2 and 3, respectively) reduce the wave height by 12% and 14%, respectively. Similar to the total wave field, an increasing wave height (e.g., comparing C1, C7, and C11) as well as an increasing period (e.g., comparing C1 with C3, and C7 with C9) results in a lower reduction rate for all three locations, with Restoration 1 showing the lowest values for all components.

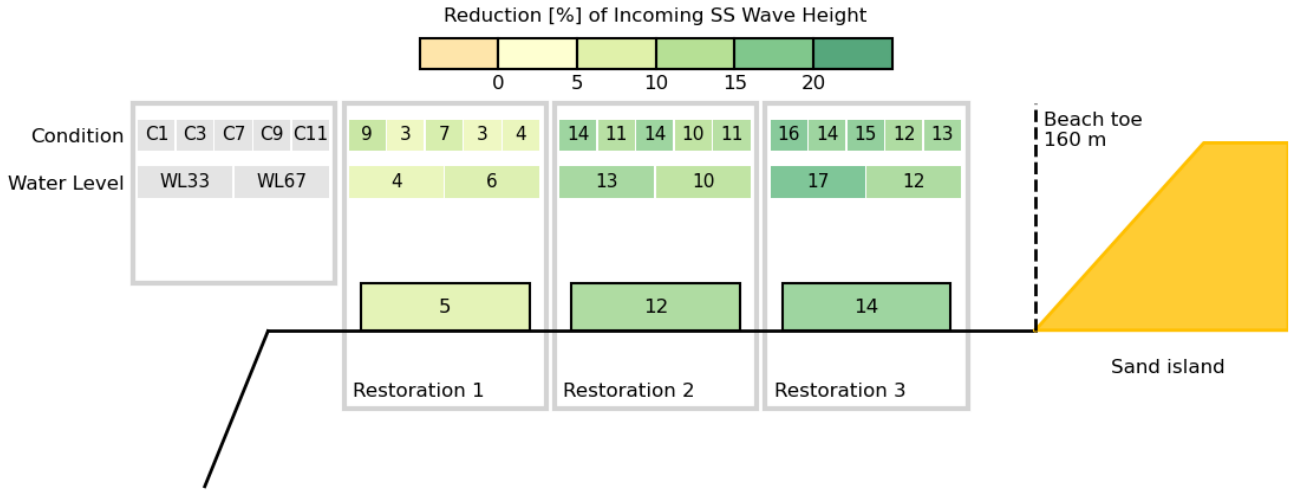

Figure 6.5: Reduction in percentage of incoming **Sea/Swell** wave height at **the beach toe**. The values indicate the total reduction per location (black-lines boxes) as well as for the specific wave conditions and water levels.

Although Figure 6.5 shows the relative reduction in wave height at the shoreline, examining wave height reduction directly behind the restoration (shoreward side) also provides insight. This allows us to determine whether the observed differences between locations arise from dissipation over the restoration itself or from subsequent wave energy transformation over the reef flat. Figure 6.6 shows the reduction in percentage in incoming SS wave height directly behind each restoration. The results

differ noticeably from those measured at the beach toe (Figure 6.5). Here, the differences between the restoration locations are almost identical. All three restorations reduce the SS wave height by approximately 15%, and the reduction between the restorations for the specific wave conditions and water levels is almost identical.

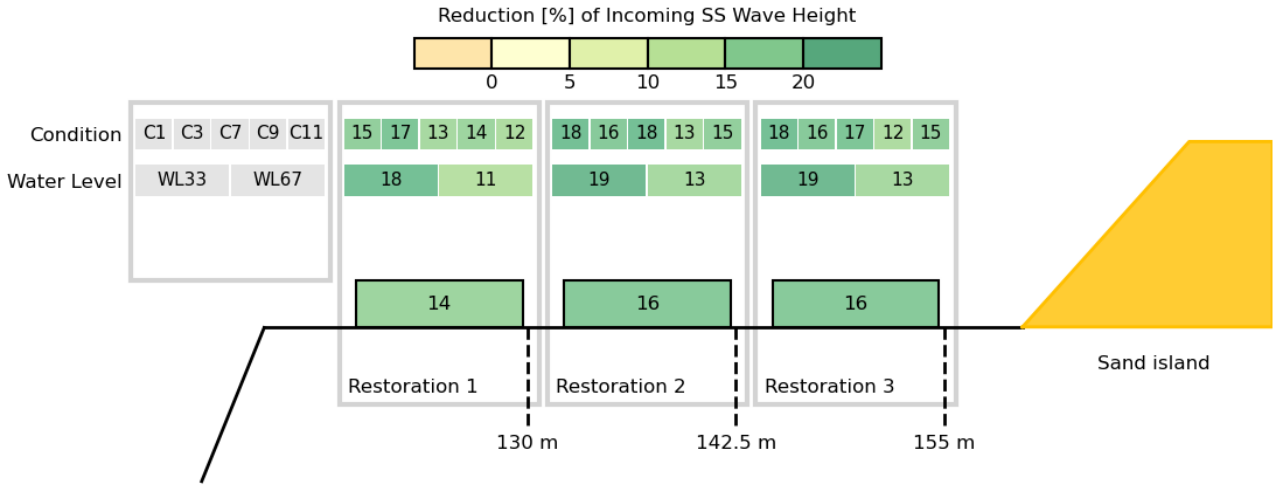

Figure 6.6: Reduction in percentage of incoming **Sea/Swell** wave height **directly behind** the restorations (130, 142.5 and 155 m for restoration 1, 2 and 3 respectively).

The fact that the reduction in incoming SS wave height is almost identical for each restoration when measured directly behind them (Figure 6.6), but varies significantly when measured at the beach toe (Figure 6.5), suggests that the reduction at the beach toe is primarily due to the subsequent transformation of wave energy over the reef flat. This can be further explored by examining the transformation of sea/swell (SS) waves over the reef flat. Figure 6.7 illustrates this transformation for wave condition C7. Only this specific wave condition is shown, as the results for other wave conditions are similar. The top panel depicts the transformation of H_{SS} for WL33, while the middle panel shows the transformation for WL67.

For both water levels, the base case (S0) shows a high rate of wave energy dissipation near the reef crest (x = 120 m), which gradually decreases to a nearly constant rate further shoreward (around x = 135 m). The initial high dissipation rate is probably caused by wave breaking, while the nearly constant rate further onshore is attributed to bottom friction, as was also concluded from Figure 6.4.

Restoration 1, the outermost restoration, is positioned in the region where waves are still breaking and dissipation rates are high (x between 120 and 130 m). In contrast, Restorations 2 and 3 are located further shoreward, in the area where the dissipation rate has already decreased to a steady level (x = 132.5 to x = 155 m), dominated by bottom friction. As shown in Figure 6.6, the reduction in wave height directly behind each restoration is similar, at approximately 15%. However, Figure 6.7 shows that the dissipation rate decreases significantly when moving shoreward from the restorations.

This implies that while the initial wave height reduction is consistent across the three restorations, Restoration 1 is located in a region where the base case is still dissipating significant amounts of energy. As a result, this reduced dissipation rate shoreward of Restoration 1 compared to the base case results to an overall lower reduction in wave height at the beach toe compared to Restorations 2 and 3, which are positioned where the dissipation rate has become relatively constant.

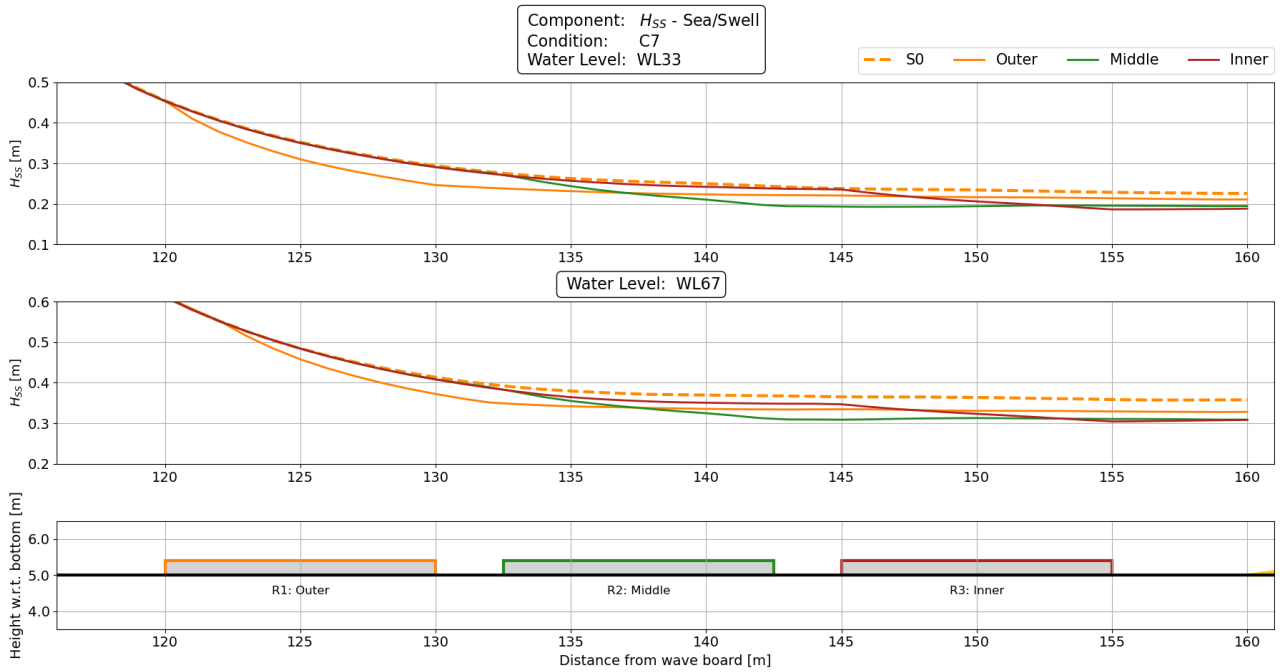

Figure 6.7: Transformation of the incoming **Sea/Swell** wave height H_{SS} for condition **C7** over the reef flat, for the base case (dashed line) and the three restorations. The top panel shows the transformation of H_{SS} for WL33, while the middle panel the transformation for WL67.

A similar investigation is performed for the infragravity waves. Figure 6.8 and 6.9 show the reduction in incoming infragravity wave height at the beach toe and directly behind each restoration, respectively. The figures show a notable difference between the behaviour of the sea/swell and infragravity wave components. For the infragravity waves, the percentage reduction is almost identical at both the location directly behind a restoration and at the shoreline, suggesting that energy reduction mainly occurs over the restoration itself, rather than through subsequent transformation across the reef flat.

In both Figures Restoration 1 reduces the incoming IG wave height most significantly by around 15%, while Restoration 2 and 3 reduce the height by 12 and 8%, respectively. Notably, the inner restoration, Restoration 3, shows significantly lower reductions, particularly under more energetic conditions (C9 and C11). In these cases, both figures show a reduction of only about 5%.

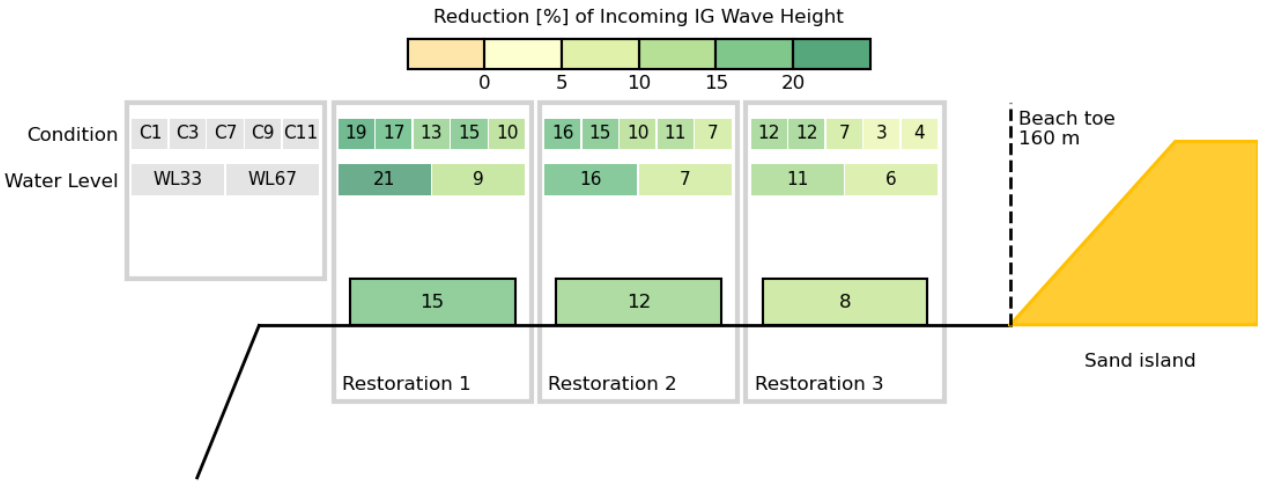

Figure 6.8: Reduction in percentage of incoming **Infragravity** wave height at the **beach toe** (160 m from wave generator). The values indicate the total reduction per location (black-lines boxes) as well as for the specific wave conditions and water levels.

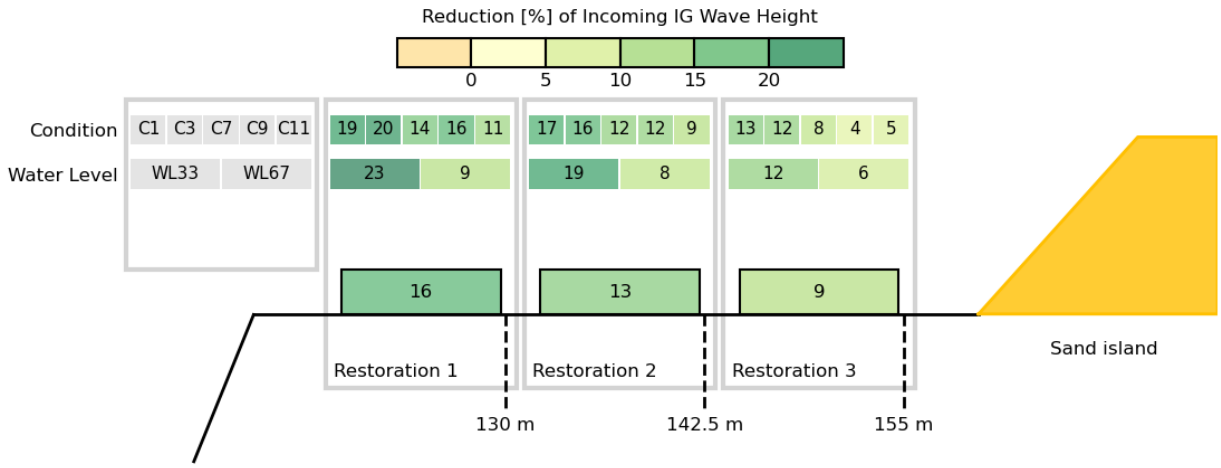

Figure 6.9: Reduction in percentage of incoming **Infragravity** wave height **directly behind** the restorations (130, 142.5 and 155 m for restoration 1, 2 and 3 respectively).

An analysis of the wave height transformation over the flat for wave condition C7 is also conducted for the incoming infragravity waves (Figure 6.10). The top panel shows the transformation of H_{IG} for WL33, while the middle panel shows WL67. As also shown in Figure 6.4, the infragravity waves gain energy over the flat, with the rate of increase decreasing shoreward. This increase in wave height is both a result of breakpoint forcing as well as energy transfer from the sea/swell waves to the infragravity waves.

For all three restorations, Figure 6.10 shows that the shoreward increase in infragravity wave height is similar to that of the base case (S0, dashed orange line). However, if the restoration is placed in a region with a high rate of change in infragravity wave height, such as Restoration 1 (x = 120 m to x = 130 m), the infragravity waves are attenuated more significantly. This effect is hypothesised to be related to wave groupiness, a concept discussed further in Chapter 9.

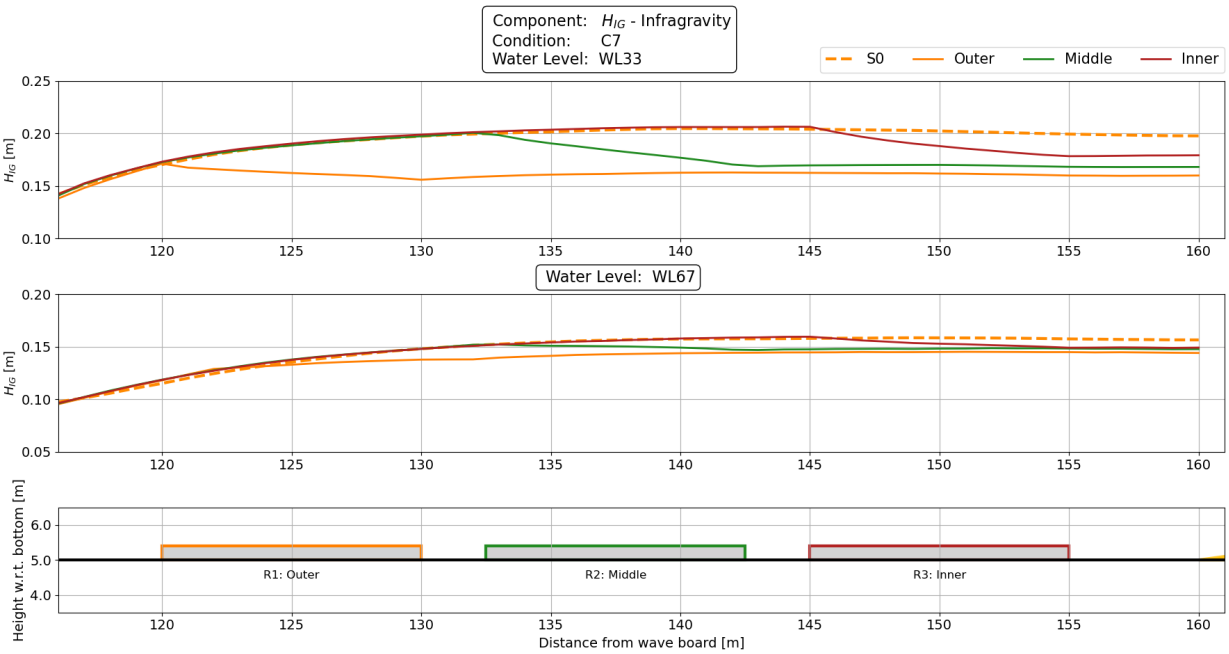

Figure 6.10: Transformation of the incoming **Infragravity wave height** H_{IG} for condition **C7** over the reef flat, for the base case (S0) and the three restorations. The top panel shows the transformation of H_{IG} for WL33, while the middle panel shows WL67.

6.2. Influence of Reef Element Density

Four different densities are investigated at the location of the middle restoration, positioned 132.5 m from the wave board. The porosities of these densities range from 0.90 for the lowest density (Density 1) to 0.78 for the highest (Density 4). These densities correspond to the number of elements in the artificial reef to be used in the lab. Figure 6.11 shows the reduction in percentages of incoming wave height at the beach toe. As can be observed, increasing density leads to a greater reduction in wave height, with the highest density reducing the wave height by 19% compared to 12% for the lowest density. Additionally, the differences per wave condition, water level and wave component are consistent in magnitude between the different densities. In other words, an increase in density has a similar effect on the wave height reduction for each wave condition, water level and wave component.

For reference, Density 1 consists of 66 elements, while Density 4 has 153, more than twice as many. However, the additional wave height reduction is only around 50% greater. Nevertheless, Density 4 was selected for the laboratory experiments in combination with either Density 1 or Density 2. Density 3 was not used, as the difference in wave height reduction compared to the others was 4% or less, making it harder to detect variations in laboratory results. Ultimately, Densities 2 and 4 were chosen for the experiments. Although Density 2 gives the largest difference in wave height reduction, combining Densities 2 and 4 simplified the arrangement of instrumentation during the tests, as detailed further in section 7.4.

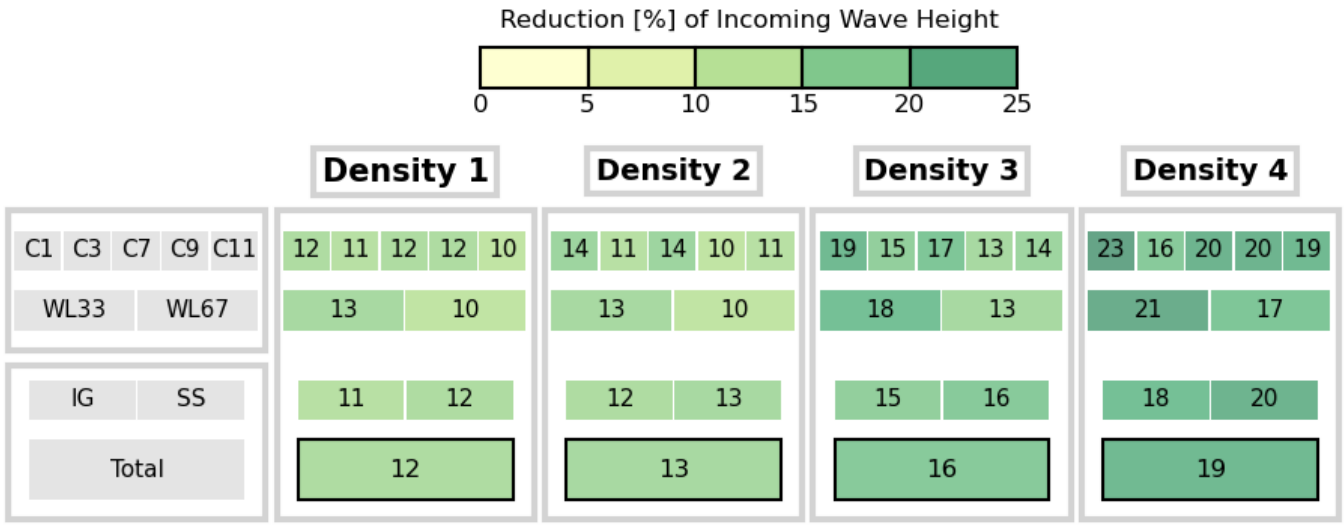

Figure 6.11: Reduction in percentage of incoming wave height at the beach toe (160 m from wave generator) for the four densities tested. The restoration is located in the middle of the reef flat between x = 132.5 and x = 142.5 m.

Flow Regimes

In Section 4.4, the expected flow regimes were determined based on the ratio A_{∞}^{rms} / S. However, these calculations used the rms free-stream velocity for the base case. Here, the same ratio is recalculated using the depth-averaged velocity directly in front of and behind the restoration. Although only minor differences are expected, this approach leads to more accurate estimates of the flow regimes.

Table 6.2 shows the mean values of $U_{\infty,\omega}^{rms}$, T_{m01} and A_{∞}^{rms}, along with the range in A_{∞}^{rms}/S across all wave conditions and water levels. The data shows that density has a limited influence on both the rms free-stream velocity and the mean spectral period, resulting in similar mean orbital excursion lengths for all densities. However, the range of A_{∞}^{rms}/S differs due to the differences in spacing. In general, the ratio is above 1, indicating the general flow regime. Even the largest ratio of 4.5 remains within this regime. Therefore, for all densities, frequency dependent energy dissipation is expected in the laboratory results.

Density	Spacing [m]	$U_{\infty,\omega}^{rms}$ [m/s]	$T_{m01}[s]$	A_{∞}^{rms} [m]	A_{∞}^{rms}/S [-]
D1	0.54	1.1	4.9	0.82	0.7 - 2.3
D2	0.42	1.0	5.2	0.87	0.9 - 3.1
D3	0.34	1.0	5.0	0.81	1.0 - 3.6
D4	0.27	0.9	5.1	0.80	1.3 - 4.5

Table 6.2: Range in ratio's for A_{∞}^{rms} over S, across all wave conditions and water levels, for the four different tested densities, including mean values for $U_{\infty,\omega}^{rms}$, T_{m01} and A_{∞}^{rms}.

6.3. Stability

The artificial reefs consist of individual elements placed on the flume bed. These elements are subject to heavy wave loads and flow velocities but are required to stay in place. Morison (1950) developed equations which determine the stability criteria for these individual elements. While these equations have been developed for slender cylinders, they have also effectively been applied to structures with a more complex shape such as the MOSES units and Reef Balls (Düzbastılar and Şentürk, 2009; Harris and Gonzalez, 2005). A requirement for the artificial reef elements used for these experiments is that they remain stable under testing. The Morison equation is used to determine this stability criteria. If the elements are deemed unstable, they need to be anchored to the bottom of the flume.

Morison Equation

The Morison equations are semi-empirical and based on a momentum balance in horizontal forces, and uses empirical coefficients. The forces on a structure are estimated based on velocities and accelerations around the reef, which are estimated with linear wave theory. An element is deemed stable if the mobilizing force F_{wave} is smaller than the resisting force $F_{resisting}$. The mobilizing force F_{wave} (Equation 6.1) is the sum of a drag component f_{drag} (Equation 6.2), depending on the flow velocity around a structure, and an inertia component $F_{inertia}$ (Equation 6.3), depending on the flow acceleration around a structure.

$$F_{wave} = F_{drag} + F_{inertia} \tag{6.1}$$

$$F_{drag} = C_D \frac{\rho_w A_p u^2}{2} \tag{6.2}$$

$$F_{inertia} = C_M \rho_w V a \tag{6.3}$$

In these equations:

C_D	[-]	=	Coefficient of drag
ρ_w	[kg/m^3]	=	Water density
A_p	[m^2]	=	Cross-sectional area in the direction of flow
u	[m/s]	=	Horizontal flow velocity
C_M	[-]	=	Coefficient of inertia
V	[m^3]	=	Volume of the reef element
a	[m/s^2]	=	Flow acceleration

These mobilizing forces need to be balanced by a resisting force $F_{resisting}$ (Equation 6.4) in order for the element to be stable. The resisting force is based on the roughness of the bed as well as the weight and

shape of an element. The resisting force is limited by the buoyancy $F_{buoyancy}$ of the element (Equation 6.5) as well as a lift force F_{lift}, caused by the flow of water around the structure (Equation 6.6).

$$F_{\text{resisting}} = \mu \left(W_{\text{object}} - F_{\text{buoyancy}} - F_{\text{lift}} \right) \tag{6.4}$$

$$F_{\text{buoyancy}} = \rho_w V_g \tag{6.5}$$

$$F_{\text{lift}} = C_L \frac{1}{2} \rho_w S u^2 \tag{6.6}$$

In these equations:

μ	[-]	=	Coefficient of friction
W_{object}	[kg]	=	Weight of a reef element
V_g	[m^3]	=	Volume of a reef element
C_L	[-]	=	Coefficient of lift
S	[m^2]	=	Planform area of a reef element

The Morison Equations require three empirical coefficients: C_D, C_M, C_L. The value of these coefficients is highly dependent on the shape of a structure, which means that ideally these values need to be calibrated based on laboratory stability tests. Due to time constraints however, the values for these coefficients are based on limited available literature.

Linear Wave Theory

As mentioned earlier, the flow velocity and flow acceleration used for the Morison equation are based on linear wave theory. For the flow velocity, the peak orbital velocity $\hat{u}$ at the bottom of the water column is used, while for the acceleration, a, the acceleration at this location is used. Although these parameters could be directly obtained from the SWASH simulations, they are instead determined using linear wave theory to align with standard practices in applying the Morison equation, which generally rely on this approach. A limitation of using linear wave theory is that it does not account for the inherent randomness of waves, leading to uncertainties in the calculated forces exerted on the elements.

These parameters, $\hat{u}$ and a, depend on the significant wave height H_s, the spectral wave period $T_{m-1,0}$, the water depth h and the wave length L, of which the latter can be calculated by linear wave theory with equation 6.7. The peak orbital velocity $\hat{u}$ can be calculated with equation 6.8 and the acceleration a with equation 6.9.

$$L = \frac{g \cdot T_{\text{m-10}}^2}{2\pi} \cdot \tanh\left(\frac{2\pi d}{L}\right) \tag{6.7}$$

$$\hat{u} = \frac{\pi H_s}{T_{\text{m-10}}} \frac{1}{\sinh(kh)} \tag{6.8}$$

$$a = \frac{2 H_s \pi^2}{T_{\text{m-10}}^2} \frac{1}{\sinh(kh)} \tag{6.9}$$

The wave number k is given by

$$k = \frac{2\pi}{L} = \frac{2\pi}{\sqrt{\frac{gT^2}{2\pi}}}$$

Stability Criteria

To calculate the required weight of the individual elements, several parameters must be defined, including the empirical coefficients C_D, C_M and C_L, as well as the specific dimensions of the elements themselves. The hydrodynamic parameters H_s and T_{m-10}, as well as the water level h, are obtained from the SWASH simulations for the two tested configuration. These values are calculated by averaging over the 10-meter length of the restoration area. Conservative values for the empirical coefficients are selected based on findings from comparable research (Table 6.3).

Variable	Description	Value	Unit	Argumentation
C_d	Drag coefficient	2	-	Based on research of Diederen (2022). A value of 2 is a relatively high value for the drag coefficient.
C_m	Coefficient of Inertia	3	-	In general the coefficient of inertia is equal to 2. However, for reefs placed close to the seabed k_m a more appropriate value is 3 (Diederen, 2022).
C_l	Coefficient of lift	2	-	Very limited literature is available on the coefficient of lift. Expected is that the lift term is in the same order of magnitude as the drag and inertia terms.
A_p	Element frontal area	0.068	m^2	The element frontal area perpendicular to the flow.
V	Element Volume	0.018	m^3	The element volume.
S	Element planform	0.106	m^2	The element planform acquired from the 3D model.
ρ_w	Element density	1900	kg/m^3	The density of the concrete printed by Coastruction is 1900 kg/m^3.
μ	Friction coefficient of the bed	0.5	-	The elements are placed on a concrete bed in the Delta flume, which has a friction coefficient of approximately 0.5.

Table 6.3: Values for the different parameters employed in the Morison Equation

The elements must remain stable for all experimental runs. Therefore, the required weight for each run has been calculated, showing that the highest required weight is 28.7 kg for condition C11 at WL67. The lowest required weight is 24 kg for condition C1 at WL33, with a median weight of 28.2 kg. Table 6.4 shows the mean spectral period, wave height, and water level together with the corresponding required weights and the actual weight of the elements. The printing process of the elements is not perfect, and although the average weight of the elements is 30 kg, element weight varies by around 2 kg. This means that some elements fail to meet the minimum required weight.

Additionally, there is an uncertainty for the required weight of the elements, which is based on hydrodynamic conditions derived from a numerical model. This model might not be able to fully capture a real-world case and therefore, actual values could be higher. To account for these uncertainties, an arbitrary safety factor of 1.2 is applied to the required weight, which increases it to 34.4 kg, exceeding the weight of the elements. Therefore, the elements must be anchored to the flume during testing. This is accomplished by securing two screws in each element and fastening them to the bottom of the flume.

Hydrodynamic run	T_{m-10} [s]	H_s [m]	h [m]	Required weight [kg]	Element weight [kg]
WL67C11	19.3	0.50	0.86	28.7	30 ± 2

Table 6.4: Required weight of a single element compared to the actual element weight.

6.4. Final Laboratory Setup

The two configurations being tested correspond to densities D2 and D4, which consist of 91 and 153 elements, respectively. For clarity, D2 will be referred to as S1, representing the low-density configuration, while D4 will be referred to as S3, representing the high-density configuration. For the CREST experiments another configuration with additional artificial reef elements (MOSES) constructed by Reef-Systems (2024) was used. This configuration is referred to as S2. However, no further analysis into this configuration is performed in this thesis.

The baseline scenario will be called S0. Both configurations span a distance between 136 meters and 146 meters from the wave board. Although the optimal starting position was identified as 132.5 meters, the presence of existing instrumentation on the platform required the setups to be placed at 136 meters. The exact positioning with respect to each other depends on the positioning of the Vectrinos, which are used to measure the in-canopy flow field.

6.4.1. Vectrino Positioning

A total of six Vectrinos are used to measure the in-canopy flow structure. These are arranged in two sets of three, with each set forming a vertical profile that measures flow at three different points within the water column, approximately 10 cm, 20 cm, and 30 cm above the bed. Both a location of accelerated flow and a location of sheltering are chosen for the Vectrino array positioning.

To determine these locations, preliminary CFD simulations conducted by Akshay Patil are analysed (Figure 6.12 and Figure 6.13). Patil's CFD simulations, performed using direct numerical simulation (DNS), model turbulent channel flow under a pressure gradient (Patil and Fringer, 2022). These simulations, based on a rigid lid assumption, differ in density, spacing, and number of elements compared to this study. However, the identified zones of sheltering and acceleration are expected to align similarly. Figure 6.12 demonstrates the reduced in-canopy flow velocity relative to the free-stream flow above the canopy, while Figure 6.13 shows a clear acceleration of flow between two elements and a sheltered area directly behind an element.

The positions of the Vectrino arrays for the low-density (S1) and high-density (S3) configurations are shown in Figures 6.14 and 6.15, respectively. Array A is located directly behind an element, representing a sheltered zone, while Array B is positioned between two elements, capturing an accelerated flow region. The two selected velocity profiles, A and B, show distinct characteristics of in-canopy flow, capturing the spatial variability within the canopy. Together, these profiles describe the in-canopy flow structure. The attenuation of the in-canopy flow can be described relative to the free-stream velocity above the canopy. All three measurement points in the two profiles are located within the canopy, capturing only the in-canopy flow. The free-stream velocity, however, is obtained from the experimental runs of the base scenario (S0). Due to the relatively uniform vertical velocity profile in the shallow water conditions on the reef flat, the base scenario can be used to describe the free-stream velocity.

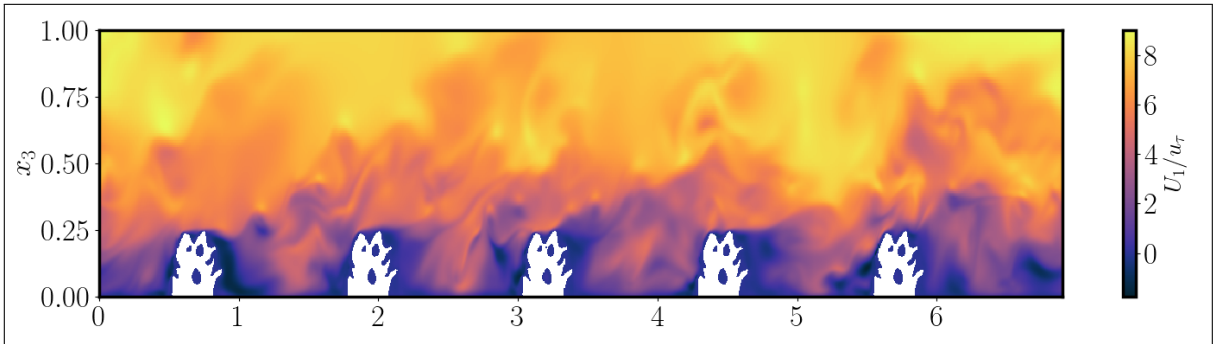

Figure 6.12: Side view of preliminary CFD simulations performed by Akshay Patil, showing a significantly larger flow velocity above the canopy. The x-axis denotes the cross-shore direction, clearly demonstrating a reduced flow velocity directly behind each element. U_1 represents the mean velocity in cross-shore direction and μ_T the shear/friction velocity. Negative or values close to zero indicate sheltered zones or recirculation regions. High values represent high-speed, or accelerated, flow regions.

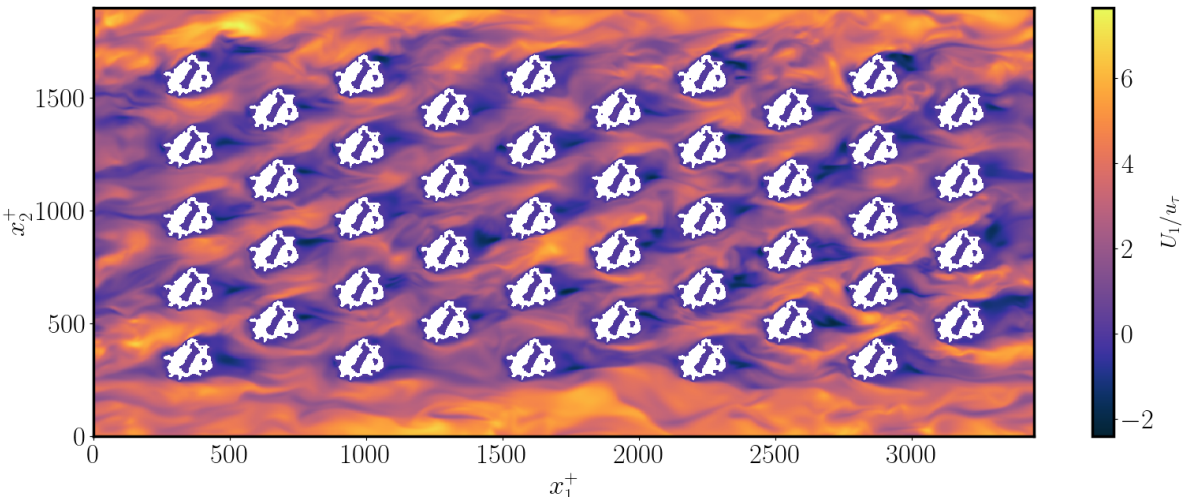

Figure 6.13: Top view of preliminary CFD simulations performed by Akshay Patil, showing accelerated flow in between elements (red/yellow areas) and flow velocity reduction directly behind elements (dark blue area). x_2^+ is the cross-flume direction and x_1^+ the cross-shore. The figure is a slice at x_3 = 0.08 m (Figure 6.12).

6.4.2. Final Configurations

Figures 6.14 and 6.15 show the precise layout of the elements, as well as the locations of the Vectrinos, represented by rectangular shapes in the figures. The velocity profiles A and B are located around the middle of the artificial reef, where the effects of the initial zone as well as wall boundary effects are minimal. As can be seen, location A measures in a sheltered area right behind an element while location B is located exactly in between two elements.

The positioning of the Vectrinos were chosen carefully to ensure that they remain as stationary as possible throughout the experiments. Given the limited time available for conducting the experiments, minimizing the need to reposition the Vectrinos is crucial to ensure that the experiments are completed within the available time.

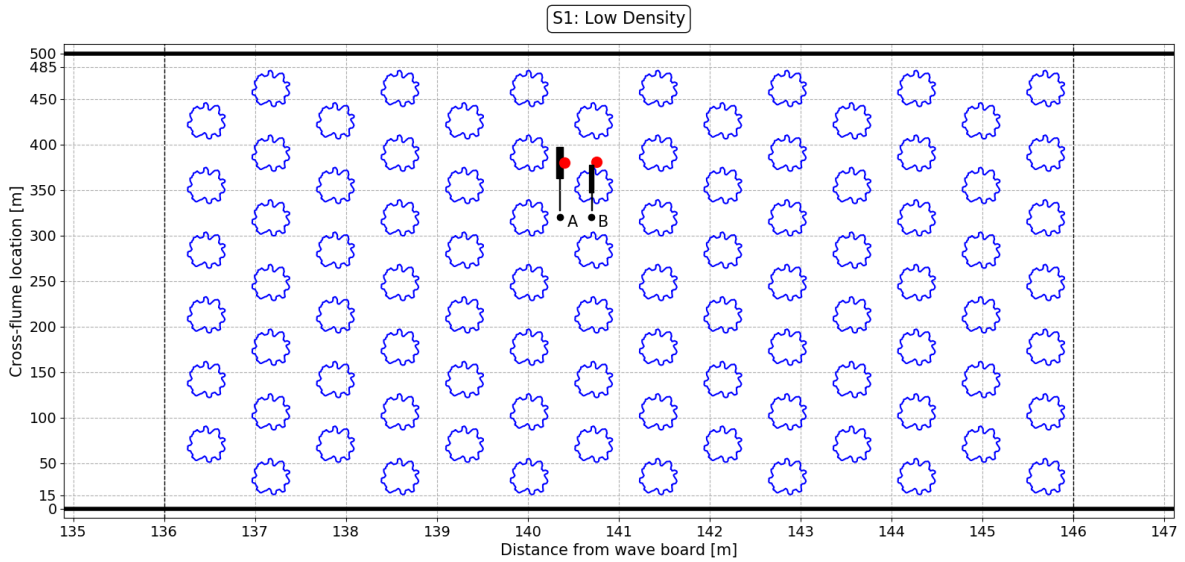

Figure 6.14: Top view of configuration **S1: Low Density** (91 elements). The location of the Vectrino's (rectangular shapes), the measurement locations A and B (black dots) and the frame for the instrumentation (red). The outer elements are positioned **18 cm** away from the wall, with a centre-to-centre distance of **70.7 cm** in both the x and y directions.

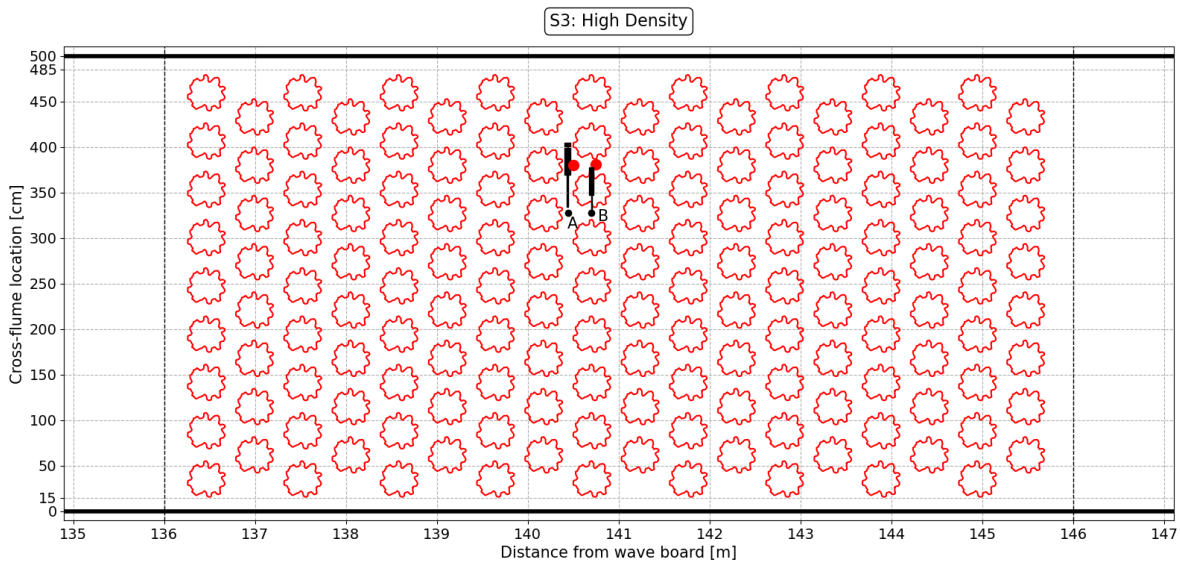

Figure 6.15: Top view of configuration **S3: High Density** (153 elements). The location of the Vectrino's (rectangular shapes), the measurement locations A and B (black dots) and the frame for the instrumentation (red). The outer elements are positioned **18 cm** away from the wall, with a centre-to-centre distance of **53 cm** in both the x and y directions.

Figure 6.16 shows the positioning of the elements for both configurations relative to one another. The figure shows that the locations of the Vectrinos remain largely consistent between the experiments, requiring only minor adjustments to realign them with the elements. This reduced need for repositioning not only saves time but also minimizes potential errors associated with moving the equipment.

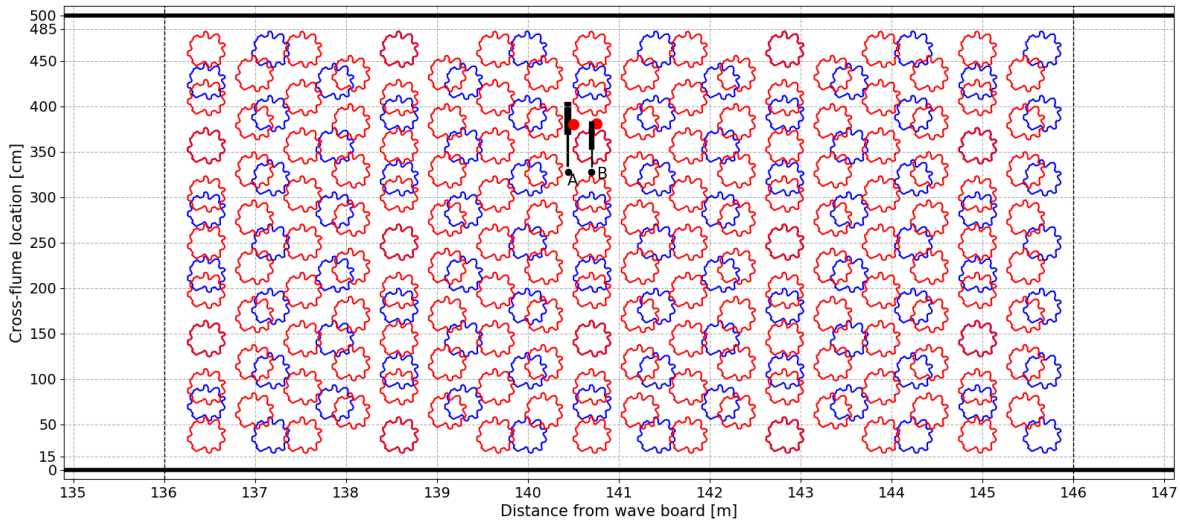

Figure 6.16: Top view of S1 and S3. The configurations are positioned such that the Vectrinos (black rectangular shapes in the figure) do not have to be repositioned. The measurement locations A and B are indicated by the black dot. The frames to which the Vectrinos are attached are indicated by the red dots.

7

Data Analysis & Comparison

It was initially planned to perform 10 simulations for each of the three configurations. However, due to unforeseen difficulties with the pressure sensors, experimental runs had to be rerun. Due to time and cost constraints, only a limited number of experiments were able to be performed again. Namely, the base case (S0) and the high density artificial reef (S3) could be tested as well as wave conditions C3, C7 and C11, for both water levels. While it is significantly less than initially planned, it is still sufficient to perform reliable analysis on the comparison between the two datasets as well as an analysis into the effectiveness of the artificial reef.

Run #	Configuration	Water level		Wave condition		
	Name	Name	Exact Height [m]	Name	Hs [m]	Tp [s]
1	S0	WL33	0.37	C3	0.5	9.24
2	S0	WL33	0.32	C7	1.0	5.77
3	S0	WL33	0.27	C11	1.3	5.77
4	S0	WL67	0.70	C3	0.5	9.24
5	S0	WL67	0.67	C7	1.0	5.77
6	S0	WL67	0.66	C11	1.3	5.77
7	S3	WL33	0.34	C3	0.5	9.24
8	S3	WL33	0.31	C7	1.0	5.77
9	S3	WL33	0.26	C11	1.3	5.77
10	S3	WL67	0.72	C3	0.5	9.24
11	S3	WL67	0.69	C7	1.0	5.77
12	S3	WL67	0.69	C11	1.3	5.77

Table 7.1: All twelve performed experimental runs with the exact water level on the reef flat as present during experimentation.

The numerical simulations differed from the laboratory experiments due to variations in the positioning of the artificial reefs as well as the water levels, requiring the rerunning of the simulations under the exact experimental conditions. Table 7.1 shows the hydrodynamic conditions for the 12 performed experimental runs including the exact water height present on the reef flat, which was extracted from the most offshore pressure sensors as described in Chapter 5.

Initially, an analysis is performed into the laboratory data to assess the effectiveness of the artificial reef and its impact on the transformation of the significant wave height. A comparison is then made between the numerical and laboratory results for case S0, which represents the scenario without an artificial reef. The effectiveness of the artificial reef is then assessed by comparing configuration S3 with S0, focusing on differences in the specific wave components SS and IG. The chapter concludes with an assessment of the model fit, evaluating the R-squared, RMSE, and bias.

7.1. Laboratory Data Analysis

Before analysing the accuracy of the SWASH simulations in describing the laboratory data, the laboratory results are first examined to evaluate the transformation of total wave height (incoming and reflected) over the reef for both the base case (S0) and the case with an artificial reef (S3). Figures 7.1 and 7.2 illustrate the transformation of the significant wave height, H_S (Panel A), and the water level, including setup η (Panel B), for WL33 and WL67, respectively.

In Panel A of both Figures 7.1 and 7.2, the wave height for the base case (S0, circular markers) and the artificial reef case (S3, triangular markers) is identical up to the restoration location (x = 136 m) for all three wave conditions (C3, C7 and C11). Onshore of the artificial reef, the wave height reduction is minimal but most significant for WL33. At the most onshore sensor (x = 155 m in the figures), the reduction in wave height for WL33 across all conditions is approximately **0.06 m**, corresponding to an **11%** decrease in total wave height. For WL67, the wave height reduction is smaller, with a decrease of approximately **0.03 m**, or **5%** of the total wave height, at the same onshore location across all conditions.

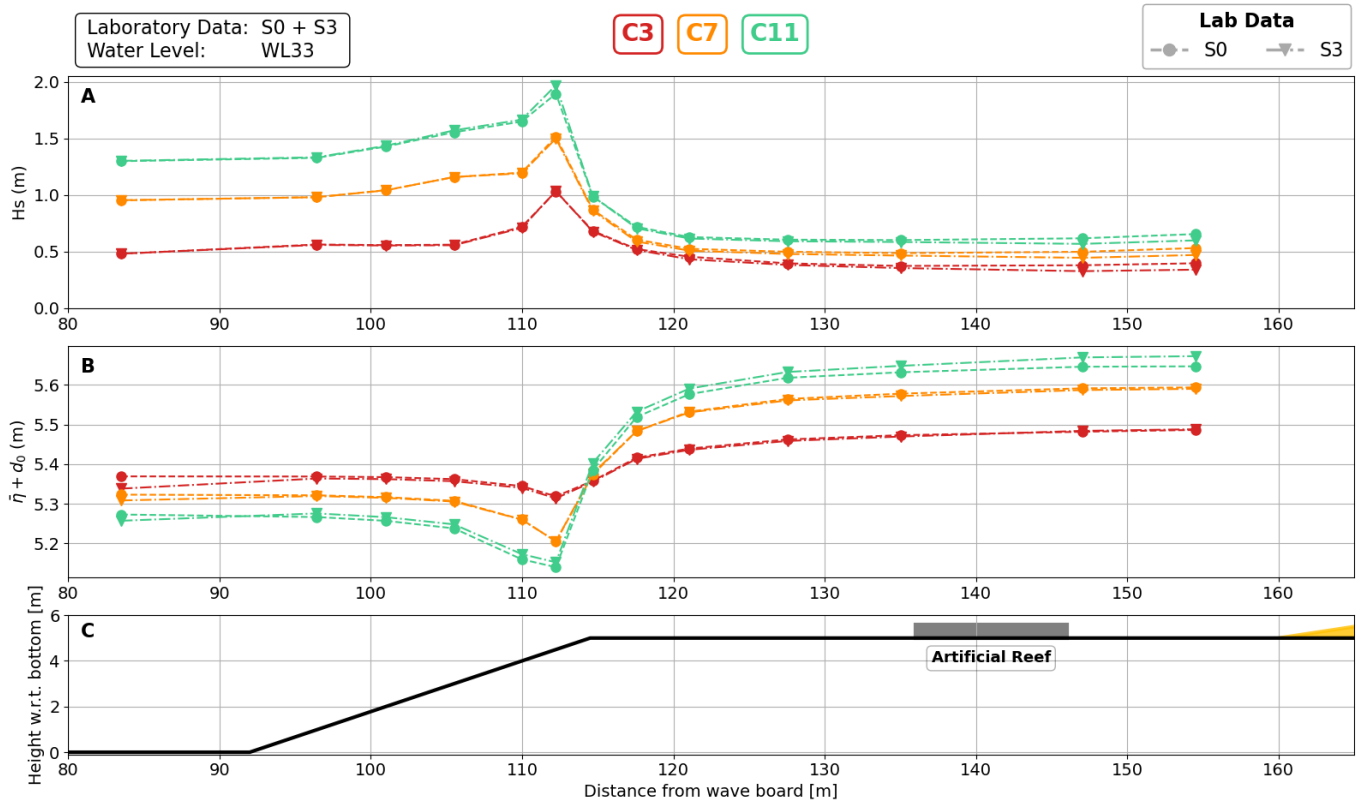

Figure 7.1: Transformation of the total (inc + ref) significant wave height H_S (**A**) and the height w.r.t. the bottom of the flume, including setup, over the reef (**B**) for the laboratory data, showing **WL33**. The artificial reef is located between x = 136 and 146 m (**C**).

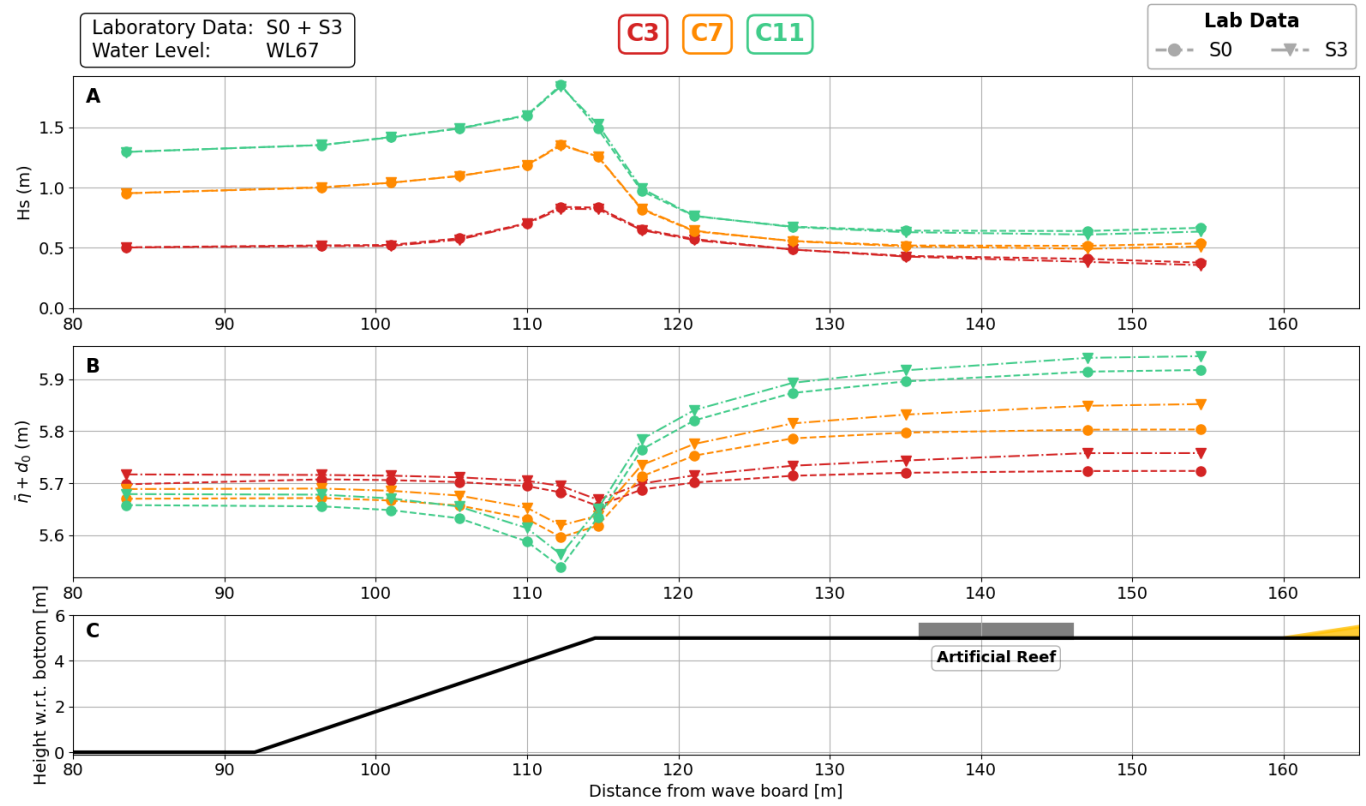

Figure 7.2: Transformation of the total (inc + ref) significant wave height H_S (**A**) and the height w.r.t. the bottom of the flume, including setup, over the reef (**B**) for the laboratory data, showing **WL67**.

Panel B of Figures 7.1 and 7.2 show the water level over the reef, including the setup η. To properly assess the differences in setup induced by the artificial reefs, it is essential for the offshore water levels to be consistent across all experimental runs. Unfortunately, this condition is not met. Consistent offshore water levels are necessary because the effectiveness of the reefs is linked to water depth, and variations in depth affect the observed results.

Despite these inconsistencies, the offshore water levels (x = 80 to x = 100 m) shown in Panel B for WL33 indicate that while the water levels differ between wave conditions C3, C7, and C11, they are nearly identical between S0 and S3. Moving onshore over the reef flat, the water level, now also including the setup, for wave conditions C3 and C7 remains the same between S0 and S3. For C11, a slight increase in setup is observed for S3, reaching approximately **0.02 m** at the shoreline.

For WL67 (Figure 7.2, Panel B), the water levels are less well aligned than for WL33. Across all three wave conditions, water levels over the entire domain for S3 are consistently a few centimetres higher than for S0. This means that the effectiveness of the artificial reef might be underestimated.

To provide a more quantitative analysis, Table 7.2 summarises the reduction in total wave height at the most onshore sensor (x = 155 m) for each wave condition and water level, expressed both as an absolute value and a percentage. Additionally, the table includes the differences in water level for both offshore and onshore regions. Offshore water levels, therefore having approximately no setup, are calculated as the mean of the two most offshore sensors (x = 83 m and x = 97 m), while onshore water levels, including setup, are the mean of the two most onshore sensors (x = 147 m and x = 155 m). Both water levels are shown to examine the influence of offshore water levels on the corresponding setup onshore.

Table 7.2 shows that both the absolute reduction in H_S and the percentage reduction are larger for WL33 compared to WL67. For WL33, the absolute reduction is similar across all three wave conditions. However, in relative terms, the most energetic condition (C11) exhibits the smallest reduction at 8.5%,

while the least energetic condition (C3) shows the largest reduction at 14.2%. In contrast, WL67 shows a slight increase in absolute reduction with more energetic conditions, though the differences are small. The percentage reduction remains consistent at approximately 5% across all three conditions.

The observed differences in water level and setup on the reef flat are influenced by the offshore variations in water level. For WL33, wave conditions C3 and C7 show minimal differences in both offshore and onshore water levels between the base case S0 and the artificial reef case S3. In contrast, wave condition C11 for WL33 shows a small increase in onshore setup of approximately 0.025 m, compared to negligible differences offshore. For WL67, the water level differences are more pronounced. Offshore, the water level for case S3 is approximately 0.02 m higher, increasing to nearly 0.05 m onshore for wave condition C7. This increased water level on the reef likely results in an underestimation of the effectiveness of the artificial reef for this higher water level.

Condition	Reduction H_s		Water Level Differences [m]	
	Absolute [m]	Percentage [%]	Offshore	Onshore (setup)
WL33C3	0.056	14.2	-0.014	0.002
WL33C7	0.061	11.5	-0.006	-0.004
WL33C11	0.056	8.5	0.001	0.025
WL67C3	0.020	5.3	0.012	0.034
WL67C7	0.026	4.8	0.019	0.047
WL67C11	0.031	4.7	0.022	0.027

Table 7.2: Absolute and percentage reductions of H_S between S0 and S3, per wave condition and water level at the location of the most onshore sensor (x = 155 m). Additionally, the water level differences both offshore and onshore are shown for the lab data between the base case S0 and the case S3.

It is also crucial to examine the transformation of the specific wave components, SS and IG, for cases S0 and S3. However, to avoid redundancy in the presented figures and information, this analysis is integrated into the comparison of the SWASH data with the laboratory results.

7.2. Comparison SWASH and Lab Data: S0 (base)

Before analysing the effectiveness of the artificial reef by comparing the SWASH data with the laboratory data, the transformation of the total significant wave height for the base case S0 is first examined. SWASH has been shown to accurately describe wave transformation over a bare reef with similar characteristics. Therefore, differences between SWASH and laboratory data for S0 are expected to be minimal. Figures 7.3 and 7.4 illustrate the transformation of total significant wave height and water level relative to the bottom of the flume, including setup, across the reef for the three distinct wave conditions, corresponding to WL33 and WL67, respectively. Notably, discrepancies between the numerical and laboratory data are observed, particularly in the shoaling, setup, and wave height over the reef flat.

The reef can be divided into three zones, each with distinct characteristics: the **offshore region** (x = 80 m to x = 100 m), the **surfzone** (x = 100 m to x = 115 m), and the **reef flat** (x = 115 m to the shoreline). The analysis of Figures 7.3 and 7.4 is conducted separately for these three zones.

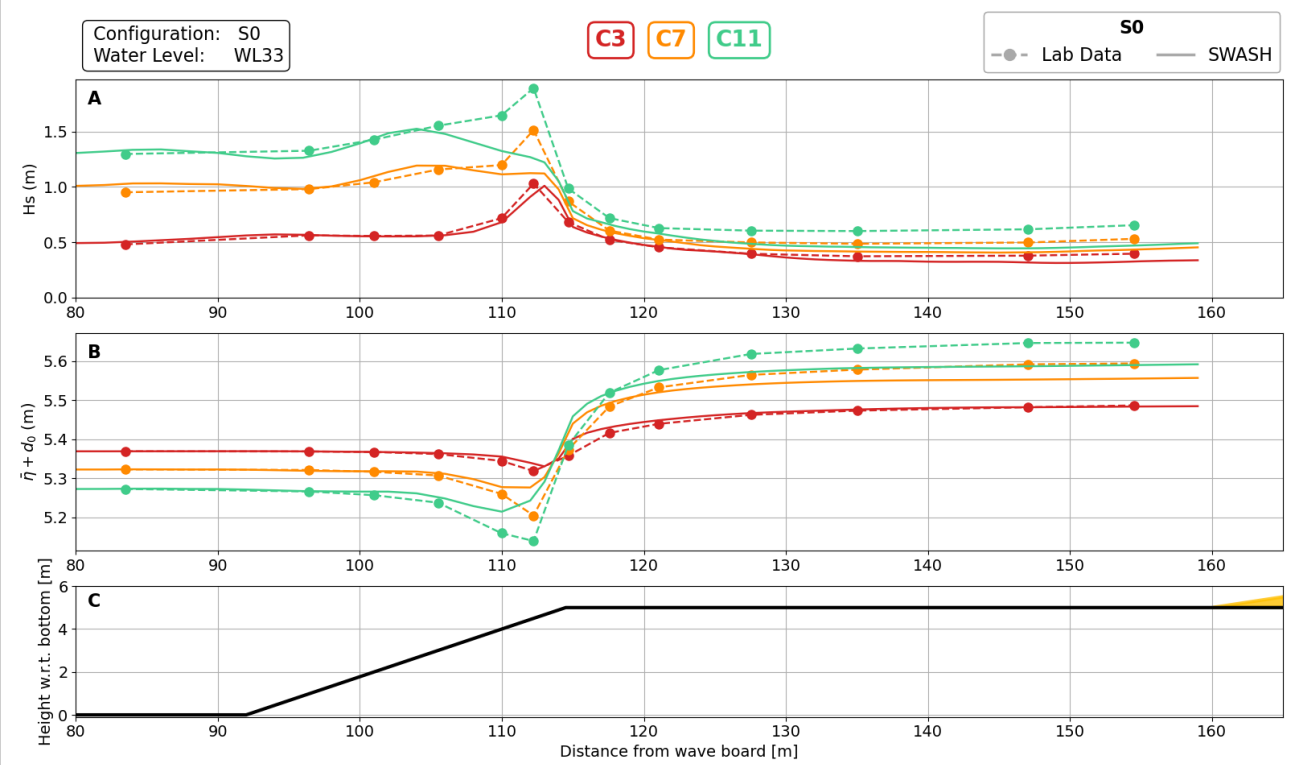

Figure 7.3: Transformation of the total significant wave height H_S and the height w.r.t. the bottom of the flume, including setup, over the reef showing the base case (**S0**) and **WL33**. The dashed lines show the lab data with the markers denoting the locations of the pressure sensors. The solid line denotes the numerical results.

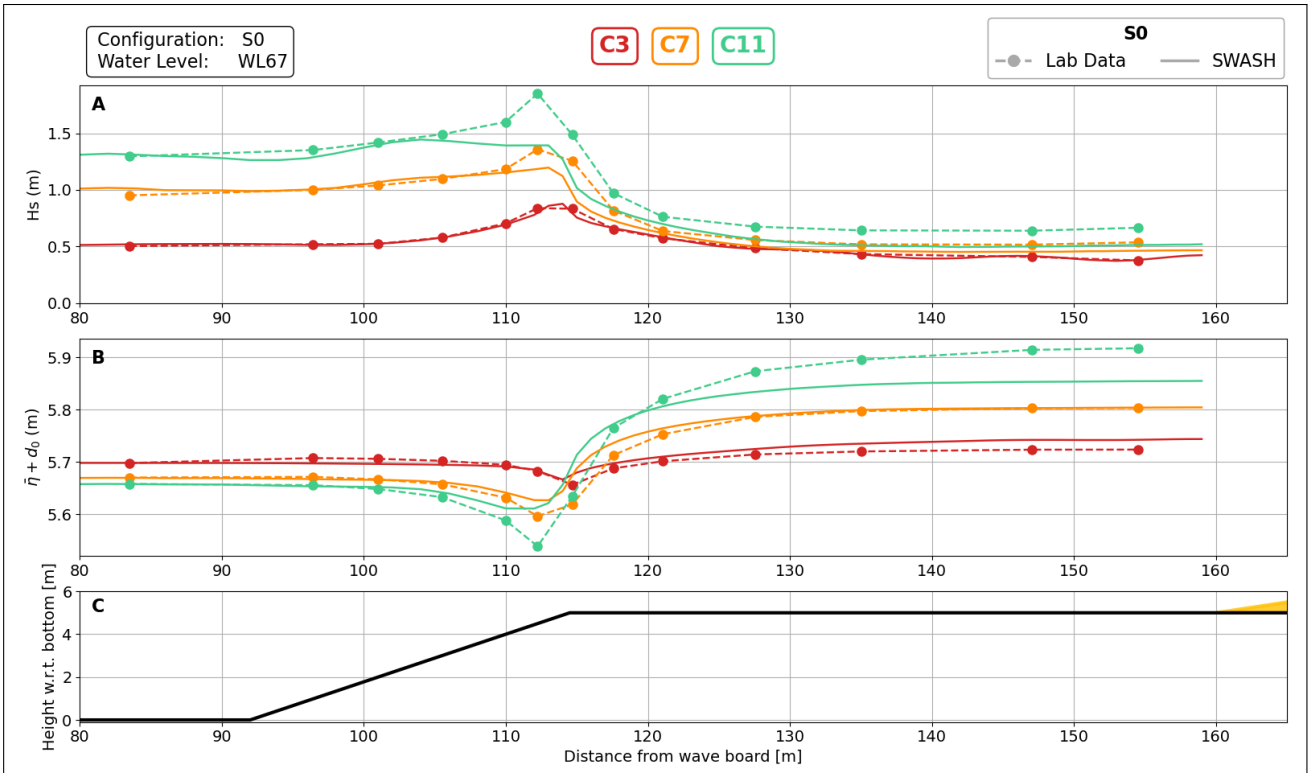

Figure 7.4: Transformation of the total significant wave height H_S and the height w.r.t. the bottom of the flume, including setup, over the reef showing the base case **(S0)** and **WL67**.

Offshore region: 80 - 100 m

The offshore significant wave height (H_S) presented in Panel A of Figures 7.3 and 7.4 shows that, for all wave conditions and water levels, the offshore significant wave height is nearly identical between the laboratory data and the SWASH simulations. Similarly, Panel B of the figures shows the offshore water level, which aligns perfectly between SWASH and the laboratory data. This outcome is expected, as the offshore water level for the SWASH simulations is calibrated to match the measurements at the most offshore sensor, located at x = 83 m.

Surfzone: 100 - 115 m

Clear differences between SWASH and the laboratory data can be observed in the surfzone. In Panel A of Figures 7.3 and 7.4, SWASH accurately predicts shoaling for wave condition C3 (depicted by the red line) for both water levels. However, for the more energetic conditions, C7 and C11, SWASH increasingly underestimates the shoaling and, consequently, the breaking wave height. This trend is consistent for both water levels.

These differences are also apparent in the water level in the surf zone, as shown in Panel B of the figures. For condition C3, the wave-induced set-down caused by shoaling aligns well between SWASH and the laboratory data. However, for the more energetic conditions (C7 and C11), SWASH progressively underestimates the set-down, which has consequences for the setup observed on the reef flat.

Reef flat: 115 - 160 m

The significant wave height and water level show notable discrepancies between the SWASH simulations and laboratory data, with SWASH consistently underpredicting the wave height on the reef flat compared to the laboratory results, particularly under more energetic wave conditions (C11). Table 7.3 shows both the numerical and percentage differences in wave height at the shoreline (x = 155 m) and the differences in setup across all wave conditions and water levels. A negative value indicates that SWASH is underpredicting the laboratory data. It is important to note that these differences are based on setup, which is referenced to the offshore water level rather than the total water level on the flat.

The table shows that the significant wave height H_S is consistently underestimated for all wave conditions, except for WL67C3 (the highest water level and least energetic condition). The most energetic condition (C11) shows the largest underestimation of wave height, both in absolute and percentage terms, with the lowest water level (WL33) showing the greatest underprediction.

In contrast, the differences in setup show a less distinct trend. For WL33, an increase in offshore wave height leads to a larger underestimation of the setup by SWASH, with condition C3 showing almost identical (minimal) setup between SWASH and the laboratory data. For WL67, condition C3 results in an overestimated setup. Although this overestimation is significant at nearly 74%, the setup difference is relatively small at only 2 centimetres. Conversely, the most energetic wave condition (C11) results in the largest underestimation of setup for WL67 at 24%.

Condition	Differences H_s		Differences setup [m]	
	Numerical [m]	Percentage [%]	Numerical [m]	Percentage [%]
WL33C3	-0.07	-17.3	-0.00	-2.3
WL33C7	-0.10	-18.0	-0.04	-14.3
WL33C11	-0.18	-27.8	-0.06	-15.3
WL67C3	0.010	2.5	0.02	73.5
WL67C7	-0.074	-13.8	0.00	0.5
WL67C11	-0.152	-22.8	-0.06	-24.3

Table 7.3: Differences in H_S and setup at the most onshore sensor (x = 155 m) between the numerical and laboratory results for configuration S0. Both a numerical value and a percentage value is displayed, with negative values indicating an underestimation by SWASH.

7.3. Influence of the Artificial Reef: Comparison S0 vs. S3

Section 7.1 demonstrated that the artificial reef in the laboratory experiments has a limited impact on reducing total wave height, while Section 7.2 compared the wave transformation for the base case (S0) between the SWASH model and laboratory results, revealing differences in both wave height and setup over the reef flat. This section further explores the comparison between the SWASH model and laboratory data, now regarding the effectiveness of the artificial reef (S3). To better understand the discrepancies in wave height on the reef flat, a more detailed analysis is performed, focusing on the transformation of wave height across the two distinct frequency bands, SS and IG. These bands are characterized by different hydrodynamic processes, providing a clearer scientific basis for interpreting the results.

Wave Height Transformation: SS and IG

Figure 7.5 shows the transformation of the total (incoming and reflected) sea/swell and infragravity wave components over the reef for wave condition C7 (H_s = 1.0 m, T_p = 5.77 s). The characteristics of the transformation for the other two wave conditions, C3 and C11, are similar to those of C7. Their respective transformations are presented in Appendix D, shown in Figures D.1 and D.2. Panel A in Figure 7.5 corresponds to the transformation at water level WL33, while Panel B depicts the transformation at water level WL67.

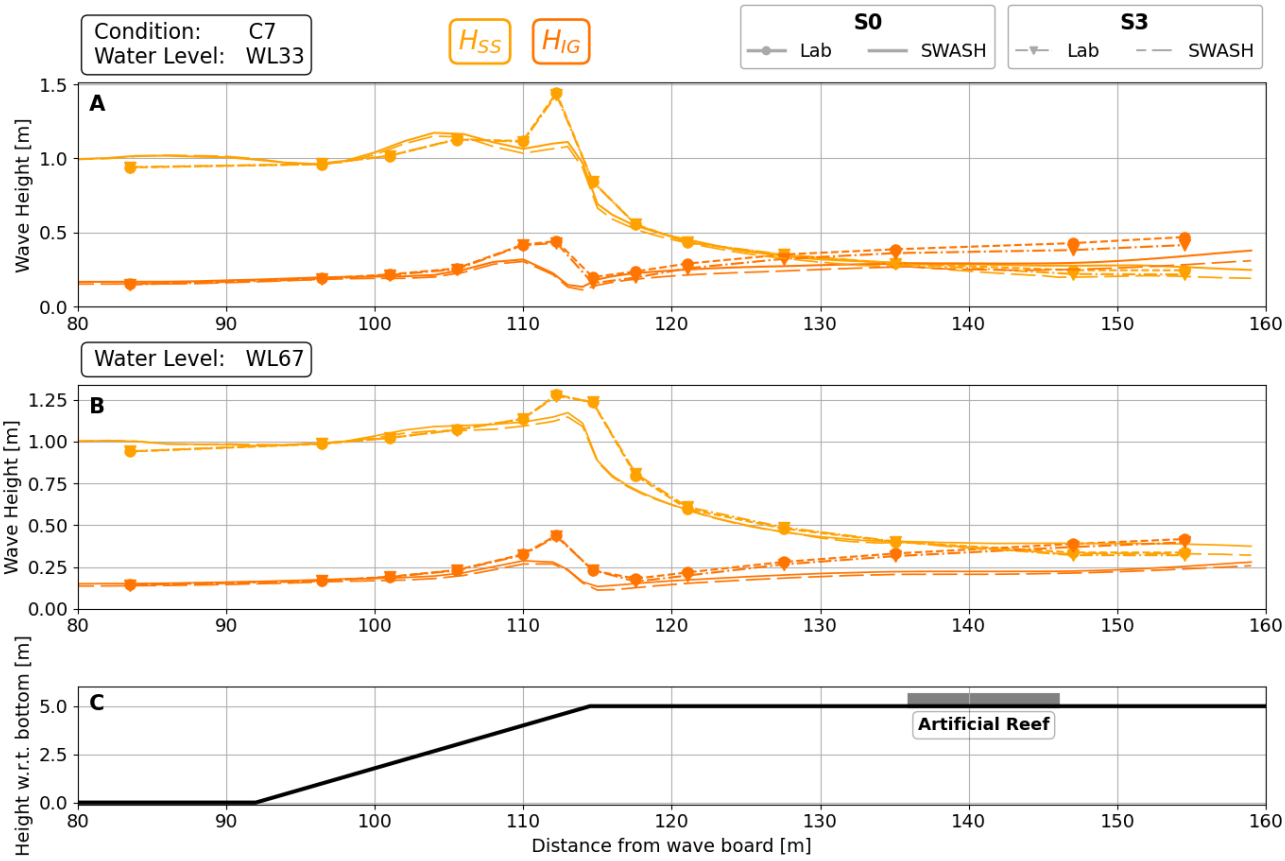

Figure 7.5: Transformation of the SS and IG wave heights H_{SS} and H_{iG} for both water levels for wave condition **C7** (H_s = 1.0 m, T_p = 5.77 s).

From x = 80 to x = 115 m in Figure 7.5, the differences between the base case (S0) and the case with an artificial reef (S3) are minimal when considering the laboratory and SWASH data separately. Offshore (x = 80 to x = 100 m), for both water levels (Panels A and B), SWASH and the laboratory results show similar wave heights for both the Sea/Swell (SS) and Infragravity (IG) components, with

SS waves being significantly larger than IG waves (1.0 m versus 0.15 m). In the surfzone (x = 100 to x = 115 m), SWASH underestimates shoaling for both SS and IG waves. However, at the reef crest (x = 115 to x = 120 m), the SS and IG wave heights in SWASH closely match the laboratory data. Beyond the reef crest, moving shoreward, discrepancies in wave heights become more pronounced.

For both water levels, SWASH accurately predicts the SS wave heights from the reef crest to the shoreline for both the S0 and S3 cases, with values of approximately 0.25 m for WL33 and 0.35 m for WL67. An increase in IG wave height is expected shoreward, driven by nonlinear processes that transfer SS energy to the IG wave band, along with breakpoint forcing. This increase is observed in both the SWASH and laboratory data; however, SWASH underestimates the magnitude of this change. Specifically, for WL33, laboratory data indicate an IG wave height of 0.45 m at the shoreline (x = 155 m), whereas SWASH predicts only 0.30 m. Similarly, for WL67, the laboratory data show 0.45 m, while SWASH predicts 0.25 m. While laboratory results show that IG wave height exceeds SS wave height at the shoreline for both water levels, SWASH shows a more limited increase in IG wave height, with IG wave heights remaining lower than SS wave heights at the shoreline.

A clear comparison between the S0 and S3 cases cannot be made from this figure, as the differences between them are too small. Therefore, an analysis of the reduction coefficient, R_c , is conducted, as described in Section 5.3. This coefficient is defined as the ratio H_{S3} / H_{S0}, representing the relative reduction in wave height due to the presence of the artificial reef.

Reduction Coefficient

Given the minimal differences between S0 and S3, an analysis into the reduction coefficient R_t is performed. This coefficient does not describe the absolute value of the wave heights, but shows the ratio in wave height between cases S3 and S0 (Figure 7.6 to 7.8). The figures not only show the reduction coefficient for the specific wave components H_{SS} (Figure 7.7) and H_{IG} (Figure 7.8), but also for the total wave height H_S (Figure 7.6).

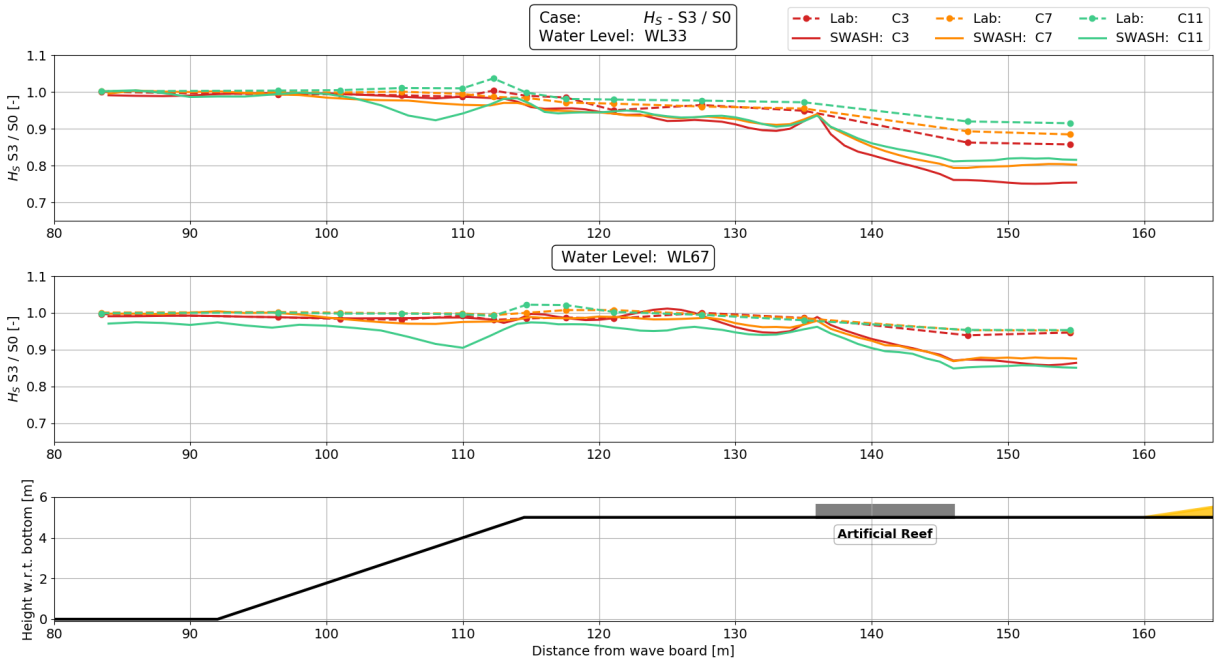

Figure 7.6: Reduction coefficient R_c showing the ratio of **total significant wave height** H_S for S3 / S0 for both water levels and all three wave conditions. For all cases, the SWASH model overestimates the reduction in wave height caused by the artificial reef.

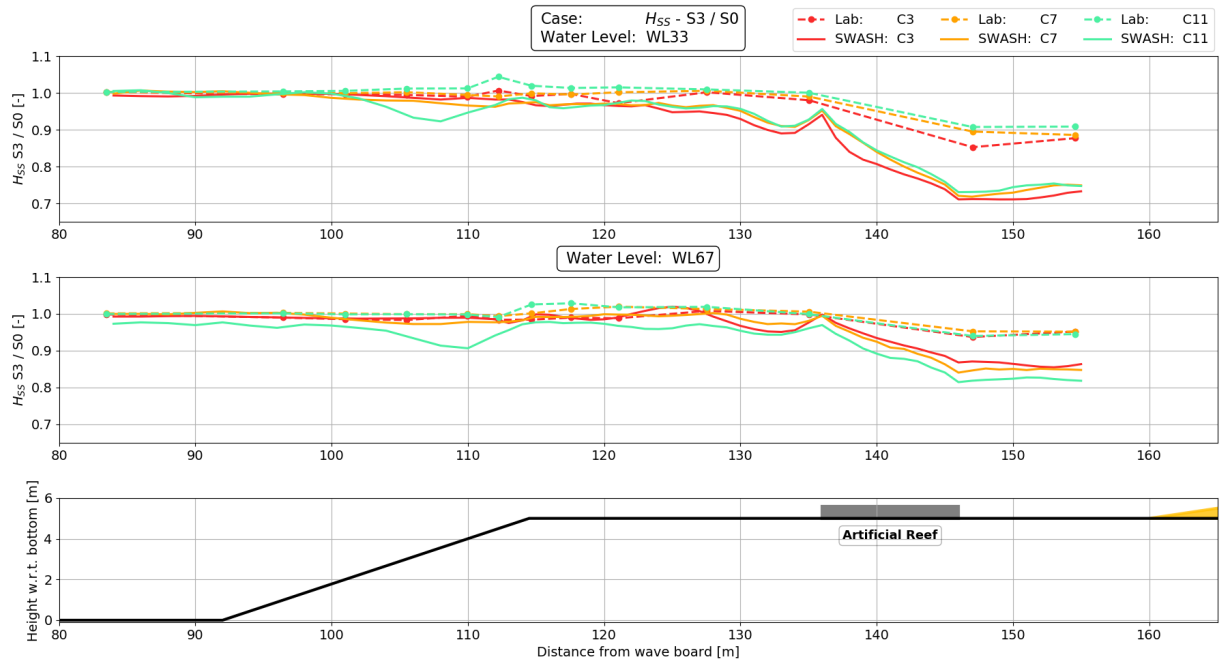

Figure 7.7: Reduction coefficient R_c showing the ratio of **total Sea/Swell wave height** H_{SS} for S3 / S0 for both water levels and all three wave conditions. Just as for total wave height, the SWASH model overestimates the reduction in wave height caused by the artificial reef.

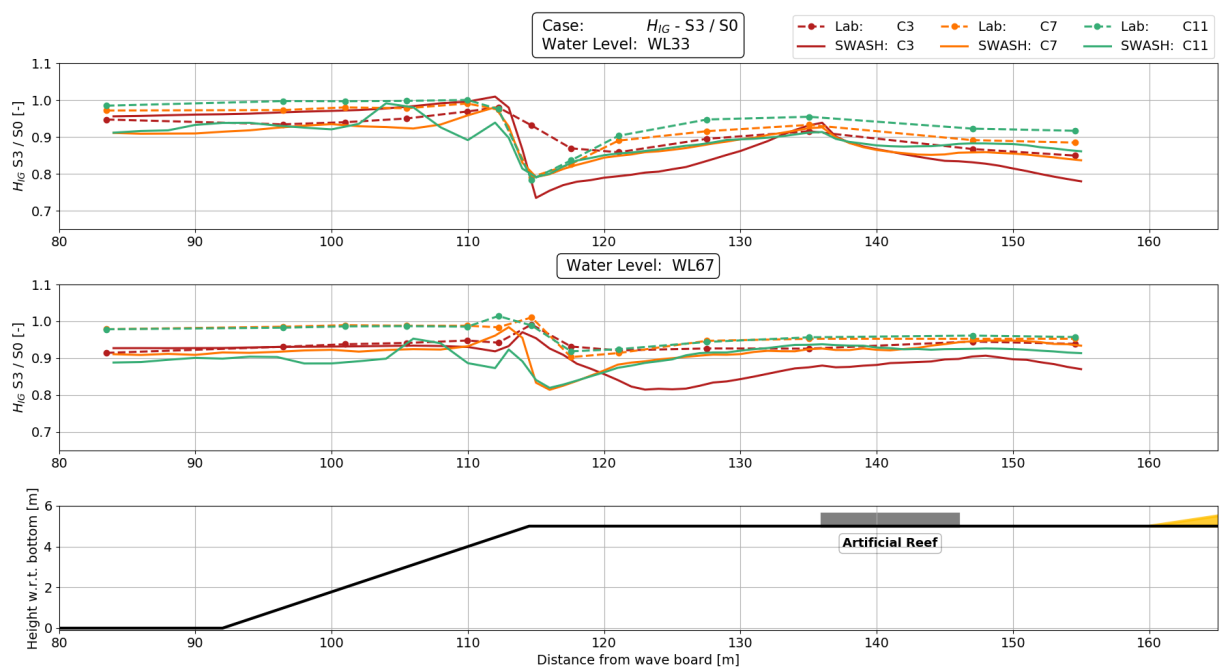

Figure 7.8: Reduction coefficient R_c showing the ratio of **total Infragravity wave height** H_{IG} for S3 / S0 for both water levels and all three wave conditions. While the laboratory data shows a comparable reduction in IG wave height compared to the total ans SS wave height, the SWASH data has difficulties accurately predicting the IG wave component.

The artificial reef is located between x = 136 m and x = 146 m. Since the total wave height (incoming and reflected) is shown, some differences offshore of the restoration are expected, although minimal. The laboratory data shows a reduction coefficient of around 1 in this area, which is both expected and

desired. However, SWASH struggles to accurately predict conditions in the shoaling zone (x around 110 m), particularly for the IG wave component (Figure 7.8). From the figures, it is clear that SWASH overestimates wave attenuation at the closest sensor to the shoreline (x = 155 m) for all conditions and water levels.

For the total significant wave height shown in Figure 7.6, at WL33, both SWASH and the laboratory data show that wave height reduction is smaller for the more energetic condition (C11) compared to the less energetic one (C3). However, SWASH predicts a reduction coefficient (R_c) of around 0.8, while laboratory data shows a reduction of 0.9. For WL67, the reduction coefficients are more similar across all wave conditions, with SWASH predicting R_c = 0.85 and the laboratory data 0.95, indicating less reduction at WL67 than at WL33.

A similar trend is observed for the SS component in Figure 7.7, with a greater reduction in SS wave height compared to the total significant wave height. For WL33, the laboratory data show an R_c of 0.9, whereas SWASH predicts a lower value of 0.75. For WL67, the laboratory data indicate an R_c of 0.95, while SWASH predicts 0.85. Drawing reliable conclusions from the R_c of the IG waves (Figure 7.8) is challenging for the SWASH data. While the laboratory data show similar trends to those for SS and total wave height, with lower reduction for more energetic conditions at WL33 and a consistent reduction rate of around 0.95 at WL67, SWASH struggles to predict IG wave attenuation, particularly in the surfzone.

To assess the extent of the difference between SWASH and the laboratory data, Table 7.4 presents the percentage reduction at the shoreline (x = 155 m) for all cases and wave components. For the lower water level (WL33), both SWASH and the laboratory data show a reduction in effectiveness as the wave conditions become more energetic. In contrast, for the higher water level (WL67), the reduction in effectiveness remains consistent across wave conditions. However, while SWASH shows a frequency dependence, with SS waves experiencing greater attenuation than IG waves, the laboratory data shows a more similar reduction for both wave components, around 11% for WL33 and 5% for WL67. In general, SWASH tends to overestimate the reduction, particularly for the SS component, with the overestimation being roughly a factor of two to three.

Case	H_s		H_{SS}		H_{IG}	
	Lab	**SWASH**	**Lab**	**SWASH**	**Lab**	**SWASH**
WL33C3	14.2%	24.6%	12.2%	26.7%	15.0%	22.0%
WL33C7	11.5%	19.7%	11.4%	25.1%	11.5%	16.3%
WL33C11	8.5%	18.4%	9.1%	25.3%	8.3%	13.9%
Average	11.4%	20.9%	10.9%	25.7%	11.6%	17.4%
WL67C3	5.3%	13.6%	4.8%	13.6%	6.1%	13.0%
WL67C7	4.8%	12.4%	4.8%	15.2%	4.7%	6.6%
WL67C11	4.7%	14.9%	5.5%	18.2%	4.2%	8.6%
Average	4.9%	13.6%	5.0%	15.7%	5.0%	9.4%

Table 7.4: Percentage reductions per wave condition, water level and wave component at the location of the most onshore sensor (x = 155 m). For all cases the laboratory data shows a lower reduction compared to the numerical simulations.

Differences in Variance Density Spectra

Given the significant difference between the laboratory data and the numerical data for the infragravity wave height on the reef flat, an investigation into the energy density spectra is performed. Figures 7.9 and 7.10 display the energy density spectra for wave condition C7 and the two water levels, respectively, showing both the numerical results from SWASH and the laboratory data at four different locations,

including the peak frequency f_{peak} at each location. Again, only wave condition C7 is shown, since the characteristics of the spectra observed for condition C3 and C11 are similar to C7. The energy density spectra for these conditions can be found in Appendix D in Figures D.3 to D.6.

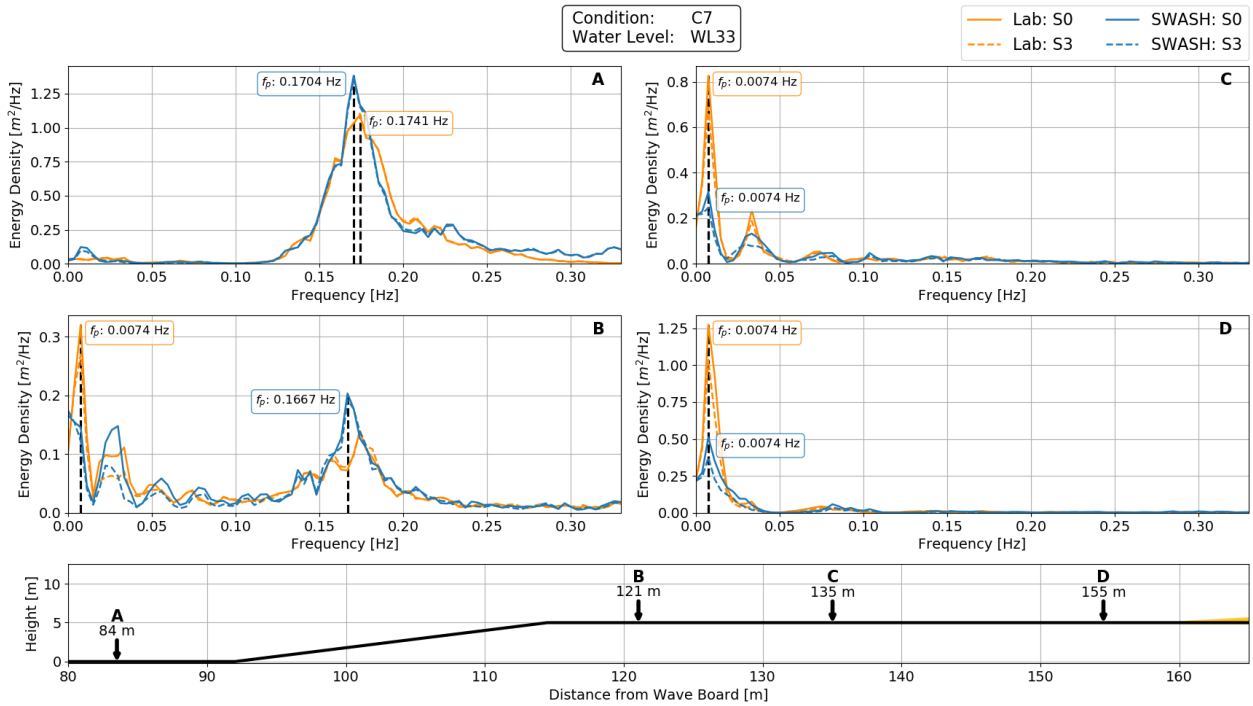

Figure 7.9: Energy density spectra at several locations on the reef flat for wave condition **C7** at **WL33**. Location A is positioned offshore, while Location B, C and D are positioned on the reef flat, with location D onshore of the artificial reef. Additionally, the peak periods f_{peak} are displayed for each location.

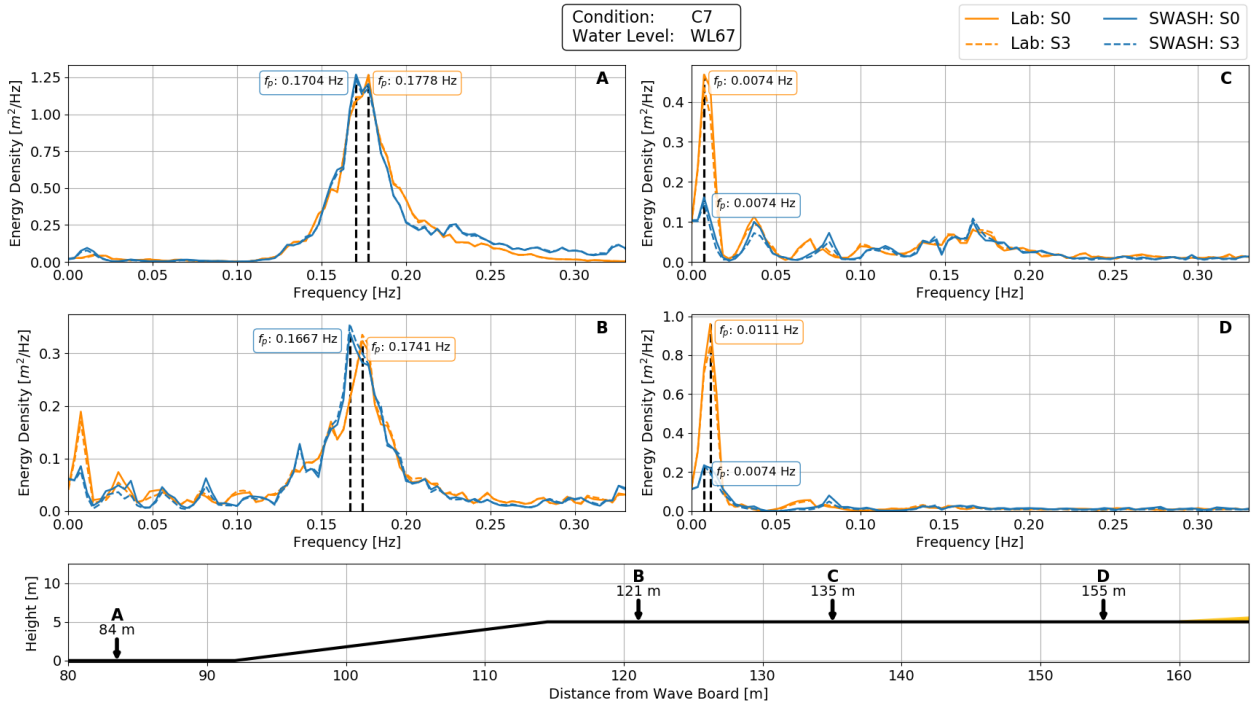

Figure 7.10: Energy density spectra at several locations on the reef flat for wave condition **C7** at **WL67**.

For both water levels and at all four locations, the higher frequency (SS) components (>0.05 Hz) appear to correspond well between SWASH and the laboratory data. The most offshore location (location **A**) is expected to show minimal differences between the datasets. However, since the total energy spectrum is presented, which includes both incoming and reflected signals, some minor discrepancies are anticipated. Overall, both the offshore peak frequency (location **A**) and the magnitude of the spectra align closely. A small peak in the SWASH data at very low frequencies (<0.02 Hz) is noticeable, which is not present in the laboratory data.

When moving further onshore, (location, **B**, **C**, and **D**) notable differences can be seen. While the higher frequency components still overlap reasonably well, the laboratory data exhibits a distinct and strong low-frequency energy peak, occurring at approximately 0.0074 Hz (135 s) of which the magnitude grows shoreward (from location **B** to location **D**). Although the magnitudes of these specific frequencies differ significantly between SWASH and the lab data, the peak frequency values are similar. This significant peak could be a result of resonance processes over the reef flat and is further investigated in the discussion section of this thesis. The differences between S0 and S3 are small, and the figures only show a minimal distinction between them.

7.4. Assessing Model Fit

An analysis is performed to assess how accurately SWASH predicts the laboratory data. Although there will be differences in the time series between the datasets, their energy density spectra should be the same, making these spectra useful for evaluating the goodness of fit.

R-squared

For each of the 14 pressure sensors along the transect, an R-squared analysis is performed on the energy density spectra, which include all three wave conditions, two water levels, and two configurations. Additionally, the R-squared for the specific frequency bands (IG and SS) is computed.

The R-squared values for configurations S0 and S3 independently are shown at each sensor in Figure 7.11. The SS wave band and the total energy density spectrum both show high R-squared values (>0.95) offshore. The IG wave band shows very low R-squared values offshore, however the p-value is larger than 0.05 and therefore the presented values are not statistically significant. Closer to the shore, the R-squared values decrease significantly, with the total spectrum lowering to around 0.75 and the SS gradually decreasing to 0.6. The IG component shows values between 0.6 and 0.8 on the reef flat. The difference between S0 and S3 is marginal for all components and sensors.

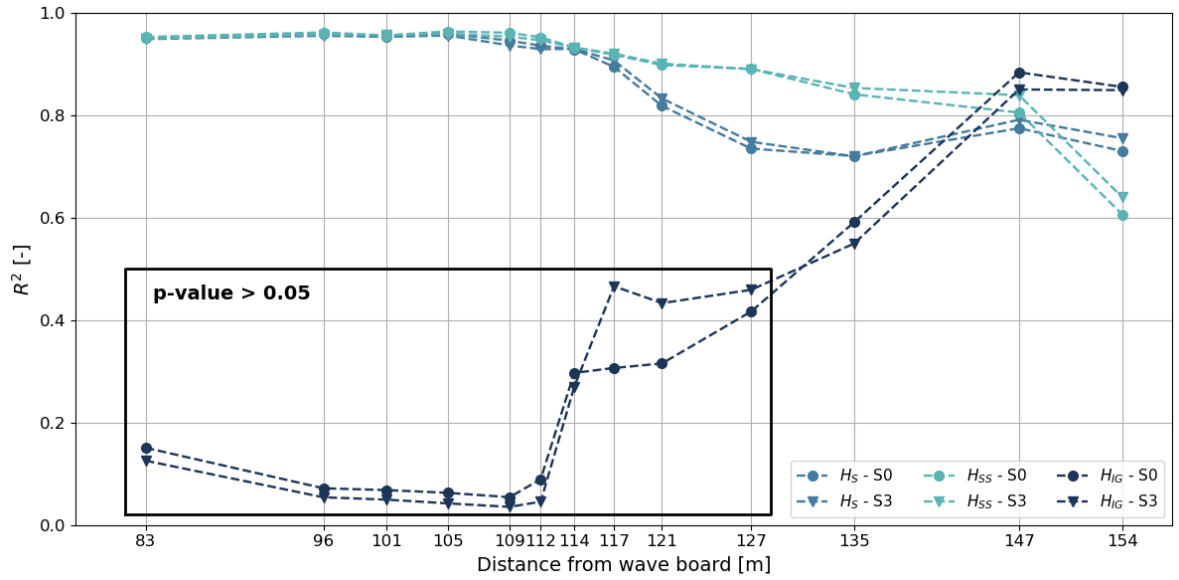

Figure 7.11: R-squared value indicating the correlation between the energy spectra of the numerical and laboratory data at each sensor. In general, the correlation on the reef flat is lower than offshore, with the IG frequency band not showing a statistically significant correlation for the offshore sensors.

Table 7.5 shows the R-squared for each component and condition, averaged both over the entire domain and specifically over the reef flat. It shows that the correlation is largely independent of water level. The results also indicate that SWASH most accurately predicts the SS waves, both offshore as well as on the reef flat. Additionally, while for the IG waves, the R-squared values are relatively high for the most onshore sensor, the overall correlation for IG waves is poor on average.

Case	H_s		H_{SS}		H_{IG}	
	Total	**Reef flat**	**Total**	**Reef flat**	**Total**	**Reef flat**
WL33C3	0.85	0.75	0.92	0.90	0.20	0.39
WL33C7	0.90	0.84	0.89	0.81	0.34	0.66
WL33C11	0.86	0.78	0.87	0.78	0.30	0.61
Average	0.87	0.79	0.89	0.83	0.28	0.55
WL67C3	0.84	0.72	0.91	0.86	0.29	0.46
WL67C7	0.90	0.81	0.91	0.83	0.40	0.60
WL67C11	0.87	0.77	0.88	0.78	0.39	0.65
Average	0.87	0.77	0.90	0.82	0.36	0.57

Table 7.5: R-squared for the three frequency bands for each wave condition and water level. A distinction is made between the correlation over the total domain and specifically on the reef flat, which in general is lower than for the complete domain.

Root Mean Square Error

Besides evaluating the correlation between the model and the laboratory data, a measure of the difference in magnitude between the measured and predicted wave height is assessed using the Root Mean Square Error (RMSE). Figure 7.12 shows the average RMSE in wave height for each sensor, for the total wave height H_S, the SS wave height H_{SS}, and the IG waves H_{IG}.

Offshore, the RMSE is below 0.05 m until it reaches the surfzone, where it peaks around the reef crest at approximately 0.40 m for the total wave height. Given that the average offshore wave height is around 1.00 m, the RMSE is less than 5% of the total wave height. However, in the surf zone, the total wave height ranges from 0.2 m for the infragravity waves up to 1.4 m for the total wave height. This results in an RMSE between 30% and 50% of the total height, which is quite significant.

Further onshore the RMSE increases to 0.15 m for the IG waves, while it remains below 0.05 m for the SS waves. Onshore the IG waves are of order 0.4 m, while the SS waves are 0.3 m in magnitude. Therefore, the RMSE error is relatively low for the SS waves (less than 10%), but reaches up to 40% for the infragravity waves.

It's important to note that the RMSE does not directly represent the mean error, as it involves squaring the errors and then taking the square root, which gives a larger weight to larger errors. However, it still gives an accurate magnitude of the error in the model.

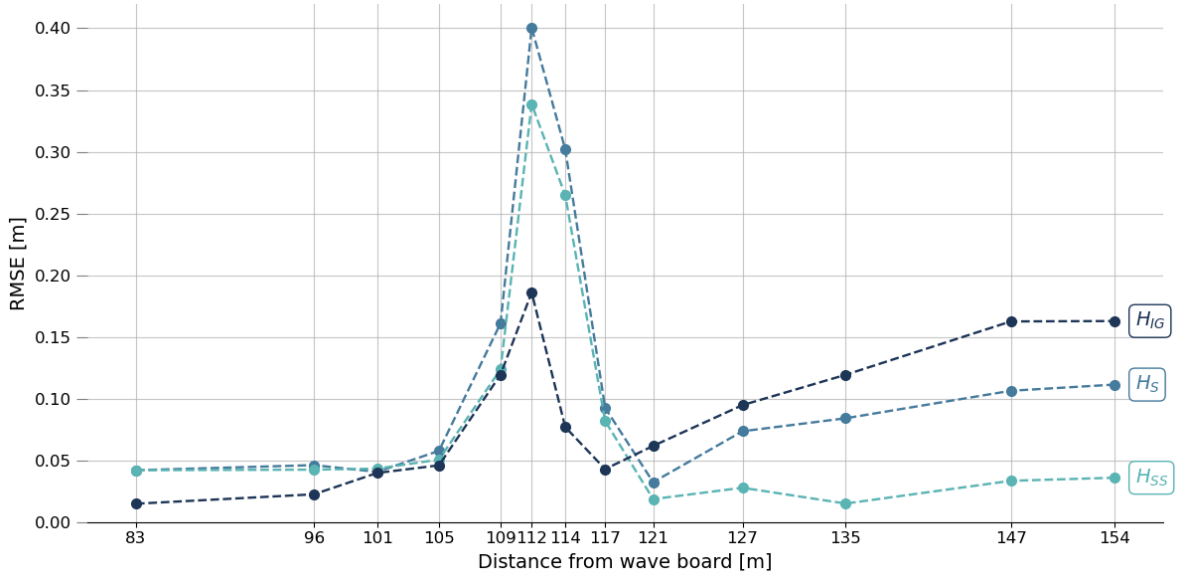

Figure 7.12: RMSE for the wave height at each sensor, showing a large error in the surfzone reaching a magnitude of 0.4 m. The SWASH model additionally shows a large error for the IF waves on the reef flat of 0.15m.

Bias

While the RMSE gives an indication of the magnitude of the error, it does not indicate whether the model is over-predicting or under-predicting the data. Therefore Figure 7.13 shows the bias for each sensor. A positive value indicates that the model is underpredicting while a negative value means that it is overpredicting. As can be seen from the figure, in general, the model is underpredicting the data, which is most significant for the surf zone at 0.3 m for the total significant wave height and 0.15 m for the IG waves (around 50% of total wave height). Also the infragravity waves are severely underestimated on the reef flat by 0.15 m (40% of total IG wave height) while the sea/swell waves are slightly overestimated by 0.03 m (<10%).

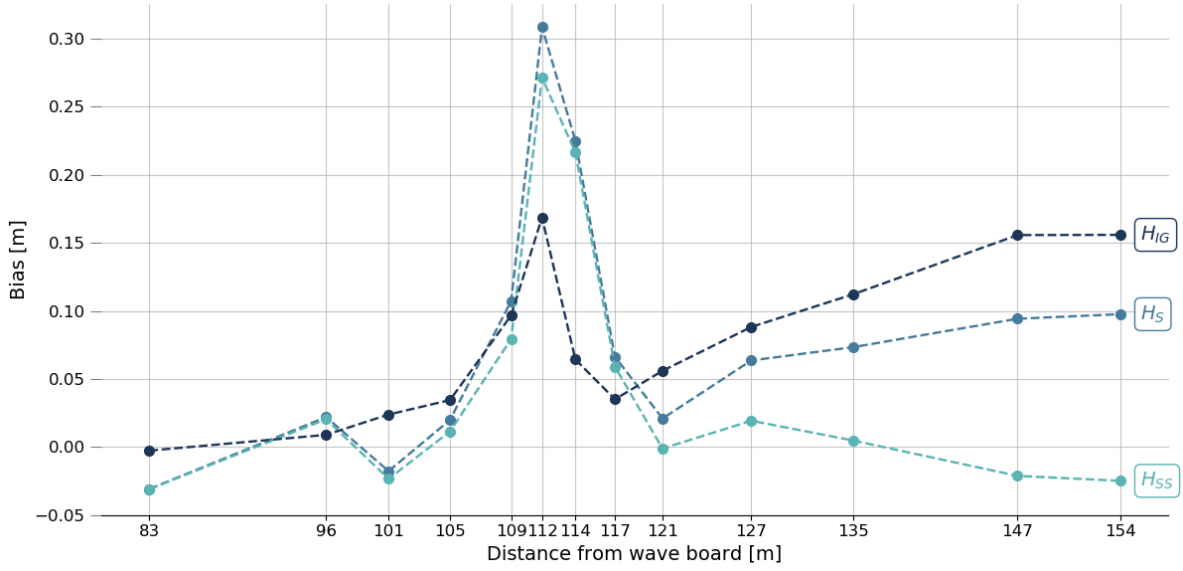

Figure 7.13: Bias in wave height at each sensor, showing an underprediction of the wave height in the surfzone of up to 0.30 m and of the IG wave of 0.15 m on the reef flat. The SS waves are slightly overpredicted on the flat, but the magnitude is minimal.

8

Discussion

In Chapter 4, the design of the artificial reef structures is discussed, concluding with an answer to the first research question. This chapter examines the limitations of the data analysis techniques, the numerical modelling approach, and the laboratory experiments. Additionally, the results are explored in greater detail and compared with findings from existing literature.

8.1. Stability of Artificial Reef Structures

The artificial reef structures were constructed by Coastruction using their state-of-the-art powder-bed 3D printer, capable of creating complex elements. However, limitations in the printing process lead to variations in weight of up to 10%, meaning that the actual porosities could be different from the porosity values used for the numerical analysis. Additionally, the differences in the individual elements resulted in different frontal and planform areas, which influences the accuracy and reliability of the stability analysis.

Although stability was not the primary focus of this thesis, a stability analysis was performed using empirical coefficients found in literature. However, these coefficients are often calibrated for structures located in deeper water (Düzbastilar, 2009; Woo et al., 2014; Tomasicchio et al. 2009). Limited research is specifically addressed to individual elements in shallow water with minimal submergence depth.

Nevertheless, a MSc thesis by Speth (2023) examined similar structures produced by Coastruction in a laboratory setting with similar characteristics, although at smaller scale. Her study did not include a stability analysis, yet the elements remained stable during testing without additional safety precautions. A short analysis is performed using the same empirical coefficients as those applied in this thesis, aiming to determine whether her elements would theoretically be stable under the tested conditions.

Speth provided all necessary data on the properties of the elements, water depth, spectral period (T_{m-10}), and wave height. Her elements weighed 5 kg, but under the most energetic wave conditions, a weight of 7 kg would have been necessary, excluding the 1.2 safety factor applied in this thesis. Therefore, the empirical coefficients might be overly conservative for such cases. Although stability was not a main concern in this thesis, these findings indicate the importance of conducting stability analyses due to the large uncertainty in empirical coefficients.

8.2. Data Analysis Techniques

Besides limitations in the modelling approach, limitations in the techniques used to analyse the data can negatively impact the accuracy of the results.

A substantial part of the analysis of the numerical data focused on the incoming wave height transformation, acquired by separating the wave field into an incoming and an outgoing component using the Guza wave split method. Since shallow water conditions cannot be assumed across the entire

domain, wave celerity is not solely a function of the water depth. Therefore, a more complex version of the Guza split method was used, which requires the computation to be made in Fourier space. As a consequence, energy at twice the frequency of interest was neglected. However, most energy is concentrated either at the low frequency or at the offshore peak frequency, therefore the effect of this limitation is expected to be minimal.

While assessing and quantifying this effect is difficult, an attempt is made by computing the decomposition for the simplified case of shallow water conditions. For the infragravity (IG) waves, which can be assumed to be in shallow water, both versions of the Guza split method should produce the same decomposed wave field. Figure 8.1 shows the incoming and outgoing significant IG wave height over the domain for wave condition C7 (H_S = 1.0 m, T_p = 5.77 s) at water level WL33.

The results show nearly, however not fully, identical wave heights on the reef flat (x > 115 m) and offshore (x < 100 m), while a clear difference can be seen in the surfzone (x = 100 to 115 m). Due to the complex processes in this zone, it is difficult to assess which method more accurately describes this area. However, the minor differences on the reef flat, where shallow water conditions certainly prevail for the IG waves, suggests that performing the Guza split in Fourier space can indeed underestimate the wave energy, although very slightly. Unfortunately, a similar assessment cannot be made for the sea/swell waves.

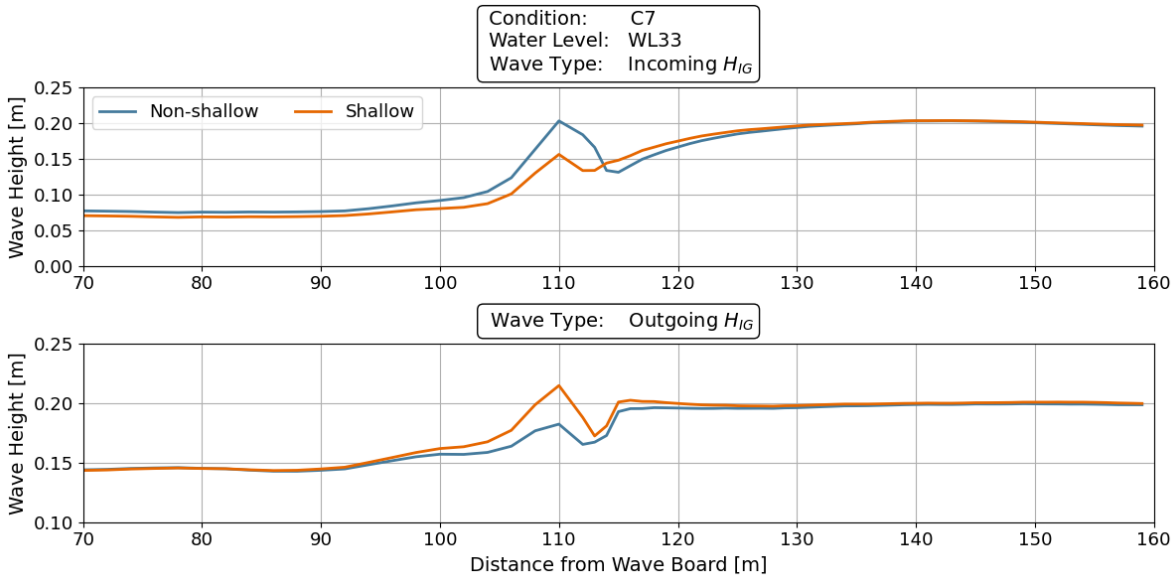

Figure 8.1: Comparison between the different versions of the Guza split method, in which either shallow water is assumed (orange) or not (blue/grey). The figure shows both the incoming and outgoing component of the IG waves for wave condition C7 and water level WL33.

8.3. Numerical Modelling Approach

The SWASH model was used for the numerical simulations, in which the artificial reef was modelled as a porous medium. The SWASH simulations showed, for the more energetic wave conditions, an underestimation of the shoaling, leading to a reduced setup over the flat compared to the laboratory results. Additionally, SWASH overpredicts the effectiveness of the artificial reefs. Here the limitations of the modelling approach are investigated and discussed. The results are compared to relevant literature, and the parameter selection for the model is discussed.

Additionally the results of the optimisation part of this thesis are discussed and compared to existing literature, focussing on the observed differences for the tested locations as well as the magnitude of the effect of the artificial reefs.

8.3.1. Shoaling and Wave-Induced Setup

While SWASH allows for adjusting the breaker parameter to increase the steepness at which waves break, the high vertical resolution used in these experiments did not require this adjustment (Smit et al., 2013). Despite this, the model underestimated shoaling, which subsequently led to an underestimation of wave breaking and a lower setup on the reef flat under highly energetic conditions (H_S = 1.3 m, Condition C11). Therefore, it is worthwhile to evaluate the performance of other studies in predicting shoaling under similar experimental conditions.

Several studies have calibrated numerical models based on the laboratory experiments of Demirbilek and Nwogu (2007), which measured wave height and water levels over a fringing reef. These experiments had similar characteristics to the CREST experiments but featured a less steep fore-reef slope and employed fewer sensors in the surfzone. As a result, the sharp peaks in wave height observed in the surfzone during the CREST experiments may not have been captured. However, the setup observed on the reef flat should still be accurately represented.

Buckley et al. (2014) calibrated a single-layer SWASH model and the Surfbeat version of XBeach using the dataset of Demirbilek and Nwogu (2007). They found that both models accurately predicted the setup over the reef flat, even under highly energetic wave conditions. Similarly, Pearson et al. (2017) compared the XBeach Non-Hydrostatic (XBNH) model to the results of Demirbilek and Nwogu (2007). While Pearson found that the setup was not accurately predicted for some wave conditions, it was accurately predicted for the conditions similar to those in the CREST experiments (condition C11).

However, Lashley et al. (2018), who also calibrated the XBNH model on the same dataset, found that while wave heights were well captured, the model underestimated the setup over the reef flat for highly energetic conditions like C11. Lashley also calibrated the XBNH model using experiments of Buckley et al. (2015), which featured a fore-reef slope of 1:5, similar to that of the CREST experiments. In these cases, the setup was consistently underestimated under more energetic conditions. Furthermore, the results of Lashley showed that while, in the experiments, a sharp peak in H_{m0} was observed in the surfzone, the model failed to capture it.

Additional research has evaluated the performance of numerical models in simulating wave dynamics over fringing reefs. Fang et al. (2014) found that their Boussinesq model generally underestimated wave setup on the reef flat, particularly under conditions involving highly nonlinear waves. Similarly, Yao et al. (2012) tested a fully nonlinear Boussinesq model on multiple laboratory experiments, including those from Demirbilek and Nwogu (2007). While the model showed good agreement with the measured results from this dataset, it struggled to predict setup accurately on steeper reef profiles, especially those with a slope steeper than 1:6, such as the reef tested for the CREST experiments.

8.3.2. Porous Medium Flow Resistance

SWASH overpredicts the effectiveness of the artificial reef, i.e. wave height reduction, by approximately a factor of 2. However, resistance forces within the porous medium depend on the parameters α and β, which are related to the laminar and turbulent friction loss, respectively. These parameters depend heavily on the flow conditions and the specific shape of the elements. As discussed in Section 4.4, the hydrodynamic conditions in this study fall outside the range for which Van Gent (1995) developed and calibrated his model and parameters. Van Gent developed his model based on submerged breakwaters, where the dimensions of the individual rocks were notably smaller compared to the elements used in the CREST experiment. Additionally, the porosity of the submerged breakwaters was significantly lower than that of the artificial reef used here.

For this study, values of $\alpha = 200$ and $\beta = 1.1$ were use, based on proposed values by Qu et al. (2024), Hsu et al., (2002), Van Gent (1995), and Losada et al. (2008). However, these values clearly need further calibration, as the model currently overestimates wave attenuation significantly. It is recommended to consider different parameter values such as those employed by Yao et al. (2022), who used $\alpha = 500$ and $\beta = 2$, as well as even lower values as found by Mellink et al. (2014). An initial attempt at calibrating the data is performed for multiple sets of dimensional parameters:

- Case 1 (base): α = 200 and β = 1.1
- Case 2: α = 200 and β = 0.8
- Case 3: α = 200 and β = 2
- Case 4: α = 500 and β = 2

The results are illustrated in Figure 8.2 and show the effect of a change in both α and β. The analysis focuses solely on the sea/swell (SS) component of the wave field, since SWASH accurately predicts these waves, whereas infragravity waves are heavily underpredicted. From the figures it becomes clear that changing the value for α has no effect, since the turbulent forces, which scale with the square of the velocities, are dominant. Increasing β to 2 shows a significant increase in wave height reduction, while lowering the value to 0.8 shows a decrease. A value for β of 0.8 is a lower bound value as found in literature, yet the reduction in wave height is still overestimated by the SWASH model.

The overestimation of wave height reduction in the SS band may partly be explained by the underprediction of the infragravity wave heights in the SWASH model. Infragravity waves introduce a periodic, slowly varying water level over the reef flat. As the effectiveness of the artificial reef is non-linearly influenced by water depth, differences in infragravity wave height between the SWASH model and laboratory observations may affect the overall wave height reduction. The underestimated infragravity wave heights in SWASH could therefore contribute to the overestimation of wave reduction by the artificial reef.

Another important factor is the porous media approach, for which, as previously noted, the conditions in this study fall outside the range for which Van Gent (1995) developed and calibrated his model. Consequently, Van Gent's porous medium model may not be suitable for this specific relatively porous artificial reef structure, which consists of relatively large individual elements

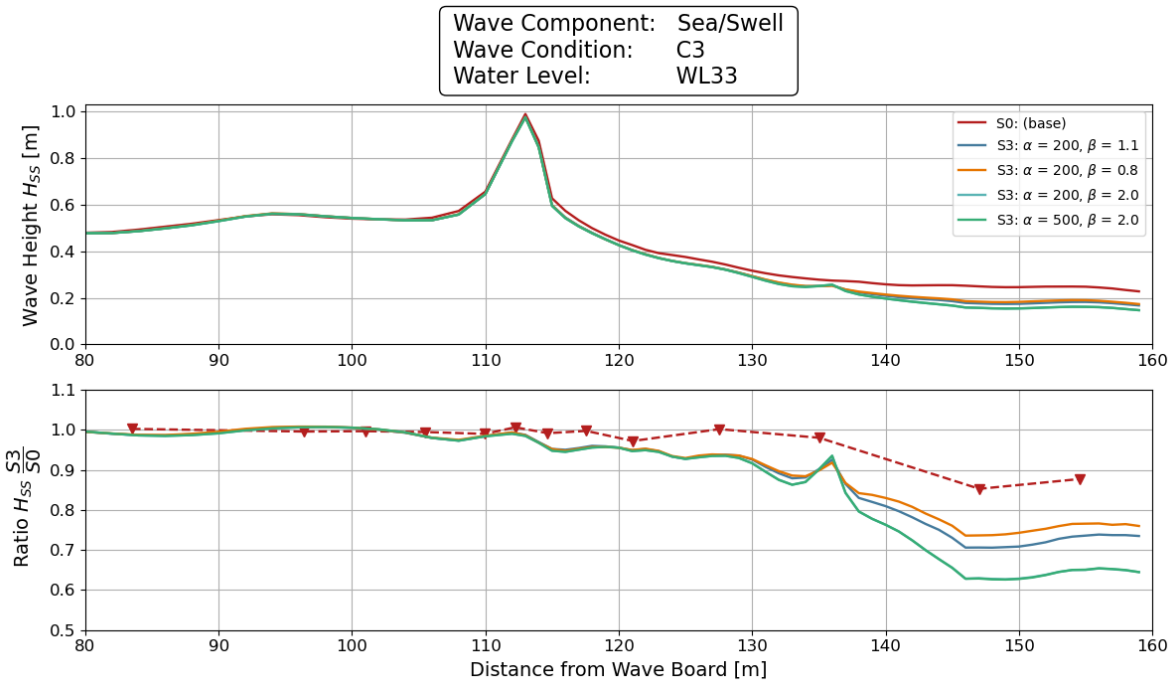

Figure 8.2: Sea/swell wave height transformation over the domain for different sets of coefficients α and β with in the top figure the total sea/swell wave height H_{SS} and the bottom the transmission coefficient depicting the ratio in wave height for S3 over S0.

8.3.3. Differences for Restoration Location

The differences observed in wave height reduction by the artificial reefs placed at the three distinct locations on the reef flat can be compared with findings of Roelvink et al. (2021). Roelvink showed that

the location of an artificial reef on a fringing reef flat influences its effectiveness in reducing runup height. Her research evaluated this effectiveness mainly based on runup height; however, information on total wave height, including the infragravity and sea/swell components is available. Roelvink modelled the reef restoration as an impermeable layer with an increased height of either 0.25 m or 1.25 m (in real-life scale) with increased roughness. In contrast, in the SWASH model, the artificial reefs are schematised as a porous medium, with a real-life scale of 0.75 m.

The wave heights, water levels, reef flat widths, and fore reef slopes studied by Roelvink are comparable to those used in this experiment. Her results showed that a restoration positioned closer to the reef crest increased the setup and therefore had a minimal impact on runup reduction. For the middle and inner reef locations, however, a similar and slightly larger reduction in runup was observed. This thesis observed a similar result for the total wave height with the middle and inner reefs showing similar reductions, while the outer reef location showed a reduced effectiveness. However, this reduced effectiveness in the SWASH model is not due to increased setup, but because of the already present natural dissipation of wave energy at this location, rendering the effect of the artificial reef minimal.

Furthermore, Roelvink's study indicated that the effectiveness reduces with larger wave heights and higher water levels, which can also be observed in the SWASH results, reinforcing that water depth significantly influences the effectiveness of an artificial reef. Her results also showed that the outer restoration had the greatest reduction in sea/swell wave height at the beach toe, while the middle and inner locations had similar reductions for this component. Infragravity wave height reduction was consistent across all reef placements. In contrast, the SWASH results indicate that the outer restoration is most effective at reducing infragravity wave height at the beach toe, while the inner reef best reduces sea/swell wave height.

In summary, while the observed total wave height reduction in this study aligns with the results reported by Roelvink et al. (2021), the reduction for specific wave conditions differs. These differences are likely due to variations in both the schematisation of the artificial reef and the vertical resolution used in the models. Specifically, Roelvink employed XBNH with 2 layers, while this study used SWASH with 10 layers. The additional layers in the SWASH model allow for more detailed wave dynamics, improving the representation of wave energy dissipation and setup. However, other factors, such as the reef schematisation (porous medium vs. impermeable layer), water depths, and wave conditions, could also play roles in the differences between the results.

8.4. Laboratory Experiments

The discrepancies between the numerical model and the laboratory data are also approached with regard to the laboratory results. Limitations in the methodology, laboratory setup and instrumentation, influence the accuracy and validity of the results. Here these limitations are discussed. Additionally, the laboratory results are compared to existing literature on both empirical relations for the transmission coefficient of submerged structures, as well as on the expected frequency dependent energy dissipation according to the theory of Lowe (2005a; 2005b; 2007).

8.4.1. Experimental Setup and Performed Test Runs

The initial plan was to perform experimental runs on two different densities of artificial reef structures for a total of five wave conditions. While these tests were completed, the pressure sensor data appeared to be erroneous and, consequently, unusable. Due to time constraints, only one reef configuration was again tested for just three wave conditions, considerably limiting the data available for validating the numerical model. The pressure sensor data of the initial runs is still under review, but could not yet be used for this thesis.

The limited available data resulted in not being able to find a statistically significant correlation between SWASH and the laboratory data for the offshore infragravity waves. Furthermore, configuration S3 did not show frequency-dependent dissipation, which may be attributed to the high density of the elements. Although configuration S1 has a significantly lower density, a direct comparison could not yet be performed.

Finally, the decomposition of the wave field into an incoming and outgoing component did not function

correctly yet, therefore an analysis into the incoming wave components could not be made. Consequently, the reflected waves now influence the comparison between the lab data and the numerical results.

8.4.2. Low Frequency Peak

A significant discrepancy between the numerical results and laboratory data is observed in the magnitude of infragravity waves, particularly around the energy peak at a frequency of around 0.0074 Hz. First an investigation is performed into resonance processes, as these could be a reason for this low frequency peak. Additionally, the wave generator of the Deltares Wave Flume cannot generate bound subharmonics with a period larger than 50 s, or a frequency below 0.02 Hz. By incorporating this frequency limit into the numerical model, an assessment can be made on how the wave maker's limitations might influence the results.

Resonance

From the energy density spectra a clear peak in the low frequencies can be observed, of which the peak period is relatively constant over the reef flat and also at a similar location for the different conditions. This could result from resonance.

Resonance is a significant phenomenon on fringing reefs, particularly associated with IG and very low-frequency (VLF) waves. The natural resonance frequency of a reef depends on the reef width and the water depth and will therefore vary over time depending water level fluctuations, such as sea level rise and tides. These changes in water levels can potentially lead to a substantial increase in runup height (Pequignet et al., 2009). Resonance over a fringing reef has been observed in the field (Cheriton et al., 2016) and can lead to strong amplification of the runup height. Resonance is especially important for narrow and deep reefs, where the IG and VLF waves caused by the offshore forcing can be close to the natural resonance frequency of the system. The nth resonance frequency of a reef ($f_{N,n}$) is defined by Equation 8.1:

$$f_{N,n} = \frac{(2n+1)\sqrt{gh_{reef}}}{4W_{reef}} \tag{8.1}$$

Where n is the resonant mode (0, 1, 2, ..., n), g is the acceleration due to gravity, h_{reef} is the water depth on the reef flat, and W_{reef} is the width of the reef flat.

The observed low-frequency peak may result not only from resonance of the reef itself, specifically the reef flat, but also from seiching in the entire wave flume, spanning from the wave generator to the beach. To investigate this, the resonance periods of both cases are analysed. Ideally, the location on the beach where the low frequency waves are reflected should be chosen as the boundary of the reef flat width. However, this location is not known, therefore a range in resonance periods for each condition is given based on the range of the swash zone (area between the highest runup level and the lowest), since the wave reflect somewhere within this zone.

Although LIDAR measurements were conducted in the Delta Flume to measure runup, this data was not used in this thesis. Consequently, the swash zone is instead estimated using results from the SWASH model. Furthermore, from the graphs depicting the energy density spectra (Figure 7.9 and 7.10 in Chapter 7, and Figures D.3 to D.6 in Appendix D), the peak frequencies of the lab data can be extracted for each simulation. However, the frequency resolution is relatively course for these very low frequencies. Therefore the frequency resolution is made finer to extract more accurate peak frequencies.

With the water level h, the resonance frequencies and corresponding resonance periods are determined (Table 8.1).

Condition	f_p [hz]	T_p [s]	$T_{r,reef}$ [s]	$T_{r,system}$ [s]
WL33C3	0.0074	135	94 - 143	166 - 215
WL67C3	0.0111	90	100 - 148	168 - 216
WL33C7	0.0093	108	93 - 139	165 - 210
WL67C7	0.0130	77	91 - 135	160 - 203
WL33C11	0.0093	108	93 - 140	164 - 212
WL67C11	0.0093	108	89 - 133	157 - 201

Table 8.1: The observed peak periods T_p and the range in resonance periods for all conditions for the reef system $T_{r,reef}$ and the total wave flume system $T_{r,system}$

The peak periods for the laboratory experiments are around 100 s, with increasing wave energy and water level, lower peak periods. These peak periods seem to fall within the range of the resonance periods of the reef flat. However, the ranges of these resonance periods are relatively independent on water level and wave condition, which is not the case for the observed peak periods. Therefore, it is not likely that the high low-frequency peaks are a result of resonance. Additionally, the resonance periods for the entire system are larger than the observed peak periods, indicating that resonance of the entire system is unlikely.

Basing the potential resonance periods on a range corresponding to the lowest and highest possible runup values, is inaccurate. Therefore, a more thorough investigation is recommended to determine the exact locations at which the long waves reflect. Additionally, a resonance analysis using the numerical model is needed, since the model showed peaks at similar locations. This can be done by adjusting the domain length to see if the peak location remains consistent and by varying the reef width to evaluate its influence on the frequency location of the low-frequency peak.

Frequency Cutoff

As mentioned, the wave generator is capable of generating bound subharmonics with periods up to 50 seconds, corresponding to a frequency of 0.02 Hz. The numerical model, however, can incorporate these harmonics at much lower frequencies, which can introduce differences in the observed low-frequency wave energy between the model and the laboratory data. To address this, an adjustment was made to the numerical model, allowing for the setting of a specific frequency cutoff for the bound subharmonics. In this case, the cutoff frequency was set to 0.02 Hz to match the capabilities of the wave generator.

Figure 8.3 shows the incoming significant wave height H_S over the reef flat for both the laboratory data and the SWASH simulations, including the case with (dashed line) and without (solid line) the 0.02 Hz cutoff frequency. The results show a notable increase in wave height on the reef flat for the numerical results, aligning much more closely with the laboratory data. The improvement is most pronounced for wave condition C11 ($H_S = 1.3m$), the most energetic condition, where the numerical data now nearly matches the laboratory results.

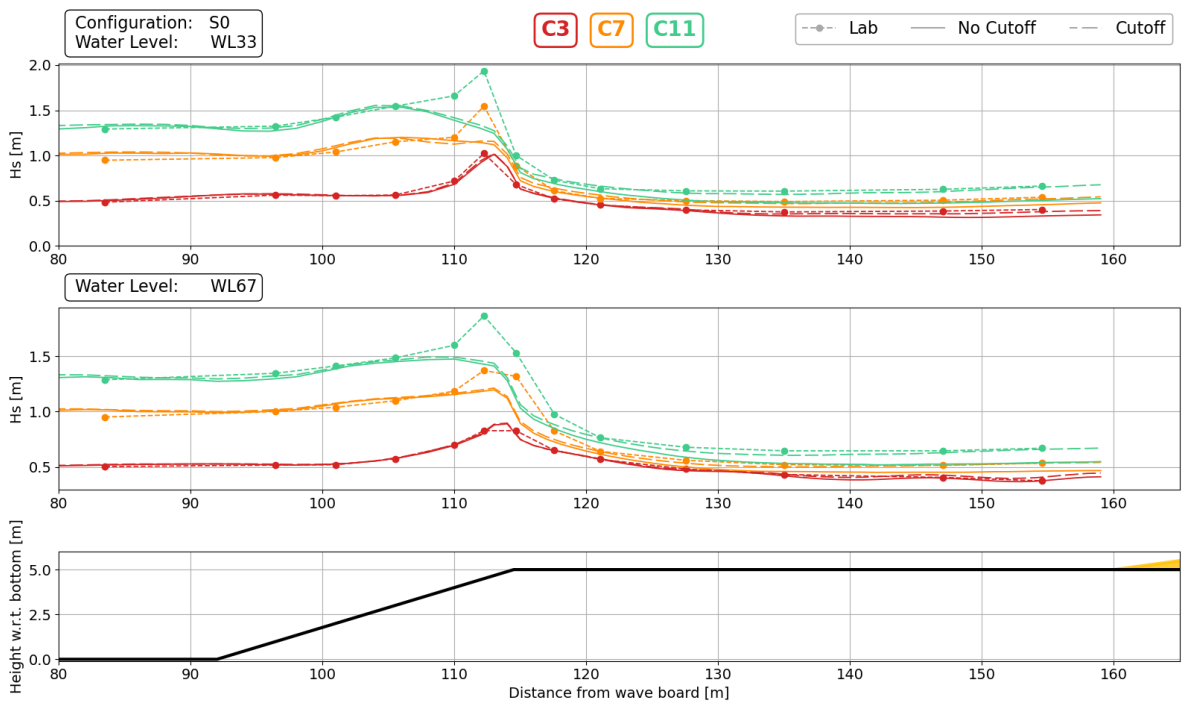

Figure 8.3: Wave transformation of the total wave height H_S for the original numerical simulations not including a low-frequency cutoff (solid line) and for the simulations including the cutoff of 0.02 Hz (dashed line).

The impact of the frequency cutoff can clearly be seen when examining the energy density spectra. Figure 8.4 shows the energy density spectra at several locations on the reef flat for wave condition C11 and water level WL33. The addition of the frequency cutoff at 0.02 Hz (indicated by the black dashed line) results in a substantial increase in wave energy below this threshold. Although the energy levels remain lower than the laboratory data, the numerical model much more accurately describes the data.

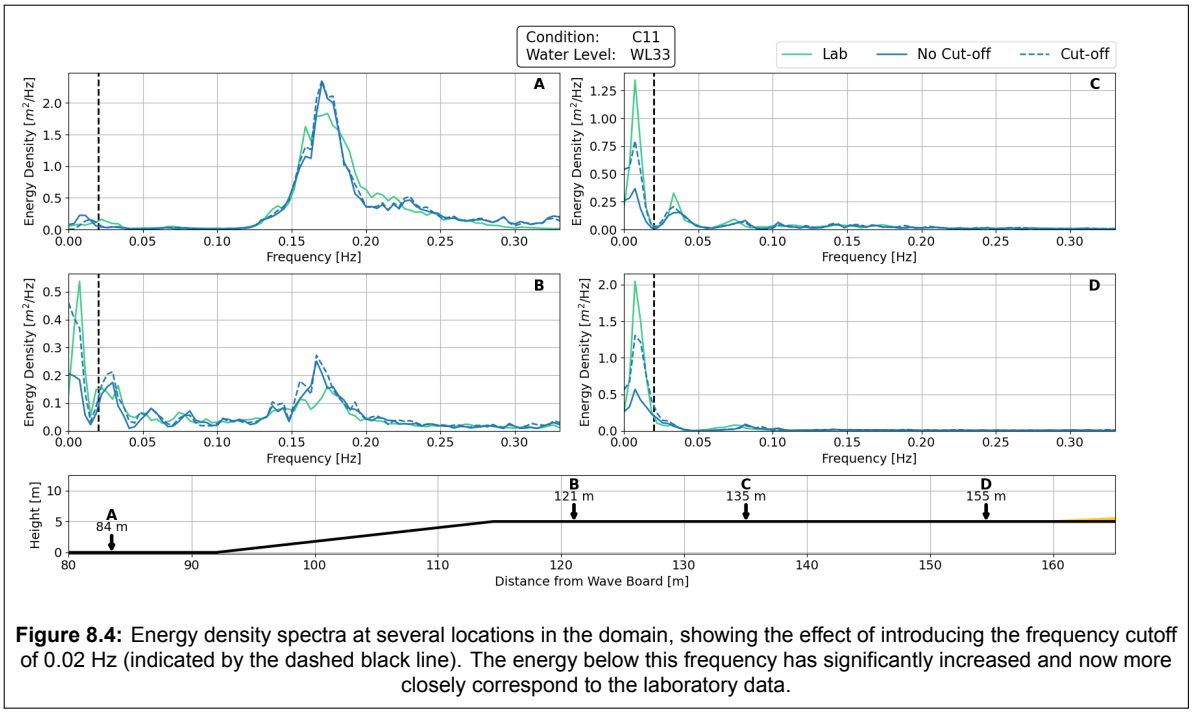

Figure 8.4: Energy density spectra at several locations in the domain, showing the effect of introducing the frequency cutoff of 0.02 Hz (indicated by the dashed black line). The energy below this frequency has significantly increased and now more closely correspond to the laboratory data.

Figure 8.5 shows the transformation of the infragravity waves over the domain for condition C11. While onshore, the infragravity waves are significantly closer in magnitude to the lab data, offshore the wave height is underestimated. This is consistent for all conditions and water levels, which might be a result of other changes to the numerical model that came with the updated version.

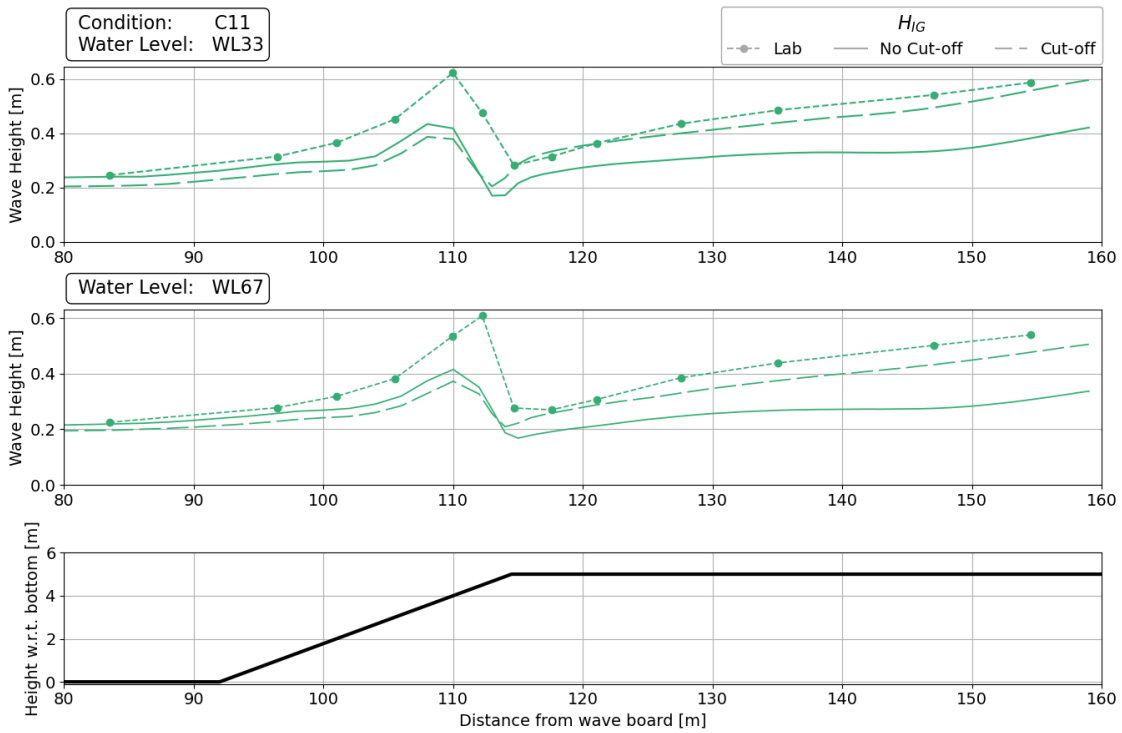

Figure 8.5: Comparison of wave transformation for numerical simulations using the old version of SWASH, without a cutoff, and the new version, both ran with and without the cutoff for low-frequency waves. The difference between the solid line and the dashed-dotted line for the IG wave height indicates other changes to the numerical model which might influence the results.

Therefore, Figure 8.6 shows the wave height transformation for the case with and the case without the cutoff for the latest version of SWASH. The results show for the total wave height H_S (top panel) a minimal difference between the case without the cutoff for both versions of SWASH. The new version does however seem to have a slightly higher wave height over the reef flat. This difference can be found in the infragravity wave height (bottom panel), which show a larger infragravity wave height on the flat for the new version of SWASH. Additionally, the run with the cutoff frequency implemented shows a reduced infragravity wave height offshore. This is unwanted and could be a result of less infragravity wave height added at the offshore boundary because of the higher cutoff frequency.

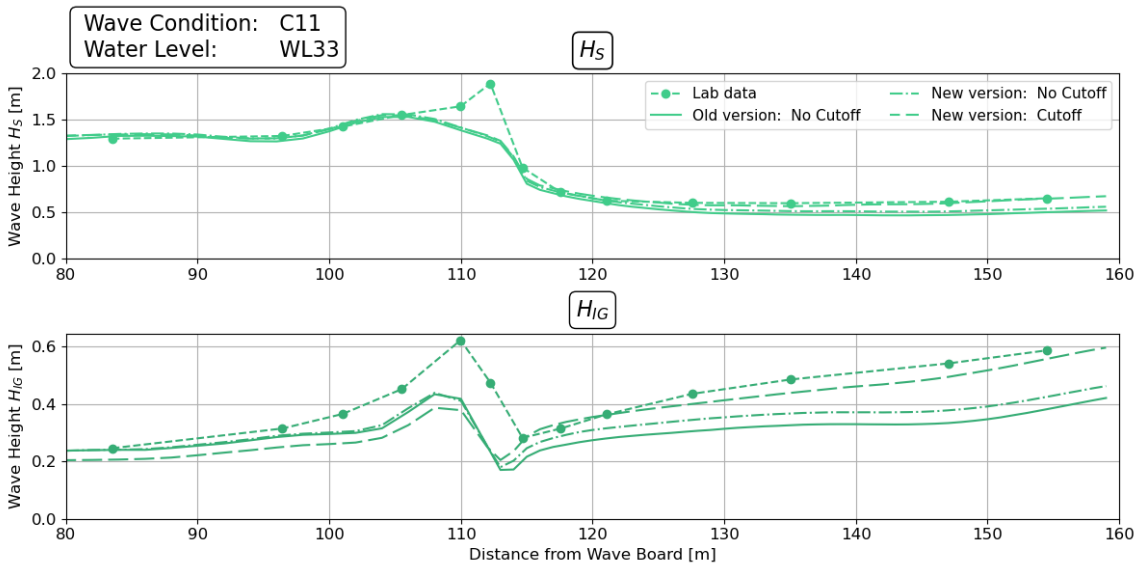

Figure 8.6: Transformation of total wave height H_S (top panel) and IG wave height (bottom panel) over the flat for the original no cutoff case and the simulation including the cutoff of 0.02 Hz. The IG wave height on the reef flat has increased, corresponding to the lab data, while offshore the wave height has decreased.

Additionally, the Root Mean Square Error (RMSE) on the reef flat has significantly decreased. Initially, the RMSE for the infragravity (IG) waves was as high as 0.15 m, which accounted for around 40% of the total IG wave height on the flat. After applying the frequency cutoff, the RMSE reduced to 0.04 m, or just 10% of the IG wave height. While the model still underestimates the IG wave height, the numerical results are now much closer to the laboratory data. It is challenging to explain why limiting the frequency at which bound waves are generated leads to an increase in the observed IG wave height on the reef flat. Intuitively, setting a cutoff should reduce the amount of infragravity wave energy, but the opposite effect is observed.

Implications for the Results

Ideally, all numerical simulations should be rerun with the applied cutoff frequency, including those with an artificial reef configuration. However, due to time constraints and numerical instabilities encountered in the updated version of SWASH, these simulations were not performed. Despite this, it is possible to infer the potential impact of this unnatural low-frequency energy peak on the results.

This low-frequency peak observed in the lab data, with a period of about 100 seconds, introduces an artificial fluctuation in water level across the reef flat. For more energetic wave conditions, this infragravity wave height reaches approximately 0.4 m, while the total water depth on the flat, including setup, is only around 0.6 m for WL33 and 0.9 m for WL67. As a result, this low-frequency wave can be seen as a slow variation in water level, significantly affecting the hydrodynamic processes on the reef, such as wave breaking, wave transformation, and frictional dissipation, all of which are sensitive to water depth.

Additionally, the effectiveness of the artificial reef is highly dependent on water level, with a higher water level resulting in a relatively lower reduction in wave energy. Since these processes are non-linear, the artificial water level fluctuation will most likely skew the results by impacting wave interactions on the reef flat. This influence negatively impacts the validity and applicability of the results.

8.4.3. Empirical Transmission Coefficients

The laboratory experiments conducted with the artificial reef showed a reduction in wave height at the shoreline of 11% for low water levels and 5% for higher water levels. Although tests evaluating wave transmission over these specific structures have not been performed previously, empirical formulations for the transmission coefficient of wave height over submerged structures have been developed. For the purposes of this thesis, a reduction coefficient was introduced, defined as the ratio of wave height

between a case with a reef (restoration) and a case without, at the same location. In contrast, the transmission coefficient is defined as the ratio of wave height onshore of the artificial reef compared to the wave height offshore of it.

Van Gent et al. (2023) derived an empirical expression for various types of submerged breakwater structures. Their formulations were compared to those from other studies, including d'Angremond et al. (1996), Tomasicchio et al. (2011), Goda et al. (2009) and Kurdistani et al. (2022). The new formulation proposed by Van Gent is specifically developed for perforated structures that could represent artificial reefs, and showed good correspondence with the previously established expressions, and even improved accuracy for perforated structures. The equation is given as follows:

$$K_t = c_1 \tanh\left(-\left(\frac{R_c}{H_{m0}} + c_2\left(\frac{B}{L_{m-1,0}}\right)^{c_3} + c_4\right)\right) + c_5 \tag{8.2}$$

The equation includes five coefficients c_1 to c_5 that are dependent on the type structure. For perforated structures, the coefficients were calibrated to c_1 = 0.13, c_2 = 3.1, c_3 = 0.75, c_4 = −0.15 and c_5 = 0.82. R_c represents the freeboard, and $L_{m-1,0}$ the spectral wave period defined as $(g/2\pi)T^2_{m-1,0}$.

Van Gent developed several sets of coefficients c based on the structures tested. Figure 8.7 shows a scatter plot comparing the calculated transmission coefficient K_t and the measured values for two sets of coefficients. To clarify, the measured values shown in the figure represent the transmission coefficient K_t, not the reduction coefficient R_c. The first set, based on the perforated structure, is expected to correspond closely with the artificial reef, while the second set is based on a slightly different structure with a vertical perforated plate. The comparison of both sets of coefficients is made to demonstrate the effect of calibrating the coefficients.

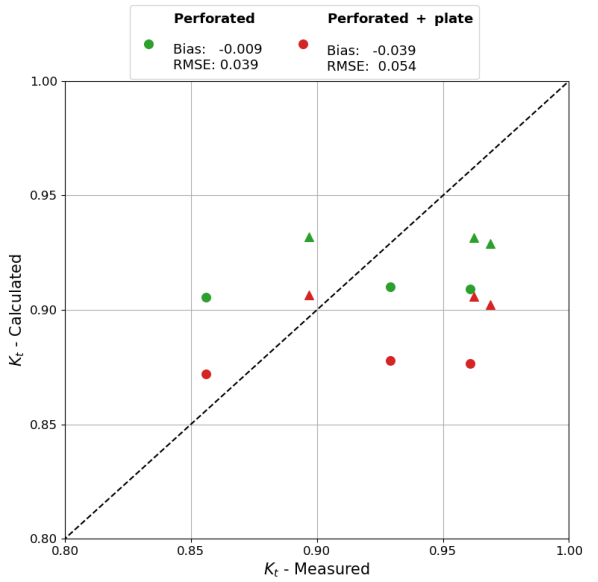

Figure 8.7: Scatter plot showing the calculated transmission coefficient K_t directly behind the restoration and the measured values. Two sets of coefficients are used, developed for slightly different structures.

As shown in the figure, the coefficients calibrated for the perforated structure correspond well with the measured data, and have a bias of -0.009 and a RMSE of 0.039. Conversely, the coefficients for the perforated structure with a plate showed a slightly worse correlation, showing a lower expected transmission and errors with a bias of -0.039 and an RMSE of 0.054. However, an RMSE of 0.039 and 0.054 for a transmission coefficient of around 0.9 is still relatively significant. Moreover, the errors are similar for both water levels, with circles representing WL33 and triangles representing WL67. It is important to note that the measured transmission coefficient is influenced by the wave conditions,

whereas the calculated values are not. This discrepancy arises because, in Equation 8.2, the term R_c/H_{m0} is dominant and remains roughly constant even as the offshore wave height increases.

The coefficients c were specifically calibrated for a perforated structure and predict the measured transmission coefficient for this particular artificial reef configuration relatively well. A second, less dense artificial reef was also tested, though the results are not included in this thesis as the data is not yet available. This configuration is expected to have a different transmission coefficient, yet the proposed coefficients by Van Gent should still be applied, since it resembles the perforated structure of Van Gent as much as the more dense reef. Calculating the transmission coefficient for this second configuration is essential to verify if the same coefficients still predict the reduction with sufficient accuracy.

8.4.4. Frequency Dependence

A significant incentive for the CREST experiments was the limited knowledge on canopy flow dynamics. According to Lowe (2007), higher frequency components are expected to dissipate more energy than lower frequency components. This thesis, however, focuses on wave height reduction rather than energy dissipation. While wave height reduction is related to dissipation, it additionally involves the transfer of energy between different frequency bands, meaning it is not the same as dissipation. With these limitations in mind, the study still investigates the potential frequency dependence of wave height reduction for the SS and IG waves.

The experimental results, however, did not show frequency dependence in wave height reduction. Both infragravity and sea/swell waves exhibited similar reductions in wave height, regardless of offshore forcing and water levels. According to Lowe (2007), frequency-dependent dissipation is expected, particularly when the flow is in the general flow regime, where the ratio between the orbital excursion length A_∞^{rms} and the element spacing S exceeds one.

The orbital excursion length is a function of the free-stream velocity $U_{\infty,\omega}^{rms}$ and the mean spectral period T_{m01}. These values are calculated for each condition at the two closest sensors to the artificial reef: a sensor directly in front at 135 m and a sensor directly behind at 147 m. For each parameter the average value between the two sensors is calculated and displayed in Table 8.2. The table also shows the values calculated for the numerical model.

Case	$U_{\infty,\omega}^{rms}$ [m/s]		$T_{m01}[s]$		A_∞^{rms}/S [-]	
	Lab	SWASH	Lab	SWASH	Lab	SWASH
C3WL33	0.9	0.8	10.4	5.7	5.0	2.8
C7WL33	1.0	1.0	11.4	5.9	6.6	3.3
C11WL33	1.1	1.0	13.3	6.5	8.7	3.9
C3WL67	0.9	0.9	6.0	4.3	3.2	2.3
C7WL67	1.0	0.9	6.9	4.0	3.9	2.2
C11WL67	1.1	1.0	8.4	4.5	5.4	2.8

Table 8.2: Free-stream velocity $U_{\infty,\omega}^{rms}$, mean spectral period T_{m01}, and the ratio of the orbital excursion length A_∞^{rms} over the element spacing S, for all wave conditions and water levels. The difference between the numerical model and the laboratory data stems from the difference in mean spectral period T_{m01}.

The table shows that the free-stream velocity is almost equal for all conditions as well as between the model and the lab data. However, the mean spectral period differs a lot. SWASH shows significantly lower spectral periods for all conditions, which is a result of underestimating the low frequency components. The differences for T_{m01} results in clear differences for the ratio A_∞^{rms}/S, which is between 3.2 and 8.7 for the laboratory data and between 2.2 and 3.9 for the SWASH data. In both cases the flow is in the general flow regime and therefore frequency dependence for the energy dissipation is expected.

While not identical to wave height reduction, a similar response is expected, however frequency dependent wave height reduction was not observed (refer to Table 7.4 in Chapter 7).

There are, however, important differences between Lowe's experiments and the CREST experiments. Lowe (2007) conducted his experiments in the field using cylinders with a height of 10 cm and a diameter of 5 cm, whereas the CREST experiments used much larger elements, with a height of 25 cm and a diameter of 30 cm. Despite similar grid and individual element spacing between the two experiments, Lowe observed much shorter orbital excursion lengths, A_{∞}^{rms}, of only 28 cm, compared to the 1 to 2.4 m observed in the CREST experiments. Additionally, Lowe's rms free-stream velocities, $U_{\infty,w}^{rms}$, were around 0.3 m/s, while the CREST experiments measured approximately 1.0 m/s. Importantly, the findings of Lowe suggest that, for larger velocities, the energy dissipation factor $f_{e,j}$ (Equation 2.1) reaches a minimal value at shorter wave periods.

Lowe observed that $f_{e,j}$ becomes relatively constant for wave components with periods longer than 15 s, which corresponds to a period of around 11 s for the scaled conditions of the CREST experiments. In this thesis, sea/swell waves are defined as those with periods shorter than 20 s. To explore whether most of the energy is concentrated above this 11 s threshold, the mean spectral period T_{m01} of the sea/swell band directly behind the artificial reef is analysed (Table 8.3). Table 8.3 not only shows the T_{m01} of the sea/swell band, but also for the IG waves and the total wave field, including the difference between case S0 and S3.

Case	T_{m01}: SS [s]		T_{m01}: IG [s]		T_{m01}: Total [s]	
	S3	**S0**	**S3**	**S0**	**S3**	**S0**
WL33C3	3.9	3.6	110	98	12.1	11.8
WL33C7	3.7	3.4	97	92	14.9	13.8
WL33C11	4.0	3.8	100	94	17.8	16.6
WL67C3	3.7	3.5	97.9	96.4	5.7	5.5
WL67C7	3.4	3.3	92.9	90.1	8.2	7.8
WL67C11	3.8	3.7	94.6	91.9	10.4	10.1

Table 8.3: Mean spectral period T_{m01} directly behind the artificial reef for the sea/swell band, infragravity wave band and total energy spectrum for both the base case S0 and the case including an artificial reef S3.

The results in Table 8.3 show that the T_{m01} for the SS band is generally around 4 s and slightly higher for the S3 configuration than for the base case S0, indicating more energy in the lower frequencies. However, a similar trend is seen in the T_{m01} for the IG waves, to an even greater extent. Therefore, this increase of T_{m01} likely does not result from frequency-dependent dissipation, but rather from the calculation of the mean spectral periods based on total energy, which includes both incoming and reflected components. Lower frequency components reflect more and therefore the effect on these components is more pronounced.

Additionally, for the conditions of Lowe's experiments, a T_{m01} for the SS band of around 4 s would imply frequency-dependent dissipation. However, the higher velocities (approximately 1 m/s compared to 0.3 m/s) and larger orbital excursion lengths (around 2 m compared to 0.3 m) in this study likely result in the higher frequency components not being driven sufficiently through the artificial reef canopy and therefore dissipate at a similar rate as the lower-frequency components.

Although the less dense artificial reef (S1) has not yet been discussed, it may show frequency-dependent behaviour, and further investigation into this configuration would be valuable.

9

Conclusions & Recommendations

After identifying the limitations of the results and comparing them with existing literature, the final two research questions are addressed. To conclude this thesis, recommendations are provided, regarding the implications of this research for future projects, and suggestions are made for future work.

9.1. Conclusions

In this section, the remaining two research questions are addressed. The first question (Research Question 2) is directed at the optimisation aspect of the laboratory experiments, while the second question (Research Question 3) focuses on analysing the laboratory data and comparing it with the numerical model.

9.1.1. Question 2: Experiment Optimisation

The second research question covers the optimisation of the experimental setup by investigating, by means of numerical modelling, the effect of both the positioning and density an artificial reef has on the wave field. The main research question for this section is as follows:

> **How does the positioning and spacing of the artificial reef influence the energy distribution and wave transformation over the reef flat?**

The research question is answered through two sub-questions, which are answered individually.

> *How does the effect on the total wave field and the sea/swell and infragravity waves vary for restorations positioned at different locations on the reef flat?*

The analysis of the wave height transformation over the reef flat for the three restorations located at the outer, middle, and inner reef flat showed clear differences in total wave height and per wave component. Key findings revealed the following:

1. **Total wave height:** Restoration 1, the outer restoration, showed the least reduction in wave height at the shoreline at 8%, while Restoration 2 and 3, the middle and inner location, respectively, both show a reduction in incoming wave height of 12%. The wave height reduction is highly dependent on offshore hydrodynamic forcing, as the effectiveness of the artificial reefs can be linked to the water depth; larger depths reduce their ability to reduce wave height. Under more energetic conditions, enhanced radiation stress gradients increase the setup and, consequently, the water depth, decreasing the effectiveness of the artificial reef.
2. **Wave height reduction per wave component:** While the reduction of total wave height is roughly the same for each location, significant differences can be seen for the specific SS and IG wave components:

- **Sea/swell waves:** At the shoreline, both the middle and inner restoration show a similar reduction of sea/swell waves at 12% and 14% respectively, while the outermost restoration achieves only a 5% reduction. In contrast, the reduction directly behind each restoration is similar for all restoration locations, ranging from 14% to 16%. This suggests that the differences observed at the shoreline result from the subsequent (lack of) dissipation over the reef flat.
- **Infragravity waves**: The infragravity (IG) waves, however, show a different response. While the relative reduction in IG wave height is independent of the measurement location, it varies significantly depending on the specific location of the restoration. The outer restoration achieves the greatest reduction in IG wave height at 16%, compared to 13% for the middle restoration and 9% for the inner restoration.

The significantly lower reduction of the sea/swell waves for the outer restoration can be attributed to the location on the reef flat. At this location, the natural dissipation (i.e., dissipation in the absence of an artificial reef), primarily due to wave breaking, is still significant, thereby reducing the relative effectiveness of the outer restoration compared to the middle and inner restorations. These latter two restorations are positioned further shoreward, where natural dissipation rates are lower, making them more effective at reducing incoming wave heights. This finding is different from the results of Roelvink et al. (2021), who linked the lower dissipation rates of restorations near the reef crest to elevated setup.

How does the density of the artificial reef affect the wave energy reaching the shoreline?

In SWASH, four different densities were tested for the middle restoration location, located on the middle of the reef flat. The results showed a total wave height reduction of 12% for the lowest density, consisting of 66 elements, or 1.3 units/m^2, stretched over a length of 10 m. Increasing the density to 3.0 units/m^2 (153 elements) resulted in a 19% reduction, approximately 50% greater. However, the number of elements is more than doubled, indicating that increasing the density, even though increasing the total wave height reduction, is not efficient. Furthermore, the magnitude of the reduction was consistent across the densities for each wave condition, water level, and wave component.

9.1.2. Question 3: Data Analysis & Comparison

The third research question analyses the laboratory data on the effectiveness of the artificial reef in reducing wave height. It is also used to make a comparison between the output of the numerical model compared to the actual laboratory results.

How effective is the artificial reef restoration designed for the CREST experiments at reducing wave height, and how does it compare to predictions from the SWASH model?

The research question is split into two parts, in which the first analyses the effectiveness of the artificial reef, while the second focuses on the data comparison.

How do varying water levels and wave conditions influence the performance of the artificial reef in reducing wave height?

Due to complications during experimentation, only a limited number of experimental runs could be performed. Only a single artificial reef has been tested and the effectiveness of this reef in reducing wave height for both the total wave field as well as per wave component differed significantly for varying water levels and wave conditions.

The ratio of the orbital excursion length, A_∞^{rms}, over the spacing S falls within the general flow regime. Therefore, frequency-dependent energy dissipation is expected, with sea/swell waves dissipating more energy than infragravity waves (Lowe, 2007). However, both components show similar wave height reductions, with approximately 11% for the lowest water level and only 5% for the highest water level. This likely results from the relatively large A_∞^{rms} and large flow velocities, preventing the high-frequency

components from being sufficiently driven through the artificial reef canopy. Additionally, while for the lower water levels, the artificial reefs show a lower wave height reduction for the more energetic conditions, the wave height reduction at the higher water level is independent of offshore forcing.

Furthermore, the transmission coefficient K_t has been empirically evaluated with the formulation of Van Gent (2023), of which the results corresponded well with the measured K_t for both water levels.

> *What are the differences in wave energy propagation and reduction over the reef flat between the laboratory data and the numerical predictions of the SWASH model?*

Significant differences between the laboratory data and the numerical predictions could be observed in both the general transformation of the wave energy over the fringing reef as well as the effectiveness of the artificial reef itself.

General Wave Transformation

In general, SWASH underpredicts the wave shoaling and the corresponding breaking wave height, which leads to a difference in setup over the reef. This underprediction can be seen in the RMSE and the bias at the surf zone, where significant errors of up to 50% are observed for all wave components at this location. The magnitude of the underprediction increases under more energetic wave conditions.

Additionally, while SWASH accurately estimates sea/swell wave height over the reef flat, it severely underestimates infragravity wave height. Laboratory data show a strong increase in infragravity wave height over the flat, whereas SWASH predicts limited infragravity wave height, underestimating the laboratory data by up to 50%. Although the magnitude of the low-frequency peak differs significantly between the lab data and the SWASH output, the location of this peak at the shoreline is quite similar. This similarity is reflected in the R-squared value for infragravity waves at the shoreline, which is around 0.9. The significant peak has been attributed to the inability of the Delta Flume to generate bound low-frequency waves with frequencies under 0.02 Hz. Incorporating this cutoff frequency into the numerical model reduces the error in IG wave height on the reef flat from 50% to only 10%.

Effectiveness Artificial Reef

While SWASH underpredicts the general wave transformation over the fringing reef, it severely overpredicts the reduction of wave height over the artificial reef, particularly for the sea/swell waves, with a reduction factor of up to 3 for the higher water level. The dissipation over a porous medium in SWASH is based on three dimensional parameters, which have been calibrated for rubble mound breakwaters. It has been established that the properties of the artificial reef fall outside the range of tests for which these parameters were calibrated. A small sensitivity analysis showed that reducing the β parameter improves the prediction of the SWASH model. However, much lower values for β are needed than those typically found in the literature, suggesting that the porous medium approach used in SWASH may not be optimal for an artificial reef with these specific element dimensions and reef porosity.

The significant overpredictions could also be attributed to the low-frequency waves, which are generated in the SWASH model but not by the wave generator in the Delta Flume.

9.2. Recommendations

Here, recommendations are provided for both the implications of the observed effectiveness of the artificial reef for coastal protection strategies and artificial reef designs in the future, as well as recommendations for future research.

9.2.1. Implications for Real-Life Scenarios and Projects

The artificial reef tested in the experiment is comparable to artificial reef projects conducted in the field, although there are differences in scale. Specifically, the elements in this experiment are smaller (approximately 0.75 m in real-life scale) than those commonly used in the field, such as Reef Balls (around 1.25 m). However, here they are installed over a wider width (30 m compared to the $\sim$10 m typical in real-life projects). The smaller size was chosen to prioritise ecological benefits; while larger elements can have a greater impact on wave reduction, they provide less support for marine life.

The artificial reef achieved only a limited reduction in wave height at 11% for the lower water level and 5% for the higher water level. However, these results represent a bare artificial reef without any marine growth. Over time, corals and other marine life can grow on the structure, increasing the hydraulic roughness and width of the reef, potentially increasing its effectiveness in reducing wave height. Moreover, these smaller artificial reefs, focused on ecology, can be combined with larger structures or integrated into shoreline protection strategies, improving both the ecology and coastal protection. In this way, artificial reefs of this scale can still provide valuable benefits.

It must be noted, however, that with sea levels projected to rise by approximately 1 m by the end of the century (IPCC, 2023), water levels on the reef flat are expected to increase. Given that flood risk increases for larger water levels, artificial reefs should be able to perform best under these conditions. However, with only a 5% reduction in wave height at higher water levels, an artificial reef of this scale, while providing ecological benefits, may not offer sufficient protection against flooding for low-lying islands. Nevertheless, corals are known to grow upwards in response to rising water levels, which could help mitigate the reduction in effectiveness due to sea level rise by increasing the height of the reef.

Additionally, the SWASH simulations using a porous medium approach significantly overestimated the effectiveness of the artificial reef. Even when the dimensional coefficients were calibrated to the lower bound values found in the literature, the overestimation persisted. This suggests that either the parameters require further calibration or the porous medium approach may not be ideal for reefs with high porosities and large elements arranged in a staggered grid. A different modelling approach, such as a vegetation-type model, might be more effective. Therefore, using SWASH with the porous medium approach may not be optimal for accurately assessing reef performance.

Finally, based on the numerical simulations, if artificial reef restorations projects are performed on the reef flat, it is recommended to place them at the middle or inner location of the reef flat, since reefs at these locations are most effective at dissipating wave energy.

9.2.2. Recommendations for Future Research

The following recommendations are made for future work.

1. **Investigate Wave Groupiness**

   For the numerical analysis on the experiment optimisation (Chapter 6), the comparatively lower reduction of sea/swell waves for the outer reef restoration was explained. However, an explanation for its increased reduction in infragravity waves was not. One possible approach to clarify this is by examining wave groupiness. Wave groupiness can be quantified with the Groupiness Factor (GF), which is a statistical measure of the degree of variation of individual waves within a wave group (Liu et al., 2021). The GF is based on the envelope of the incident-wave time series and peaks at the surf zone, where nonlinear processes cause wave energy to be transferred from the peak period to both higher frequencies and infragravity waves (List, 1991; Kuznetsov, 2002).

   Several formulations for the Groupiness Factor have been proposed with the first formulation incorporating the wave envelope by List (1991) being further refined several times, for instance by Dong et al. (2008) and later by Liu et al., (2021). The formulation by List is as follows:

   $$GF = \frac{\sqrt{2}\sigma_A}{\overline{A(t)}} \tag{9.1}$$

   where σ_A is the standard deviation of the wave envelope A(t), and $\overline{A(t)}$ represents the mean. This envelope time series can be derived using a low-pass filter, of which the cutoff frequency has to be selected with care, as it significantly affects the GF.

   Wave groups with a larger GF are expected to be able to transfer more energy to the infragravity waves. Since the outer reef restoration is closer to the reef crest, the wave groupiness is expected to be larger in this location. Therefore, dissipating sea/swell energy at this location, although with the same magnitude as for the other locations, reduces the energy that can be transferred to

the lower frequencies more significantly. It is recommended to calculate the GF for the wave-time series of the numerical simulations, and the correlation between the GF at each restoration location and at the shoreline.

2. **Perform analysis on low density configuration S1**

   Due to time constraints, the pressure sensor data for the experimental runs of configuration S1 has not yet been validated. This configuration has a lower density, which provides additional data for model validation and is valuable for comparing with the empirical formulation by Van Gent (2023) for the transmission coefficient, as well as for analysing frequency-dependent energy dissipation as proposed by Lowe et al. (2007).

3. **Perform analysis on decomposed wave field**

   Time constraints also prevented the decomposition of the wave field into an incoming and outgoing component. To enable a more detailed and accurate analysis of the artificial reef's effects, it is recommended to analyse the incoming wave field using the available pressure and velocity sensor data. Additionally, a detailed analysis of wave reflection at both the shoreline and the artificial reef can provide valuable insights that were not addressed in this thesis.

4. **Conduct stability tests**

   A stability analysis on the reef elements has been conducted using empirical coefficient values found in literature. An investigation into the stability of the elements used by Speth (2023), suggested that these elements should have been unstable; however, they remained stable during experimentation. This finding highlights the considerable uncertainties in stability predictions based on empirical coefficients, particularly for elements situated in shallow waters subject to significant flow velocities. Conducting stability tests on such elements is essential for improving the predictive accuracy of empirical formulations of the stability criteria.

5. **Run additional SWASH simulations with a low-frequency cutoff**

   It is recommended to conduct additional SWASH simulations for the cases involving an artificial reef using a version of SWASH that supports the implementation of a low-frequency cutoff for the generation of bound subharmonics. Only the base case (S0) has been rerun in this study due to time constraints and numerical instability within SWASH. Performing these simulations for cases with a porous medium may yield results that align more closely with the laboratory experiments, and could show a different impact of the artificial reefs on the wave field.

6. **Conduct sensitivity analysis on the dimensional parameters**

   A limited sensitivity analysis of the SWASH model's dimensional parameters was conducted. Given the significant range in the proposed values of these dimensional parameters, it is recommended to perform further calibration of these parameters. Calibration can enhance model predictions and achieve better alignment with the experimental results

7. **Explore different schematisation approaches for artificial reefs**

   While fully 3D CFD models are capable of explicitly resolving the detailed geometry of artificial reefs, models such as SWASH, Boussinesq-type models, or XBeach Non-Hydrostatic+ require simplified representations (schematisations) of the reef structure. This thesis focused exclusively on the porous medium approach of SWASH for modelling artificial reefs; however, alternative methods are also available.

   It is recommended to investigate, compare, and calibrate various modelling approaches using laboratory results. For example, while XBeach Non-Hydrostatic+ also allows an artificial reef to be schematised as a porous medium, it uses the horizontal in-canopy momentum equation derived by Lowe et al. (2008), rather than the Van Gent equations (1995) employed in SWASH. The in-canopy momentum equation in XBNH includes a frequency-dependence term, which may offer a more accurate representation of the processes. However, XBNH+ is limited to a maximum of two vertical layers, whereas SWASH can offer finer vertical resolution.

   Another modelling approach is a vegetation-type model, which has been applied to both SWASH and XBeach Non-Hydrostatic (Reis et al., 2020; van Rooijen et al., 2016). Vegetation can be modelled as rigid cylinders with specific spacing and element diameters. These parameters can also be used to describe an artificial reef. However, the studies on vegetation models often

focus on denser elements with smaller diameters. Therefore, the applicability of this approach for modelling artificial reefs with larger elements and spacing requires further investigation.

8. **Perform full CFD simulations on oscillatory flow**

   Preliminary CFD simulations were conducted by Akshay Patil (Figure 6.13 and 6.12). He modelled turbulent channel flow under a pressure gradient (Patil and Fringer, 2022). A more accurate approach, though computationally intensive, would involve CFD simulations with an oscillatory flow that replicates the laboratory conditions. These results could then be validated against in-canopy velocity measurements from the array of Vectrinos (ADV's) located inside the canopy of the artificial reef. Additionally, the data of the Vectrinos can be used to investigate the in-canopy flow field and compare the findings to expected values based on work of for example Lowe et al. (2007).

9. **Conduct field experiments**

   Field experiments are necessary due to the limitations of the wave generator, which could not generate bound subharmonics with frequencies below 0.02 Hz, leading to abnormally large low-energy peaks on the reef flat. It is advisable to either improve the wave generator, which is a challenging task, or conduct field experiments on an artificial reef using similar elements.

References

Amores, A., Marcos, M., Pedreros, R., Le Cozannet, G., Lecacheux, S., Rohmer, J., … Khaleel, Z. (2021). Coastal flooding in the maldives induced by mean sea-level rise and wind-waves: From global to local coastal modelling. *Frontiers in Marine Science*, *8*, 665672. doi: 10.3389/fmars.2021.665672

Bayraktarov, E., Stewart-Sinclair, P., Brisbane, S., Boström-Einarsson, L., Saunders, M., Lovelock, C., … Wilson, K. (2019). Motivations, success, and cost of coral reef restoration. *Restor Ecol*, *27*, 981-991. doi: 10.1111/rec.12977

Becker, J. M., Merrifield, M. A., & Ford, M. (2014). Water level effects on breaking wave setup for pacific island fringing reefs. *Journal of Geophysical Research: Oceans*, *119*(2), 914-932. doi: 10.1002/2013JC009373

Birrell, C. L., McCook, L. J., Willis, B. L., & Diaz-Pulido, G. A. (2008). Effects of benthic algae on the replenishment of corals and the implications for the resilience of coral reefs. In *Oceanography and marine biology* (1st ed., p. 40). CRC Press.

Bishop, C., & Donelan, M. (1987). Measuring waves with pressure transducers. *Coastal Engineering*, *11*(4), 309-328. doi: 10.1016/0378-3839(87)90031-7

Bosboom, J., & Stive, M. (2021). *Coastal dynamics*. Delft University of Technology, Faculty of Civil Engineering and Geosciences. doi: 10.5074/T.2021.001

Brodie, K., & Cohn, N. (2021). Coastal geology: Coastal landforms and processes. In D. Alderton & S. A. Elias (Eds.), *Encyclopedia of geology* (Second Edition ed., p. 894-905). Oxford: Academic Press. doi: 10.1016/B978-0-12-409548-9.12483-2

Buckley, M., Lowe, R., & Hansen, J. (2014). Evaluation of nearshore wave models in steep reef environments. *Ocean Dynamics*, *64*(6), 847–862. doi: 10.1007/s10236-014-0713-x

Buckley, M., Lowe, R., Hansen, J., & van Dongeren, A. (2015, 09). Dynamics of wave setup over a steeply sloping fringing reef. *Journal of Physical Oceanography*, *45*, 150923131654000. doi: 10.1175/JPO-D-15-0067.1

Burcharth, H., & Andersen, O. (1995). On the one-dimensional steady and unsteady porous flow equation. *Coastal Engineering*, *24*(3-4), 233–257. doi: 10.1016/0378-3839(94)00025-S

Carlot, J., Vousdoukas, M., Rovere, A., Karambas, T., Lenihan, H., Kayal, M., … Parravicini, V. (2023, Jan 30). Coral reef structural complexity loss exposes coastlines to waves. *Sci Rep*, *13*(1), 1683. doi: 10.1038/s41598-023-28945-x

Chappell, J. (1980). Coral morphology, diversity and reef growth. *Nature*, *286*, 249–252. doi: 10.1038/286249a0

Chen, N., Saleh, E., Yap, T., & Isnain, I. (2018, 12). Effect of artificial structures on shoreline profile of selingan island, sandakan, sabah, malaysia. *Borneo Journal of Marine Science and Aquaculture (BJoMSA)*, *2*, 9-15. doi: 10.51200/bjomsa.v2i0.1304

Cheriton, O., Storlazzi, C., & Rosenberger, K. (2016). Observations of wave transformation over a fringing coral reef and the importance of low-frequency waves and offshore water levels to runup, overwash, and coastal flooding. *J. Geophys. Res. Oceans*, *121*, 3121-3140. doi: 10.1002/2015JC011231

Chow, V. T. (1959). *Open-channel hydraulics*. McGraw-Hill.

d'Angremond, K., Van Der Meer, J., & De Jong, R. (1996). Wave transmission at low-crested structures. In *Coastal engineering.* American Society of Civil Engineers. doi: 10.1061/9780784402429.187

Dekkers, J. (2018). *Master thesis* (MSc Thesis, Civil Engineering & Geosciences, Delft University of Technology). Retrieved from http://resolver.tudelft.nl/uuid:cb525042-e19e-455a-b05d-4820d0e5b6bc

Demirbilek, Z., Nwogu, O., & Ward, D. (2007). Laboratory study of wind effect on runup over fringing reefs, report 1: data report.

Diederen, C. (2022). *Experimental wave flume study: the stability of an artificial reef* (Master's thesis, Delft University of Technology, Delft, Netherlands). Retrieved from http://resolver.tudelft.nl/uuid:16c0b36b-9137-4297-a47e-6c53f0ee3826

Dong, G., Ma, Y., & Ma, X. (2008). Cross-shore variations of wave groupiness by wavelet transform. *Ocean Engineering*, *35*(7), 676-684. doi: 10.1016/j.oceaneng.2007.12.004

Düzbastilar, F., & Şentürk, U. (2009, 09). Determining the weights of two types of artificial reefs required to resist wave action in different water depths and bottom slopes. *Ocean Engineering*, *36*, 900-913. doi: 10.1016/j.oceaneng.2009.06.008

Fang, K., Yin, J., Liu, Z., Sun, J., & Zou, Z. (2014). Revisiting study on boussinesq modeling of wave transformation over various reef profiles. *Water Science and Engineering*, *7*(3), 306-318. doi: 10.3882/j.issn.1674-2370.2014.03.006

Garcia, N., Lara, J., & Losada, I. (2004). 2-d numerical analysis of near-field flow at low-crested permeable breakwaters. *Coastal Engineering*, *51*(10), 991-1020. doi: 10.1016/j.coastaleng.2004.07.017

Gijón, A., Jansen, W., Uijttewaal, W., Reniers, A., van Rooijen, A., Suzuki, T., … Winterwerp, J. (2021, 07). Wave transmission and drag coefficients through dense cylinder arrays: Implications for designing structures for mangrove restoration. *Ecological Engineering*, *165*, 106231. doi: 10.1016/j.ecoleng.2021.106231

Goda, Y., & Ahrens, J. (2009). New formulation of wave transmission over and through low-crested structures. In (p. 3530-3541). doi: 10.1142/9789814277426_0293

Guo, J. (2002). Simple and explicit solution of wave dispersion equation. *Coastal Engineering*, *45*(2), 71–74. doi: 10.1016/S0378-3839(02)00039-X

Guza, R., Thornton, E., & Holman, R. (1985, 11). Swash on steep and shallow beaches. In (p. 708-723). doi: 10.1061/9780872624382.049

Harris, D., & et al. (2018). Coral reef structural complexity provides important coastal protection from waves under rising sea levels. *Sci. Adv.*, *4*(eaao4350). doi: 10.1126/sciadv.aao4350

Harris, L. (2005). *Stability analysis for the submerged reef ball breakwater proposed for the mayan palace resort, quintana roo, mexico* (Technical Report). Florida Institute of Technology, Division of Marine & Environmental Systems. (Performed for Marenter, S.A. de C.V., Cancun, Q. Roo, Mexico)

Harry, D. (2022, March). *Ellaidhoo maldives by cinnamon: Trip report.* Retrieved from https://scubaboard.com/community/threads/ellaidhoo-maldives-by-cinnamon.618714/ (Accessed: 2024-09-12)

Hsu, T., Sakakiyama, T., Philip, L., & Liu, F. (2002). A numerical model for wave motions and turbulence flows in front of a composite breakwater. *Coastal Engineering*, *46*(1), 25-50. doi: 10.1016/S0378-3839(02)00045-5

Kennedy, J., & Woodroffe, C. D. (2002). Fringing reef growth and morphology: a review. *Journal of Coral Reef Studies*, *12*(3), 123-145. doi: 10.1016/S0012-8252(01)00077-0

Kurdistani, S., Tomasicchio, G., D'Alessandro, F., & Francone, A. (2022). Formula for wave transmission at submerged homogeneous porous breakwaters. *Ocean Engineering*, *266*, 113053. doi: 10.1016/j.oceaneng.2022.113053

Kuznetsov, S., & Saprykina, Y. (2002, 05). An experimental study of the near-shore evolution of wave groups. *Oceanology*, *42*, 336-343.

Lara, J., arcía, N., & Losada, I. (2006, apr). Rans modelling applied to random wave interaction with submerged permeable structures. *Coastal Engineering*, *53*(5-6), 395–417. doi: 10.1016/j.coastaleng.2005.11.003

Lashley, C., Roelvink, D., Van Dongeren, A., Buckley, M., & Lowe, R. (2018). Nonhydrostatic and surfbeat model predictions of extreme wave run-up in fringing reef environments. *Coastal Engineering*, *137*, 11-27. doi: 10.1016/j.coastaleng.2018.03.007

Lee, H., & Romero, J. (Eds.). (2023). *Climate change 2023: Synthesis report. contribution of working groups i, ii and iii to the sixth assessment report of the intergovernmental panel on climate change*. Geneva, Switzerland: IPCC. doi: 10.59327/IPCC/AR6-9789291691647

List, J. (1991). Wave groupiness variations in the nearshore. *Coastal Engineering*, *15*(5), 475-496. doi: 10.1016/0378-3839(91)90024-B

Liu, W., Shao, K., Ning, Y., & Zhao, X. (2020). Numerical study of the impact of climate change on irregular wave run-up over reefringed coasts. *China Ocean Engineering*, *34*(2), 162-171. doi: 10.1007/s13344-020-0016-6

Liu, Y., Liao, Z., Fang, K., & Li, S. (2021). Uncertainty of wave runup prediction on coral reef-fringed coasts using swash model. *Ocean Engineering*, *242*, 110094. doi: 10.1016/j.oceaneng.2021.110094

Losada, I., Lara, J., Guanchem, R., & Gonzalez-Ondina, J. (2008). Numerical analysis of wave overtopping of rubble mound breakwaters. *Coastal Engineering*, *55*(1), 47-62. doi: 10.1016/j.coastaleng.2007.06.003

Lowe, R., Falter, J., Koseff, J., Monismith, S., & Atkinson, M. (2007). Spectral wave flow attenuation within submerged canopies: Implications for wave energy dissipation. *J. Geophys. Res.*, *112*, C05018. doi: 10.1029/2006JC003605

Lowe, R., Koseff, J., & Monismith, S. (2005b). Oscillatory flow through submerged canopies: 1. velocity structure. *J. Geophys. Res.*, *110*, C10016. doi: 10.1029/2004JC002788

Lowe, R., Koseff, J., Monismith, S., & Falter, J. (2005a). Oscillatory flow through submerged canopies: 2. canopy mass transfer. *J. Geophys. Res.*, *110*, C10017. doi: 10.1029/2004JC002789

Lowe, R., Leon, A., Symonds, G., Falter, J., & Gruber, R. (2015). The intertidal hydraulics of tide-dominated reef platforms. *Journal of Geophysical Research: Oceans*, *120*(7), 4845-4868. doi: 10.1002/2015JC010701

Lowe, R. J., Shavit, U., Falter, J. L., Koseff, J. R., & Monismith, S. G. (2008). Modeling flow in coral communities with and without waves: A synthesis of porous media and canopy flow approaches. *Limnology and Oceanography*, *53*(6), 2668–2680. doi: 10.4319/lo.2008.53.6.2668

Monismith, S., Rogers, J., Koweek, D., & Dunbar, R. (2015). Frictional wave dissipation on a remarkably rough reef. *Geophys. Res. Lett.*, *42*, 4063–4071. doi: 10.1002/2015GL063804

Montanio, P. (2019). *Announcing mission: Iconic reefs–an unprecedented, large-scale coral reef restoration effort in the florida keys.* https://www.fisheries.noaa.gov/leadership-message/announcing-mission-iconic-reefs-unprecedented-large-scale-coral-reef-restoration. (Accessed on 23 January 2024)

Morison, J., Johnson, J., & Schaaf, S. (1950, 05). The force exerted by surface waves on piles. *Journal of Petroleum Technology*, *2*(05), 149-154. doi: 10.2118/950149-G

National Oceanic and Atmospheric Administration (NOAA). (2023). *Shallow coral reef habitat.* Retrieved from https://www.fisheries.noaa.gov/national/habitat-conservation/shallow-coral-reef-habitat (Accessed: 2024-09-11)

NOAA National Ocean Service. (2023). *The role of zooxanthellae in coral health.* Retrieved from https://oceanservice.noaa.gov/education/tutorial_corals/coral02_zooxanthellae.html (Accessed: 2024-09-11)

Norris, B., Storlazzi, C., Pomeroy, A., Rosenberger, K., Logan, J., & Cheriton, O. (2023). Combining field observations and high-resolution numerical modeling to demonstrate the effect of coral reef roughness on turbulence and its implications for reef restoration design. *Coastal Engineering*, *184*, 104331. doi: 10.1016/j.coastaleng.2023.104331

Obura, D., Gudka, M., Samoilys, M., Osuka, K., Mbugua, J., Keith, D., … Zivane, F. (2022). Vulnerability to collapse of coral reef ecosystems in the western indian ocean. *Nature Sustainability*, *5*, 104-113. doi: 10.1038/s41893-021-00817-0

Patil, A., & Fringer, O. (2022, 09). Drag enhancement by the addition of weak waves to a wave-current boundary layer over bumpy walls. *Journal of Fluid Mechanics*, *947*. doi: 10.1017/jfm.2022.628

Pearson, S. (2016). *Predicting wave-induced flooding on low-lying tropical islands using a bayesian network* (Master's thesis, Delft University of Technology). Retrieved from http://resolver.tudelft.nl/uuid:c3988f4b-99f8-4936-9504-261b32bb0cd1

Pearson, S. G., Storlazzi, C. D., van Dongeren, A. R., Tissier, M. F. S., & Reniers, A. J. H. M. (2017). A bayesian-based system to assess wave-driven flooding hazards on coral reef-lined coasts. *Journal of Geophysical Research: Oceans*, *122*(12), 10099-10117. doi: 10.1002/2017JC013204

Pilechi, A., Baker, S., & Cornett, A. (2018). Evaluation of a numerical wave modelling tool for studying the overtopping of rubblemound breakwaters. In *Proceedings of the 7th international conference on the application of physical modelling in coastal and port engineering and science (coastlab18).* National Research Council Canada.

Piniak, G. (2002). Effects of symbiotic status, flow speed, and prey type on prey capture by the facultatively symbiotic temperate coral oculina arbuscula. *Marine Biology*, *141*(3), 449–455. doi: 10.1007/s00227-002-0825-6

Pomeroy, A., Ghisalberti, M., Peterson, M., & Farooji, V. (2023). A framework to quantify flow through coral reefs of varying coral cover and morphology. *PLOS ONE*, *18*(1), e0279623. doi: 10.1371/journal.pone.0279623

Pomeroy, A., Lowe, R., Symonds, G., Van Dongeren, A., & Moore, C. (2012). The dynamics of infragravity wave transformation over a fringing reef. *J. Geophys. Res.*, *117*, C11022. doi: 10.1029/2012JC008310

Pomeroy, A., Lowe, R. J., van Dongeren, A., Ghisalberti, M., & Bodde, W. (2015). Spectral wave-driven sediment transport across a fringing reef. *Coastal Engineering*, *98*, 78–94. doi: 10.1016/j.coastaleng.2015.01.005

Péquignet, A., Becker, J. M., Merrifield, M. A., & Aucan, J. (2009). Forcing of resonant modes on a fringing reef during tropical storm man-yi. *Geophysical Research Letters*, *36*, L03607. doi: 10.1029/2008GL036259

Qu, K., Wang, X., Yao, Y., Men, J., & Gao, R. (2024). Numerical investigation of infragravity wave hydrodynamics at fringing reef with a permeable layer. *Continental Shelf Research*, *275*, 105212. doi: 10.1016/j.csr.2024.105212

Rathnayaka, D., & Tajima, Y. (2023). Influence of the permeability of submerged breakwaters on surrounding wave and current fields. *Coastal Engineering Journal*, *65*(3), 369–382. doi: 10.1080/21664250.2023.2211793

Reef Beach. (2024). *Shoreline restoration.* Retrieved from https://www.reefbeach.com/ (Accessed: 2024-11-19)

Reef Systems. (2024). *Modular sealife system (moses).* https://www.reefsystems.org/moses. (Accessed: 2024-09-12)

Reis, R., Pires-Silva, A., & Fortes, C. (2020). Experiences with swash on modelling wave propagation over vegetation: comparisons with lab and field data. *Revista de Gestão Costeira Integrada*, *20*, 145-150. doi: 10.5894/rgci-n303

Roelvink, F., Storlazzi, C., van Dongeren, A., & Pearson, S. (2021). Coral reef restorations can be optimized to reduce coastal flooding hazards. *Frontiers in Marine Science*, *8*. doi: 10.3389/fmars.2021.653945

Smit, P., Zijlema, M., & Stelling, G. (2013, June). Depth-induced wave breaking in a non-hydrostatic, near-shore wave model. *Coastal Engineering*, *76*, 1–16. doi: 10.1016/j.coastaleng.2013.01.008

Speth, F. (2023). *Physical modelling of 3d-printed artificial reefs with complex shapes in the wave flume* (Master's thesis, Delft University of Technology). Retrieved from http://resolver.tudelft.nl/uuid:127ebe10-bfa8-41ff-810e-7a2a03facfc0 (Master's thesis)

Spieler, R. E., Gilliam, D. S., & Sherman, R. L. (2001). Artificial substrate and coral reef restoration: What do we need to know to know what we need. *Bulletin of Marine Science*, *69*(2), 1013–1030.

Srineash, V., Kamath, A., Murali, K., & Bihs, H. (2020, 07). Numerical simulation of wave interaction with submerged porous structures and application for coastal resilience. *Journal of Coastal Research*, *36*, 752. doi: 10.2112/JCOASTRES-D-19-00147.1

Symonds, G., Huntley, D., & Bowen, A. (1982). Two-dimensional surf beat: Long wave generation by a time-varying breakpoint. *Journal of Geophysical Research*, *87*(C1), 492. doi: 10.1029/JC087iC01p00492

Tomasicchio, G., Aristodemo, F., & Veltri, P. (2009). Wave and current hydrodydynamic coefficients for bottom pipeline stability. In *Coastal structures 2007* (p. 1067-1078). doi: 10.1142/9789814282024_0094

Tomasicchio, G., D'Alessandro, F., & Tundo, G. (2011). Further developments in a new formulation of wave transmission. In *Coastal structures 2011* (p. 634-645). doi: 10.1142/9789814412216_0055

Van den Bos, J., Verhagen, H., Zijlema, M., & Mellink, B. (2014). Towards a practical application of numerical models to predict wave-structure interaction: an initial validation. *Coastal Engineering Proceedings*(34), 50–50. Retrieved from https://resolver.tudelft.nl/uuid:97f11a22-56ad-4504-a42a-cfedcb3677ca

Van Dongeren, A. (2020). *Waves on reefs: How coral reefs transform waves and help protect coasts.* Retrieved from https://www.youtube.com/watch?app=desktop&v=JvTmDnoy8E0 (Keynote speech)

Van Dongeren, A., Lowe, R., Pomeroy, A., Trang, D., Roelvink, J., Symonds, G., & Ranasinghe, R. (2013). Numerical modeling of low-frequency wave dynamics over a fringing coral reef. *Coastal Engineering*, *73*, 178–190. doi: 10.1016/j.coastaleng.2012.11.004

Van Gent, M. (1995, 05). Porous flow through rubble-mound material. *Journal of Waterway Port Coastal and Ocean Engineering-asce - J WATERW PORT COAST OC-ASCE*, *121*. doi: 10.1061/(ASCE)0733-950X(1995)121:3(176)

Van Gent, M., Buis, L., Van Den Bos, J., & Wüthrich, W. (2023). Wave transmission at submerged coastal structures and artificial reefs. *Coastal Engineering*, *184*, 104344. doi: 10.1016/j.coastaleng.2023.104344

Van Rooijen, A., McCall, R., van Thiel de Vries, J., van Dongeren, A., Reniers, A., & Roelvink, J. (2016). Modeling the effect of wave-vegetation interaction on wave setup. *Journal of Geophysical Research: Oceans*, *121*(6), 4341-4359. doi: 10.1002/2015JC011392

Van Wiechen, P. (2020). *Wave dissipation on a complex coral reef: An experimental study* (Master's thesis, Delft University of Technology). Retrieved from http://resolver.tudelft.nl/uuid:4aa6e365-5ea3-4777-b2f0-1769817d587a

Vetter, O., Becker, J., Merrifield, M., Pequignet, A., Aucan, J., Boc, S., & Pollock, C. (2010). Wave setup over a pacific island fringing reef. *Journal of Geophysical Research: Oceans*, *115*(C12). doi: 10.1029/2010JC006455

Woo, J., Kim, D., Yoon, H., & Na, W. (2014). Characterizing korean general artificial reefs by drag coefficients. *Ocean Engineering*, *82*, 105-114. doi: 10.1016/j.oceaneng.2014.02.025

Woodroffe, C. D. (2002). *Coasts: Form, process, and evolution*. The Pitt Building, Trumpington Street, Cambridge, United Kingdom: Cambridge University Press. Retrieved from http://www.cambridge.org (Published by the Press Syndicate of the University of Cambridge)

Woodworth, P. (2005). Have there been large recent sea level changes in the maldive islands? *Global and Planetary Change*, *49*(1), 1-18. doi: 10.1016/j.gloplacha.2005.04.001

World Wildlife Fund. (2023). *Everything you need to know about coral bleaching—and how we can stop it.* Retrieved from https://www.worldwildlife.org/pages/everything-you-need-to-know-about-coral-bleaching-and-how-we-can-stop-it

Yao, Y., Chen, X., Xu, C., Jia, M., & Jiang, C. (2022). Numerical modelling of wave transformation and runup over rough fringing reefs using varans equations. *Applied Ocean Research*, *118*, 102952. doi: 10.1016/j.apor.2021.102952

Yao, Y., Huang, Z., Monismith, S., & Lo, E. (2012). 1dh boussinesq modeling of wave transformation over fringing reefs. *Ocean Engineering*, *47*, 30-42. doi: 10.1016/j.oceaneng.2012.03.010

Z., M., S., G., & S., P. (2011). Swash: An operational public domain code for simulating wave fields and rapidly varied flows in coastal waters. *Coastal Engineering*, *58*(10), 992-1012. doi: 0.1016/j.coastaleng.2011.05.015

Zijlema, M. (2012, 12). Modelling wave transformation across a fringing reef using swash. coast eng proc 1(33) (currents.26). In (Vol. 1). doi: 10.9753/icce.v33.currents.26

A

Instrumentation

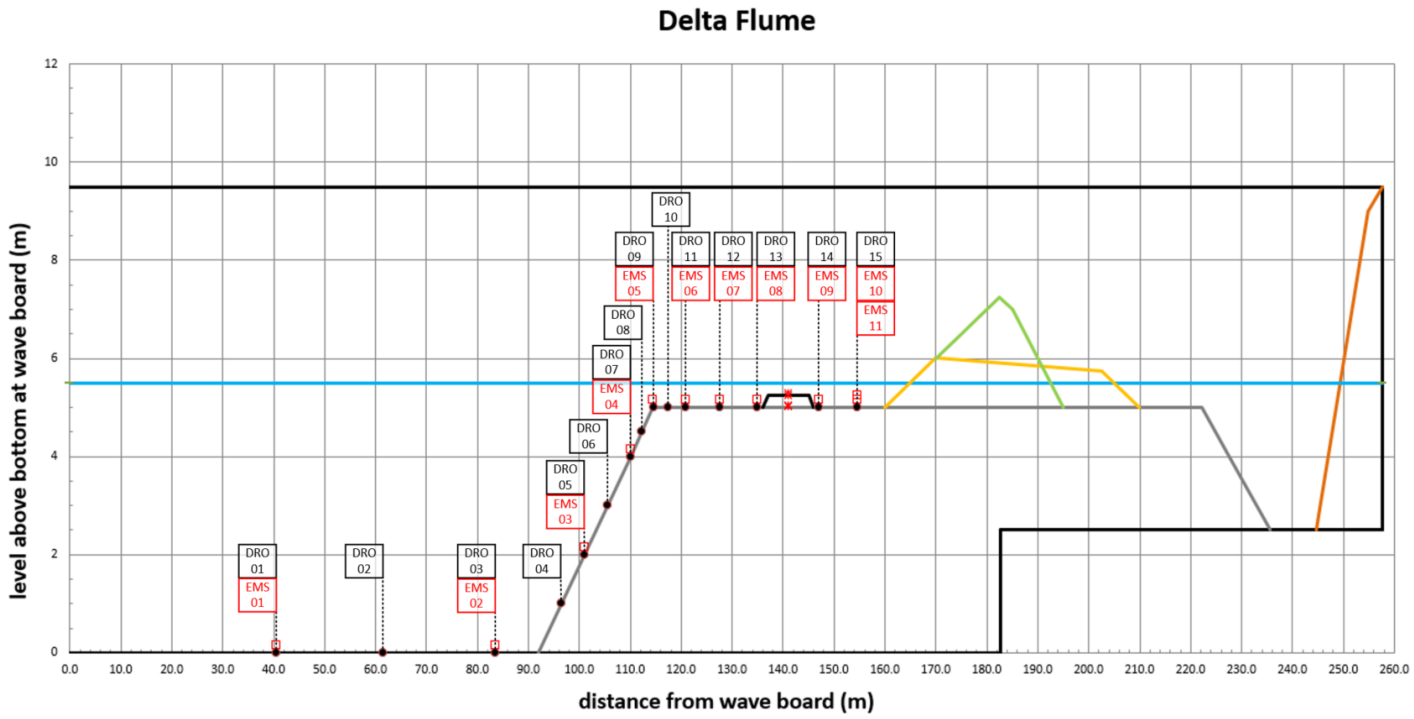

Figure A.1: Side view of laboratory setup including all pressure sensors (DRO) and velocity meters (EMS), including corresponding naming convention.

DRO				EMS			
Name	**x - position [m]**	**y - position [m]**	**z - position [m]**	**Name**	**x - position [m]**	**y - position [m]**	**z - position [m]**
DRO01	40.5	2.5	0.0	EMS01	40.5	2.5	0.15
DRO02	61.5	2.5	0.0	-	-	-	-
DRO03	83.5	2.5	0.0	EMS02	83.5	2.5	0.15
DRO04	96.43	2.5	0.98	-	-	-	-
DRO05	101.01	2.5	2.0	EMS03	101.0	2.5	2.15
DRO06	105.5	2.5	3.0	-	-	-	-
DRO07	109.98	2.5	4.0	EMS04	110.0	2.5	4.15
DRO08	112.24	2.5	4.48	-	-	-	-
DRO09	114.67	2.5	5.0	EMS05	114.5	2.5	5.15
DRO10	117.57	2.5	5.0	-	-	-	-
DRO11	121.06	2.5	5.0	EMS06	121.0	2.5	5.15
DRO12	127.55	2.5	5.0	EMS07	127.5	2.5	5.15
DRO13	135.03	2.5	5.0	EMS08	135.0	2.5	5.15
DRO14	147.04	2.5	5.0	EMS09	147.0	2.5	5.15
DRO15	154.54	2.5	5.0	EMS010	154.5	2.5	5.15
				EMS011	154.5	2.5	5.15

Table A.1: Precise positioning of all pressure sensors (DRO) and velocity meters (EMS), including corresponding naming convention. The x-position is measured from the wave generator and the z-position w.r.t. to the bottom of the flume.

B

SWASH Input Files

```
$*************HEADING*************************************
$
PROJ 'ARISE' 'BC3M'
$
$ Tp=9.24s Hs=0.5 m, dreef=0.33m
$
$***********MODEL INPUT*********************************
$
MODE DYN ONED
$
CGRID 0. 0. 0. 180. 0. 1800 0
$
VERT 10
$
INPGRID BOTTOM 0. 0. 0. 3600 0 0.05 0.
READINP BOTTOM 1. 'bathymetry_ARISE.bot' 1 0 FREE
$
FRIC MANNING 0.01
BREAK
SET BACKVISC 1e-4
NONHYDROSTATIC BOX 1. PREC ILU

SET LEVEL = 0.369

BOUNd SHAPespec JONswap 3.3 SIG PEAK DSPR DEGR
BOUNdcond SIDE W CCW BTYPE WEAK ADDBoundwave CON SPECTRUM 0.5 9.24 90 0 001500


DISCRET UPW MOM
DISCRET CORRDEP MUSCL
$
TIMEI 0.2 0.4
$

$************ OUTPUT REQUESTS *************************
$
POINTS 'GAUGE' FILE 'output_ARISE.loc'
TABLE  'GAUGE' NOHEAD 'output.tbl' TSEC XP DEPTH BOTL WATL VEL OUTPUT 000000.000 0.10 SEC

TEST 1 0
COMPUTE 000000.000 0.005 SEC 005500.000
STOP
```

Figure B.1: SWASH input file for run S0WL33C3

```
$*************HEADING*************************************
$
PROJ 'ARISE' 'RC3M'
$
$ Tp=9.24s Hs=0.5 m, dreef=0.33m
$
$********** GRIDS *********************************
$
MODE DYN ONED
$
CGRID 0. 0. 0. 180. 0. 1800 0  $[xpc] [ypc] [alpc] [xlenc] [ylenc] [mxc] [myc]
$
VERT 10 $ number of vertical layers
$
INPGRID BOTTOM 0. 0. 0. 3600 0 0.05 0.  $x0 y0 theta nx-1 ny-1 dx dy
READINP BOTTOM 1. 'bathymetry_ARISE.bot' 1 0 FREE

INPGRID PORO REG 0. 0. 0. 3600 0 0.05 0.
INPGRID PSIZ REG 0. 0. 0. 3600 0 0.05 0.
INPGRID HSTRUC REG 0. 0. 0. 3600 0 0.05 0.

READINP PORO 1 'Poro.dat' 3 0 FREE
READINP PSIZ 1 'Psize.dat' 3 0 FREE
READINP HSTRUC 1 'Hstruc.dat' 3 0 FREE

$ ********* BOUNDARIES *********
SET LEVEL = 0.338
BOUNd SHAPespec JONswap 3.3 SIG PEAK DSPR DEGR
BOUNdcond SIDE W CCW BTYPE WEAK ADDBoundwave CON SPECTRUM 0.5 9.24 90 0 001500

$ ******** PHYSICS *********

BREAK
FRICTION MANN 0.01
VISC VERTICAL KEPS
SET BACKVISC 1e-4

NONHYDROSTATIC BOX 1. PREC ILU

$ ********* NUMERICS ***********
DISCRET UPW MOM
DISCRET CORRDEP MUSCL
TIMEI 0.2 0.4

$************ OUTPUT REQUESTS *************************
POINTS 'GAUGE' FILE 'output_ARISE.loc'
TABLE  'GAUGE' NOHEAD 'output.tbl' TSEC XP DEPTH BOTL WATL VEL OUTPUT 000000.000 0.10 SEC
$ ************ COMPUTE ********************
TEST 1 0
COMPUTE 000000.000 0.005 SEC 005500.000
STOP
```

Figure B.2: SWASH input file for run S3WL33C3

Parameter	Details
SWASH Version	10.01
Run Duration	Between 3 to 6 hours
CPU	Intel i7-7700HQ, 2.8 GHz
Memory (RAM)	8 GB DDR4, 2133 MHz
Storage	SSD Storage
Operating System	Windows 10 64-bit

Table B.1: System and simulation details

C

Data Processing & Analysis Techniques

C.1. Pressure Sensor Processing

To convert pressure (kN/m^2) to sea surface elevation (m), the following steps are applied:

1. A dedicated air pressure sensor has been set up that continuously measures the air pressure at 120 hz. To smooth out short-term fluctuations in the air pressure data, a 5-minute moving average is applied and the resulting air pressure is removed from all sensors.
2. The adjusted pressure is converted to pressure head by dividing by ρ * g, in which ρ is the density of the water and g the acceleration due to gravity. Afterwards, the pressure head is corrected for their height with respect to the bed as well as for the still water level, which is acquired from the most offshore pressure sensor.
3. To convert the data to surface elevation, it is first detrended to remove any constant offsets or slow variations in the pressure signal that are unrelated to wave dynamics. Then, a Fast Fourier Transform (FFT) is applied to shift the data from the time domain to the frequency domain.
4. Next, wave number k is determined for each frequency using Guo's method (2002), which calculates k from an explicit solution to the wave dispersion relation.
5. Following linear wave theory, a correction factor is computed based on sensor height, hp, as $corr = cosh(k * h)/cosh(k * hp)$. For higher frequencies where $\frac{z_p}{L} > 0.2$ (with $z_p = h - h_p$ being the sensor height below the surface and $L = \frac{2\pi}{k}$ the wavelength), the correction factor is capped at the value corresponding to $\frac{z_p}{L} = 0.2$, following the recommendations of Bishop & Donelan (1987). The modified correction factor is then applied to the frequency-domain data, and the signal is transformed back into the time domain using an inverse FFT, producing the surface elevation time series η.

C.2. Computational Steps for Welch FFT

The computational steps for performing the Welch FFT are as follows:

1. First, the time-series is detrended by means of a second-order polynomial. Although both the lab data and SWASH simulations are generated from a stationary JONSWAP spectrum, non-stationarity can still arise due to the initial conditions (spin-up time) and the period at the end of the experiment when waves are no longer generated. To account for this, the first 10 minutes are removed, and the time series ends just before the wave generator stops producing waves, resulting in a 45-minute time series. As a precaution against potential non-stationarity, the data is detrended.

2. Afterwards, the time-series is split into 10 blocks of length nfft. The block length nfft and the sampling frequency F_s determine the frequency resolution F_{res} by dividing the sampling frequency over the block length nfft $F_s/nfft$. While the numerical simulations use a sampling frequency of 10 hz and the laboratory instruments 120 hz, by choosing a same number of blocks and having the same length of the time-series, the frequency resolution is equal for both datasets and equal to 0.0037 hz, which allows for capturing very low frequency components. A 50% overlap is used for the Welch computation, which means that each segment shares half of its data points with the adjacent segments, improving the stability.
3. Each block is then tapered with a Hamming window of length nfft. Windowing is necessary to prevent abrupt discontinuities at the segment boundaries, which can introduce artificial high-frequency components. Windowing smooths out these discontinuities by gradually reducing the amplitude of the data at the edges of each segment to zero (or near zero) while keeping the centre of the segment unaffected. Hamming windowing is chosen because it is computationally efficient as well as it maintains a high frequency resolution.
4. After performing these steps the Fast Fourier Transform is performed, resulting in a variance density spectrum with spectral density E [m^2/hz] for each simulation of the numerical model as well as for each sensor and experimental run for the laboratory experiments.

D

Complementary Figures for Chapter 7

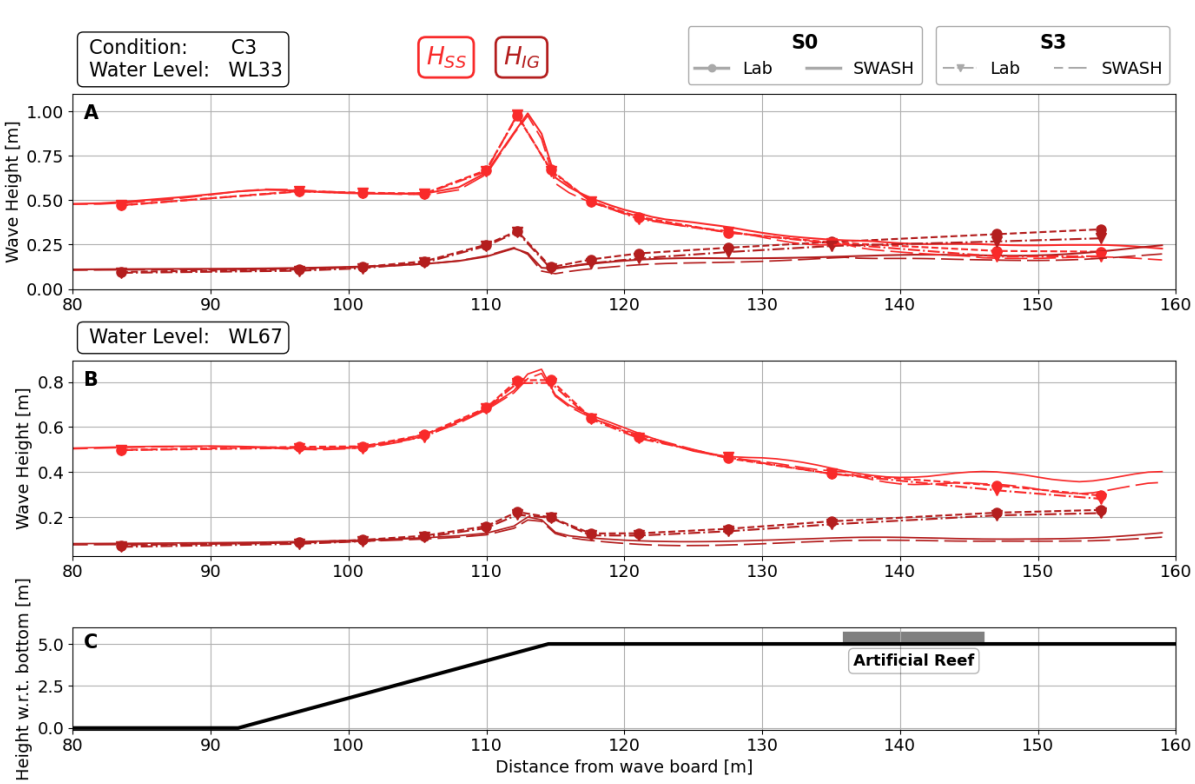

Figure D.1: Transformation of the SS and IG wave heights H_{SS} and H_{iG} for both water levels for wave condition **C3** (H_s = 0.5 m, T_p = 9.24 s). The figure includes both the laboratory data as well as the numerical results of SWASH.

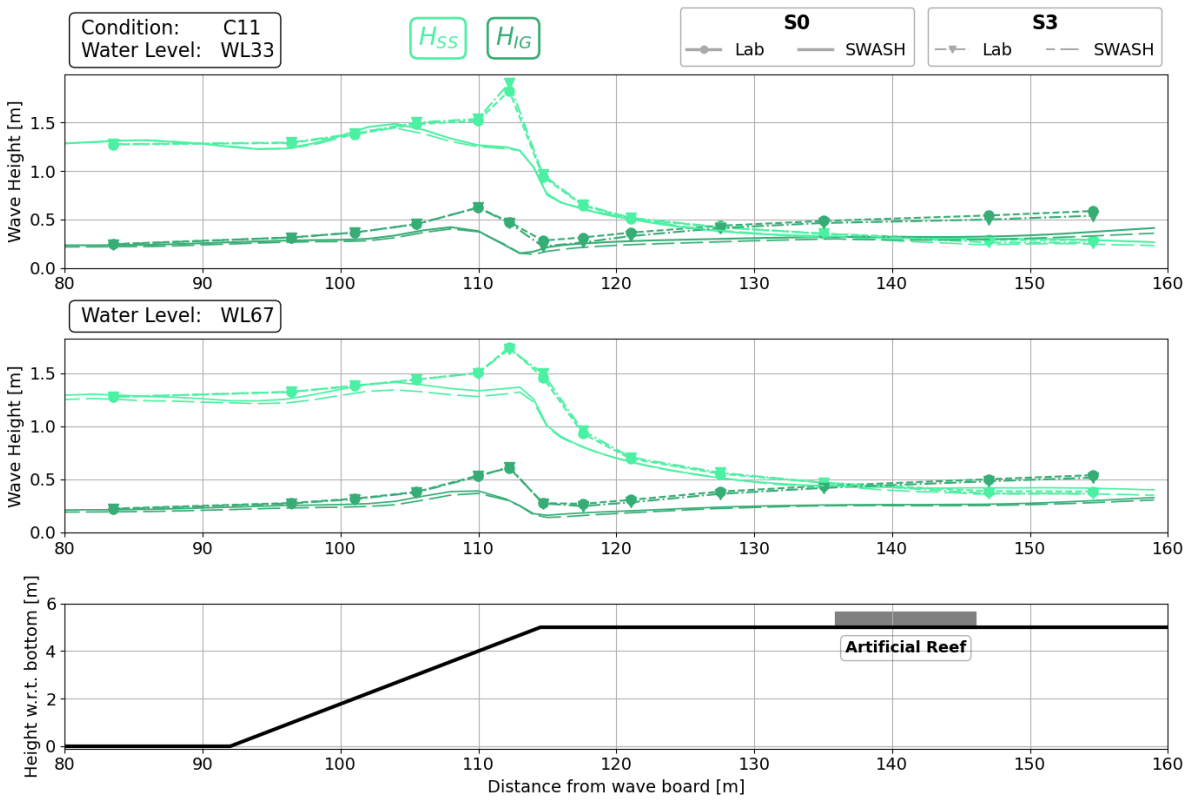

Figure D.2: Transformation of the SS and IG wave heights H_{SS} and H_{iG} for both water levels for wave condition **C11** (H_s = 1.3 m, T_p = 5.77 s).

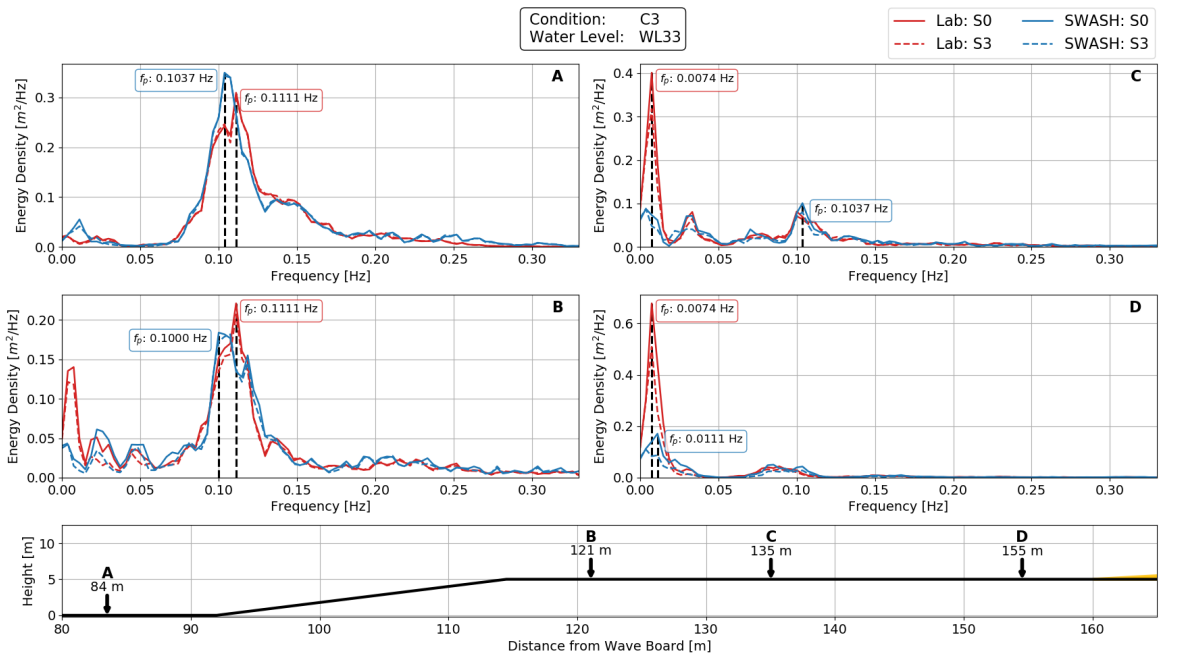

Figure D.3: Energy density spectra at several locations on the reef flat for wave condition **C3** at **WL33**. The figures show both the laboratory data as well as the SWASH output for both the base case S0 and case S3. The figures include the peak frequency f_p for each spectrum.

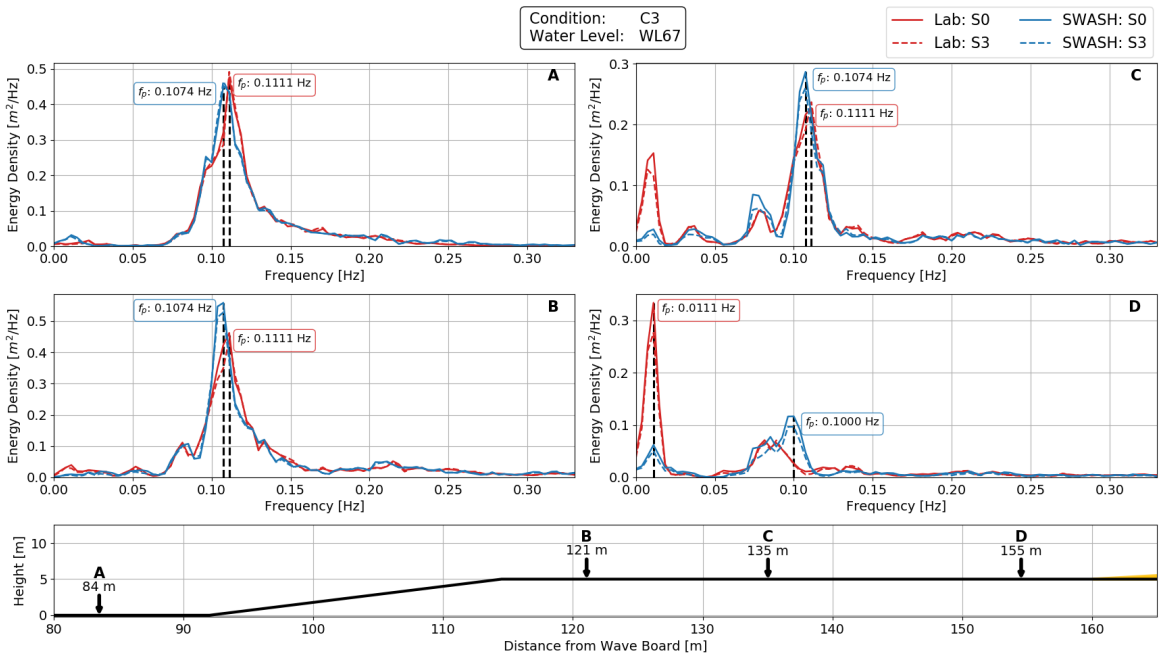

Figure D.4: Energy density spectra at several locations on the reef flat for wave condition **C3** at **WL67**.

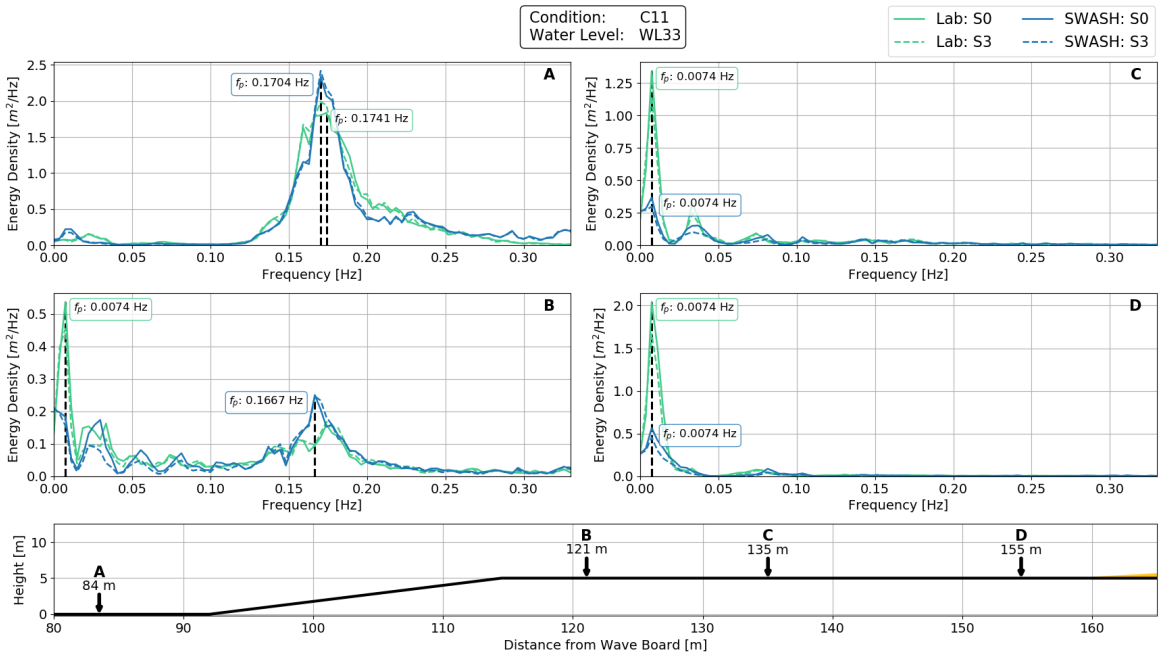

Figure D.5: Energy density spectra at several locations on the reef flat for wave condition **C11** at **WL33**.

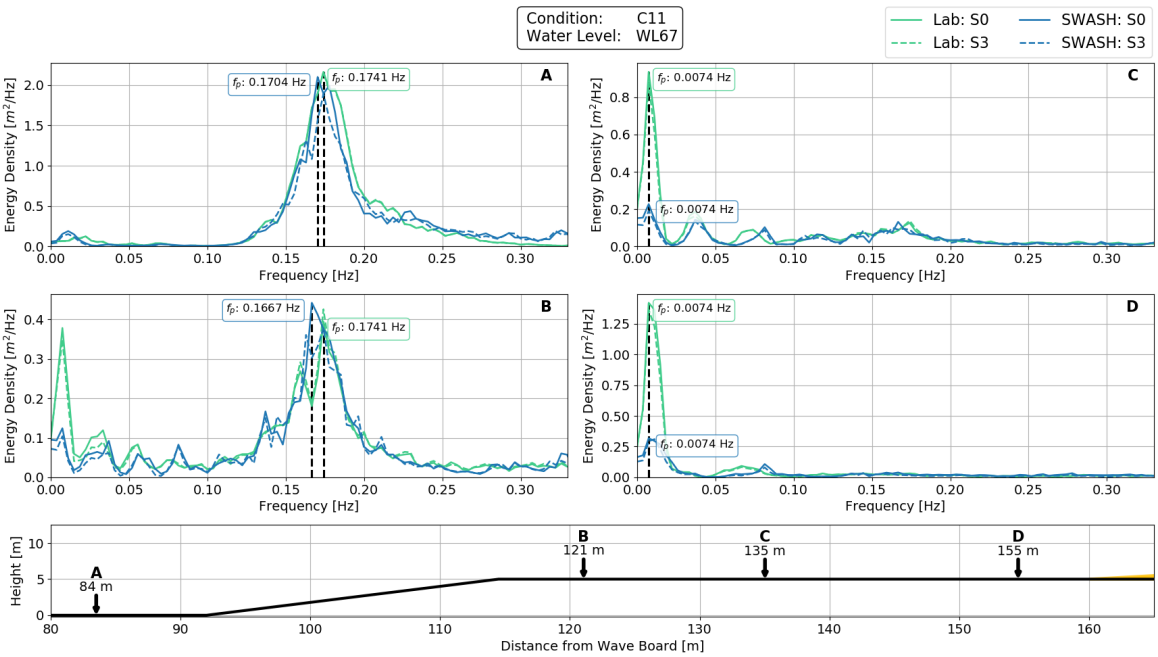

Figure D.6: Energy density spectra at several locations on the reef flat for wave condition **C11** at **WL67**.